AD_____
(Leave blank)

Award Number:
W81XWH-11-1-0768

TITLE:
Refining an Automated Transcranial Doppler System for the Detection of Vasospasm
after Traumatic Brain Injury

PRINCIPAL INVESTIGATOR:
Pierre D. Mourad, PhD

CONTRACTING ORGANIZATION:
 University of Washington,
 Seattle WA 98105

REPORT DATE: November 2015

TYPE OF REPORT:
annual report

PREPARED FOR: U.S. Army Medical Research and Materiel Command
           Fort Detrick, Maryland 21702-5012

DISTRIBUTION STATEMENT:

   X Approved for public release; distribution unlimited

REPORT DOCUMENTATION PAGE

Form Approved
OMB No. 0704-0188

Public reporting burden for this collection of information is estimated to average 1 hour per response, including the time for reviewing instructions, searching existing data sources, gathering and maintaining the data needed, and completing and reviewing this collection of information. Send comments regarding this burden estimate or any other aspect of this collection of information, including suggestions for reducing this burden to Department of Defense, Washington Headquarters Services, Directorate for Information Operations and Reports (0704-0188), 1215 Jefferson Davis Highway, Suite 1204, Arlington, VA 22202-4302. Respondents should be aware that notwithstanding any other provision of law, no person shall be subject to any penalty for failing to comply with a collection of information if it does not display a currently valid OMB control number. **PLEASE DO NOT RETURN YOUR FORM TO THE ABOVE ADDRESS.**

1. REPORT DATE	2. REPORT TYPE	3. DATES COVERED
November 2015	annual	1 Sep 2011 - 31 Aug 2015

4. TITLE AND SUBTITLE	5a. CONTRACT NUMBER
Refining an Automated Transcranial Doppler System for the Detection of Vasospasm after Traumatic Brain Injury	
	5b. GRANT NUMBER
	W81XWH-11-1-0768
	5c. PROGRAM ELEMENT NUMBER

6. AUTHOR(S)	5d. PROJECT NUMBER
Pierre D. Mourad, PhD	
	5e. TASK NUMBER
E-Mail: pierre@apl.washington.edu	5f. WORK UNIT NUMBER

7. PERFORMING ORGANIZATION NAME(S) AND ADDRESS(ES) AND ADDRESS(ES)	8. PERFORMING ORGANIZATION REPORT NUMBER
Applied Physics Laboratory, University of Washington, Box 355640 Seattle WA 98195-6470	

9. SPONSORING / MONITORING AGENCY NAME(S) AND ADDRESS(ES)	10. SPONSOR/MONITOR'S ACRONYM(S)
U.S. Army Medical Research and Materiel Command Fort Detrick, Maryland 21702-5012	
	11. SPONSOR/MONITOR'S REPORT NUMBER(S)

12. DISTRIBUTION / AVAILABILITY STATEMENT
Approved for Public Release; Distribution Unlimited

13. SUPPLEMENTARY NOTES

14. ABSTRACT
Traumatic brain injury (TBI) is a major contributor to morbidity and mortality experienced by those soldiers subjected to improvised explosive devices (IED) as well as in military and civilian high speed collisions. Traumatic cerebral vasospasm (TCV) is a major contributor to morbidity and mortality experienced by those TBI patients. Aggressive neurosurgical treatment motivated by early diagnosis appears to improve the clinical outcome for these patients. Early transcranial Doppler (TCD) measurements of blood flow speed within major cerebral arteries produces the initial diagnosis, hence motivates the rapid treatment of TCV. However, the skill necessary to deploy TCD limits its availability relative to its need. PhysioSonics, Inc, a local company in Seattle, created an *automatic* TCD system (called 'Presto' or aTCD) that minimizes the skill necessary to perform TCD assays. Our long-term goal is to optimize Presto for patients in vasospasm, through optimization of its spectral Doppler 'envelope' analyzer, its headset and supporting software so it can track blood flow in the internal carotid artery as well as middle cerebral artery.

15. SUBJECT TERMS
traumatic brain injury, ultrasound, transcranial Doppler, vasospasm.

16. SECURITY CLASSIFICATION OF:			17. LIMITATION OF ABSTRACT	18. NUMBER OF PAGES	19a. NAME OF RESPONSIBLE PERSON USAMRMC
a. REPORT U	b. ABSTRACT U	c. THIS PAGE U	UU		19b. TELEPHONE NUMBER *(include area code)*

Table of Contents

INTRODUCTION – subject. Traumatic brain injury (TBI) is a major contributor to morbidity and mortality experienced by those soldiers subjected to improvised explosive devices (IED) as well as in military and civilian high speed collisions. Traumatic cerebral vasospasm (TCV) is a major contributor to morbidity and mortality experienced by those TBI patients. Aggressive neurosurgical treatment motivated by early diagnosis appears to improve the clinical outcome for these patients. Early transcranial Doppler (TCD) measurements of blood flow speed within major cerebral arteries produces the initial diagnosis, hence motivates the rapid treatment of TCV. However, the skill necessary to deploy TCD limits its availability relative to its need. This gap in patient care reduces the quality of care and potentially, therefore, the quality of life of injured soldiers. This gap also defines a critical need for robust, easy to use TCD system, applicable to these patients.

INTRODUCTION - purpose. Early work by the PI on automating transcranial Doppler has been translated by PhysioSonics, Inc, (PSI) a Seattle-based company that he co-founded into a working automated transcranial Doppler (aTCD) device called 'Presto' that they have submitted to the FDA via a 510K for approval. Their system is based upon a novel and proprietary ultrasound platform along with novel and proprietary 'search and lock on' algorithms for detecting and staying focused on the brightest spot in 'Doppler' space – that is, within ultrasound-derived maps of blood flow speed captured by their device. This is reasonable because a view of each of the major cerebral arteries relevant to vasospasm, listed below, shows that each contribute the largest values of blood flow, hence the largest signal in Doppler space. PhysioSonics has optimized it to measure blood flow speed within the middle cerebral artery (MCA) – sufficient for some assays of vasospasm, and demonstrated its utility on uninjured volunteers. However, a critical additional assay of vasospasm – the Lindegaard ratio - requires measurements of blood flow speed within the extra-cranial segment of the internal carotid artery as well as from the MCA. Moreover, while their system already works on humans, PhysioSonics has no plans to optimize the device for TCV, or to extract information from the ICA.

INTRODUCTION – scope of the research. To met the goal of this proposal we sought to test the following hypothesis: PhysioSonics' automatic TCD (aTCD) system, with modifications to its hardware and/or software as necessary, will match measurements of cerebral blood flow in the middle cerebral artery (MCA) and in the internal carotid artery (ICA) made by standard TCD on patients who suffer from cerebral vasospasm.

Specific Aim # 1: To test the ability of the aTCD device to measure blood flow velocity in the MCA and ICA of patients with known vasospasm, as compared to standard TCD run by a trained neurosonographer. *Proposed study:* Use the device to measure blood flow in the MCA and ICA of civilian vasospasm patients – typically those with sub-arachnoid hemorrhage – within Harborview Medical Center (HMC), the only Level One trauma center in Seattle.   Compare those measurements with those determined during routine clinical care by the resident neurosonographer with their standard clinical TCD unit. Determine the level of fidelity of the aTCD-derived information on blood flow with that given by the gold standard, operator-dependent TCD device.

Specific Aim #2: To modify as necessary the TCD array and associated holder for use on the ICA, and, the algorithms required to extract the highest blood flow velocities in the MCA and ICA to guarantee that the aTCD device can detect the highest levels of vasospasm. *Proposed study #1:* Modify as necessary the brace that ordinarily holds the transducer to the temple (to facilitate measurement of blood-flow from within the MCA so that it will automatically extract blood flow information from the ICA. *Proposed study #2:* Modify as necessary the software within the aTCD device to optimize its ability to <u>calculate</u> the value of fastest blood flow within the MCA and the ICA for vasospasm patients. *Proposed study #3:* Modify as necessary the TCD transducer or its controlling software so as to optimize its ability to <u>locate</u> the point of fastest blood flow within the MCA and the ICA for vasospasm patients

Impact. Successful completion of the proposed work will yield a device that could readily become available to the military with its data interpreted on site or sent or via telemedicine for interpretation by distant neurosurgical experts.

Specific Aim #1: To test the ability of the aTCD device to measure blood flow velocity in the middle cerebral artery (MCA) and internal carotid artery (ICA) of patients with known vasospasm, as compared to standard TCD run by a trained neurosonographer. (Q1-Q10 out of 12 quarters)

Task 1: Get approval for the human subjects study (Q1-2). This study will involve up to 128 patients with vasospasm, with multiple studies per patient, over the three years of the study.

(1.1) **Done in the first year.**

Task 2: Take possession of the aTCD system (Q3).

(2.1) **Done in the first year.**

Task 3: Modify the software associated the aTCD system so it will report and store the spectrogram derived from each of the MCA and ICA, including the Lindegaard ratio. (Q2-5).

(3.1) **Done in the first year.**

Milestone #1: Achieve ability to start human study. **Done.**

Task 4: Modify as necessary the commercial headband that holds the TCD so that it can deploy on the upper portion of the neck of *volunteers*. (Q1-2)

(4.1) **Done in the first year.**

Task 5: Collect then archive aTCD and standard TCD data from the MCA and ICA of 128 patients, along with appropriate supporting medical data. For a subset of these patients we will also collect standard TCD data twice in a day in order to determine the length of time we will need to eventually monitor patients with our aTCD (Q3-Q10) UW.

(5.1) We started to recruit patients with civilian vasospasm in the 5/12th quarter of our study (October 2012). Table 1 documents the number of patients identified, consented, and studied during this research effort (October 2012 – August 2015).

Human Data	Identified	Consented	Studied	# of data sets
1Oct2012-15Sept2013	65	22	16	25
1Oct2013 – 30Sept2014	148	37	34	46
1Oct2014 – 31Aug2015	125	42	33	48
Total	338	101	83	119

Note that we lose two thirds of our identified patients to: lack of bone windows, lack of available next of kin, refusal to participate (a big problem because these patients are typically awake but uncomfortable), lack of cranial bone and patient death.

Task 6: Compare spectrogram features found within aTCD and standard TCD data. (Q5-Q10) UW

(6.1) In Figures 1-3 we compare representative blood-flow data in the MCA of three vasospasm patients. (Note that we get pdfs from the commercial system whose resolution for this report fall short of adequate representation when reproduced here.) These examples demonstrate that we can collect TCD data from the MCA of patients, with a mix of success in their comparison with the gold standard data, in ways that have or will produce improvements in the aTCD system.

Our system's data falls short in two key areas – the search algorithm and the spectral envelope calculation – as anticipated during the construction of this grant application. Indeed, our tasks as originally designed below seek to address these issues. As described in our 2nd annual report, we modified the aTCD device to search deeper, where our previous maximum depth was 50 mm and is now 70mm. We have now also added a feature where the user is able to force the machine to find peak flow in a certain volume of depth, by moving search box covering 10 mm vertical distance – this is described in detail in Task 10 below. This is meant to address some issues of the locking flow selection feature, where non-peak flow was selected.

Also, here we show the standard TCD system's reports of mean flow speeds, e.g. 107 cm/s at a depth in the left MCA of 50 mm, and pulsatility index (PI), a relative measure of the tendency of the peak systolic blood flow speed to rise above the mean blood flow speed. The aTCD system also reports these values, but in a different window. We will develop quantitative comparisons of these quantities as well as of peak systolic blood flow speed. Also, our ICA measurements with the aTCD system compare favorably with that of the clinical system. We have focused on those measurements that motivate changes to the aTCD system here for this report.
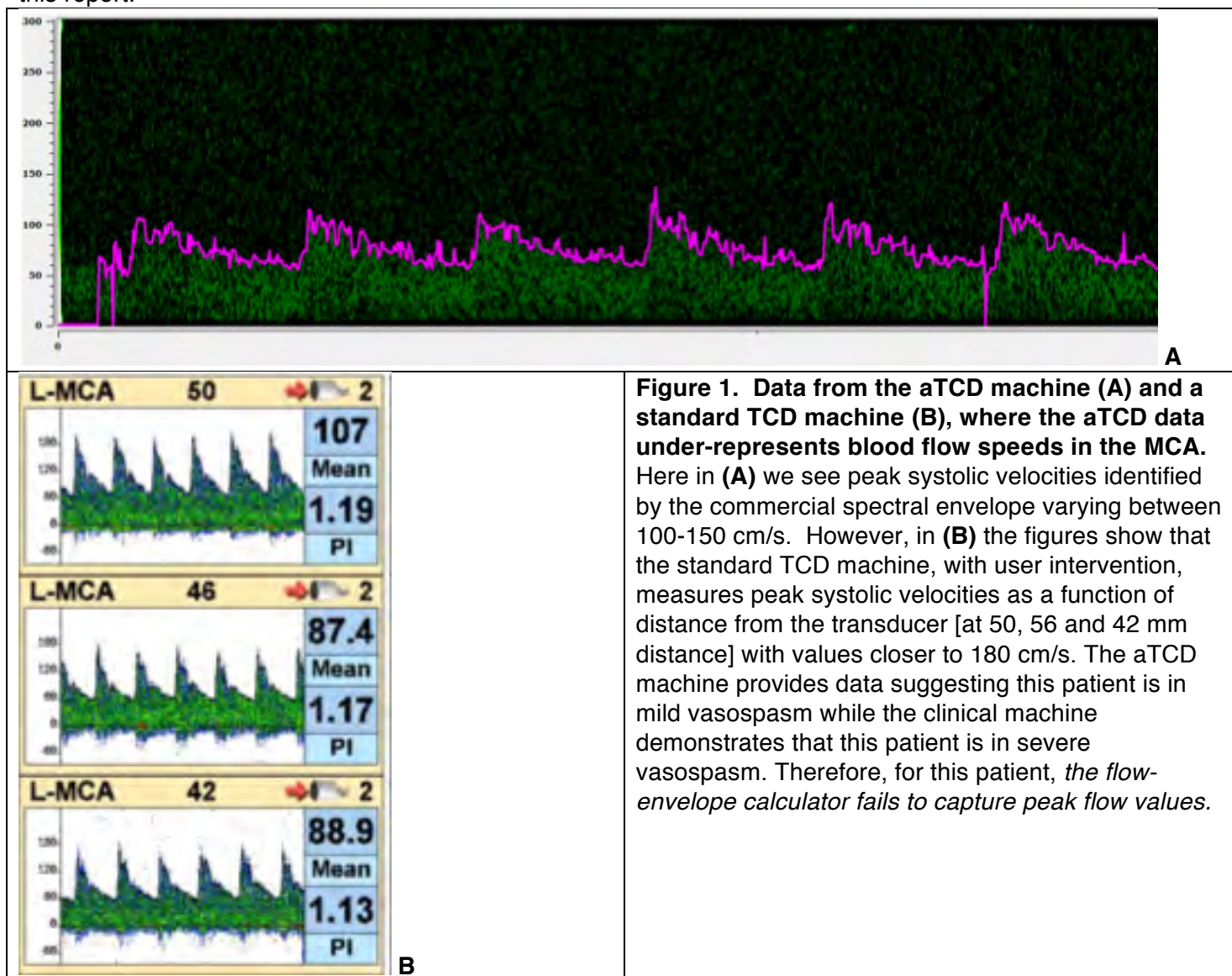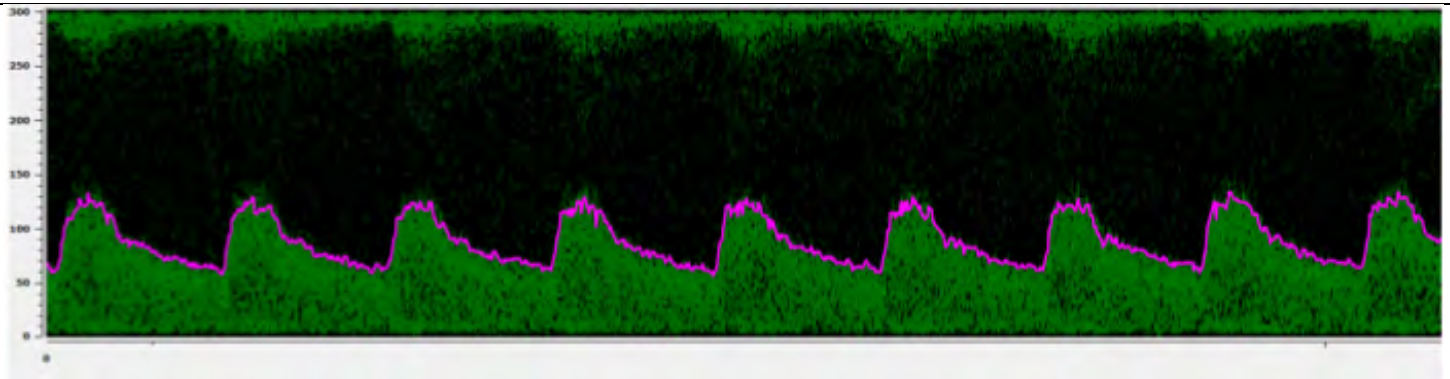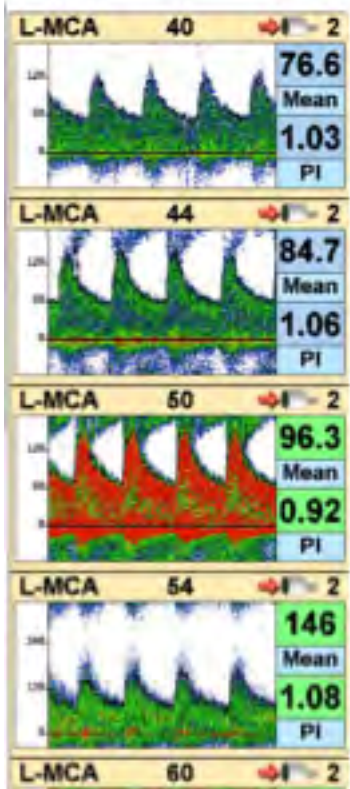

A

B

Figure 1. Data from the aTCD machine (A) and a standard TCD machine (B), where the aTCD data under-represents blood flow speeds in the MCA. Here in **(A)** we see peak systolic velocities identified by the commercial spectral envelope varying between 100-150 cm/s. However, in **(B)** the figures show that the standard TCD machine, with user intervention, measures peak systolic velocities as a function of distance from the transducer [at 50, 56 and 42 mm distance] with values closer to 180 cm/s. The aTCD machine provides data suggesting this patient is in mild vasospasm while the clinical machine demonstrates that this patient is in severe vasospasm. Therefore, for this patient, *the flow-envelope calculator fails to capture peak flow values.*

6

A

B

Figure 2. Data from the aTCD machine (A) and a standard TCD machine (B), where the aTCD data well represents the blood flow speeds in the MCA as defined by the standard TCD machine. Here in **(A)** we see peak systolic velocities identified by the commercial spectral envelope (in fucia) 140-150 cm/s, nominally close to the underlying spectrogram (in green). This compares favorably to measurements of peak systolic blood flow speeds **(B)** by the standard TCD machine as a function of depth [at 40, 44, 50 and 54 mm distance from the transducer]. These peak speeds start at a value of 120 cm/s at 40 mm distance from the transducer, increasing to close to 150 cm/s by 54 mm distance. Both the aTCD machine and clinical machine demonstrates that this patient is in moderate to severe vasospasm. Therefore, for this patient, *the aTCD system performs plausibly well compared to the clinical system.*
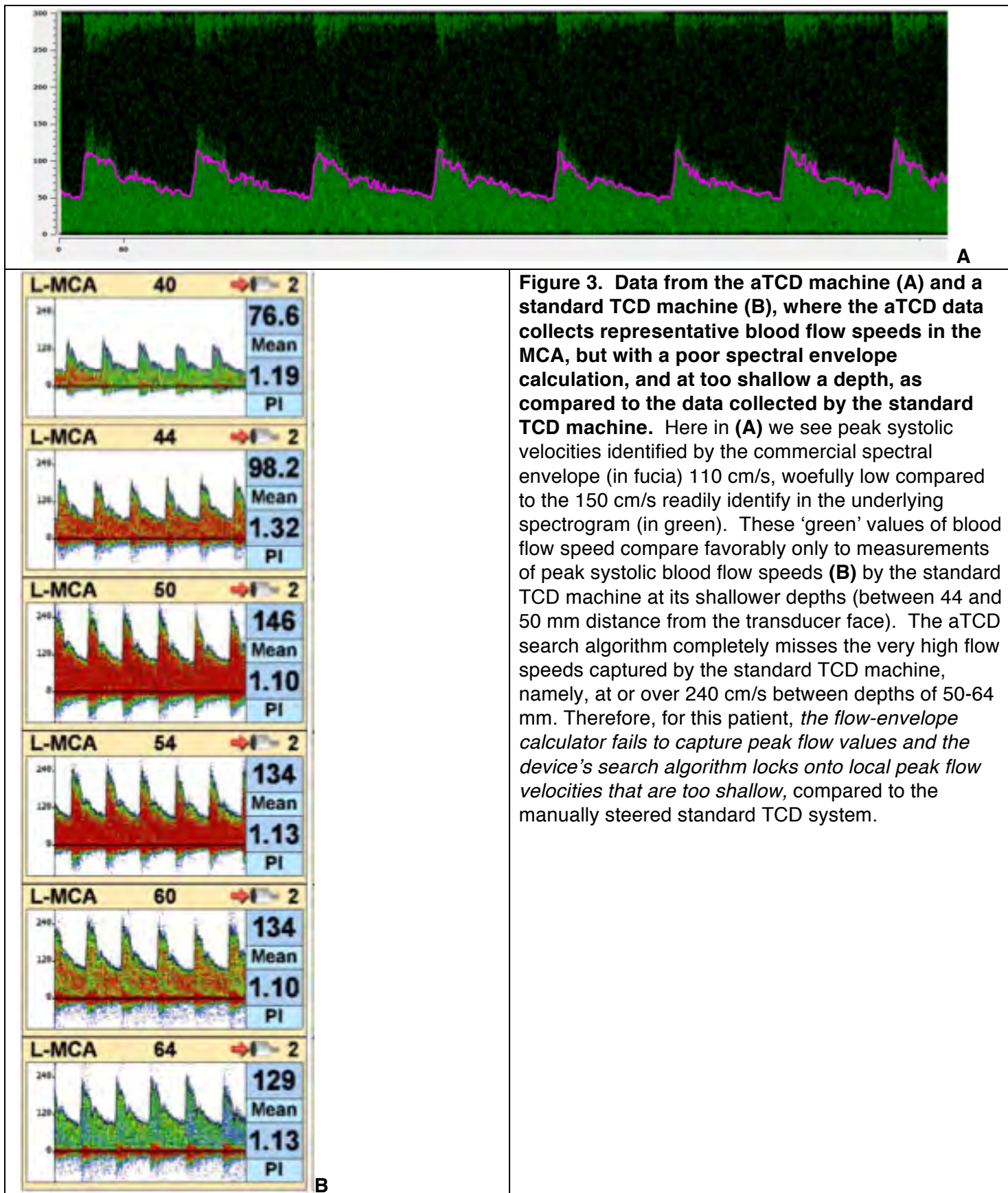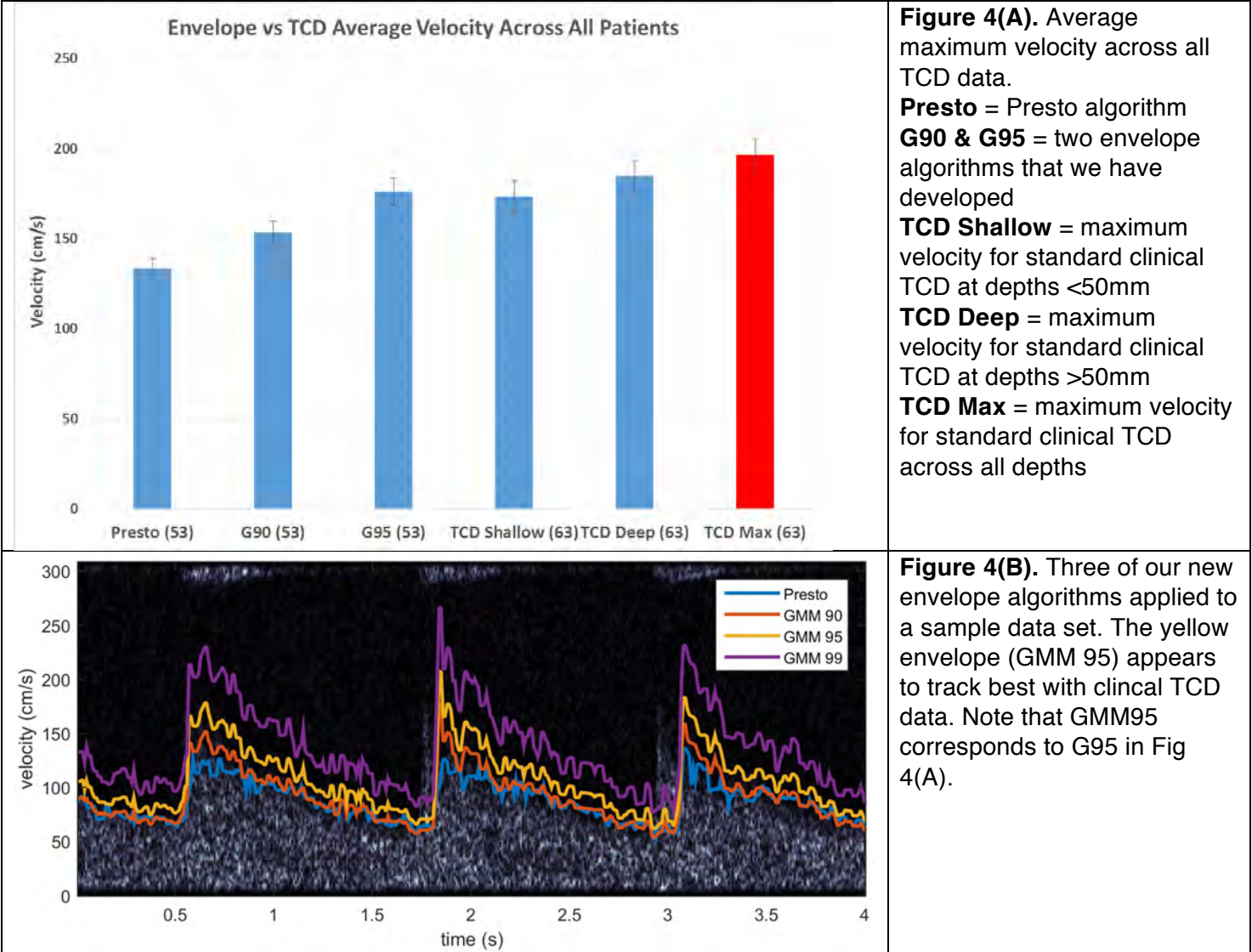
A

B

Figure 3. Data from the aTCD machine (A) and a standard TCD machine (B), where the aTCD data collects representative blood flow speeds in the MCA, but with a poor spectral envelope calculation, and at too shallow a depth, as compared to the data collected by the standard TCD machine. Here in **(A)** we see peak systolic velocities identified by the commercial spectral envelope (in fucia) 110 cm/s, woefully low compared to the 150 cm/s readily identify in the underlying spectrogram (in green). These 'green' values of blood flow speed compare favorably only to measurements of peak systolic blood flow speeds **(B)** by the standard TCD machine at its shallower depths (between 44 and 50 mm distance from the transducer face). The aTCD search algorithm completely misses the very high flow speeds captured by the standard TCD machine, namely, at or over 240 cm/s between depths of 50-64 mm. Therefore, for this patient, *the flow-envelope calculator fails to capture peak flow values and the device's search algorithm locks onto local peak flow velocities that are too shallow,* compared to the manually steered standard TCD system.

8

We have developed three enveloping algorithms, of which one appears to track best with standard clinical TCD machines. Figure 4(a), below, shows the average TCD velocity across all patients compared between the Presto algorithm, our G90 and G95 algorithms, and compared to the standard clinical machine data (looking at shallow flow data < 50 mm deep, and at the maximum across the entire depth range). Figures 4(B) and 4(C) are two examples of envelopes calculated using our three new algorithms and the original Presto algorithm. The yellow envelope (GMM 95/G95) appears to track best with standard clinical TCD data, when we look only at shallow depths (that is, less than 50mm). The signal-locating algorithm on the Presto has a tendency to focus on signals within 50mm of the transducer face, therefore we believe that a majority of our Presto data comes from within that range.
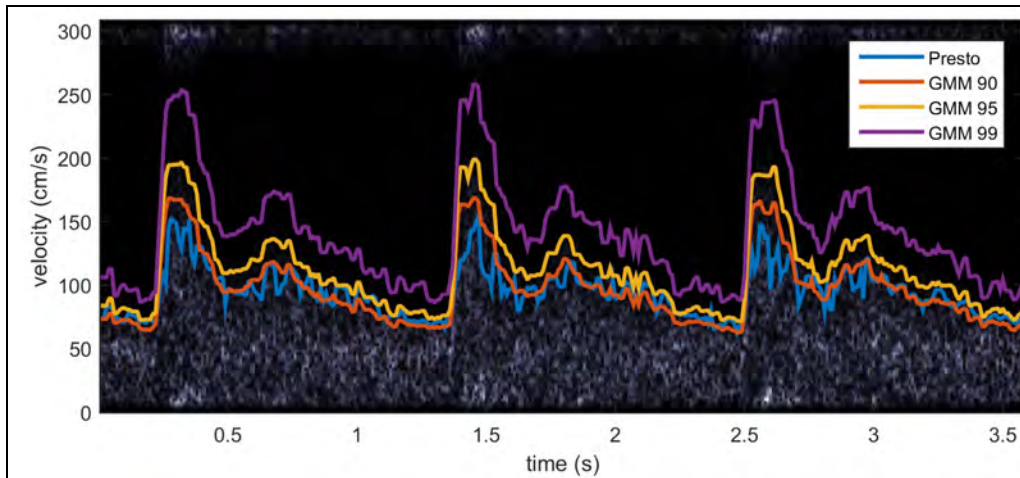

Figure 4(A). Average maximum velocity across all TCD data.
Presto = Presto algorithm
G90 & G95 = two envelope algorithms that we have developed
TCD Shallow = maximum velocity for standard clinical TCD at depths <50mm
TCD Deep = maximum velocity for standard clinical TCD at depths >50mm
TCD Max = maximum velocity for standard clinical TCD across all depths

Figure 4(B). Three of our new envelope algorithms applied to a sample data set. The yellow envelope (GMM 95) appears to track best with clincal TCD data. Note that GMM95 corresponds to G95 in Fig 4(A).
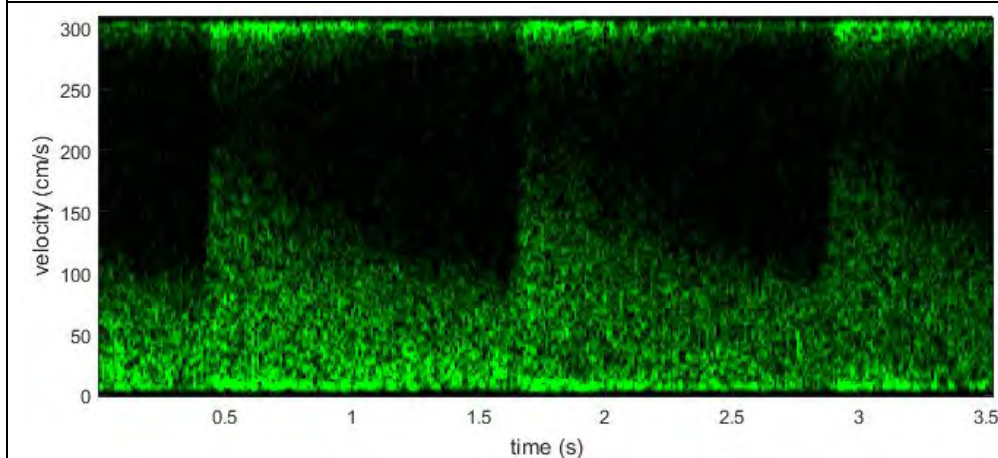
Figure 4(C). Three of our new envelope algorithms applied to a sample data set. The yellow envelope (GMM 95) appears to track best with clincal TCD data. Note that GMM95 corresponds to G95 in Fig 4(A).
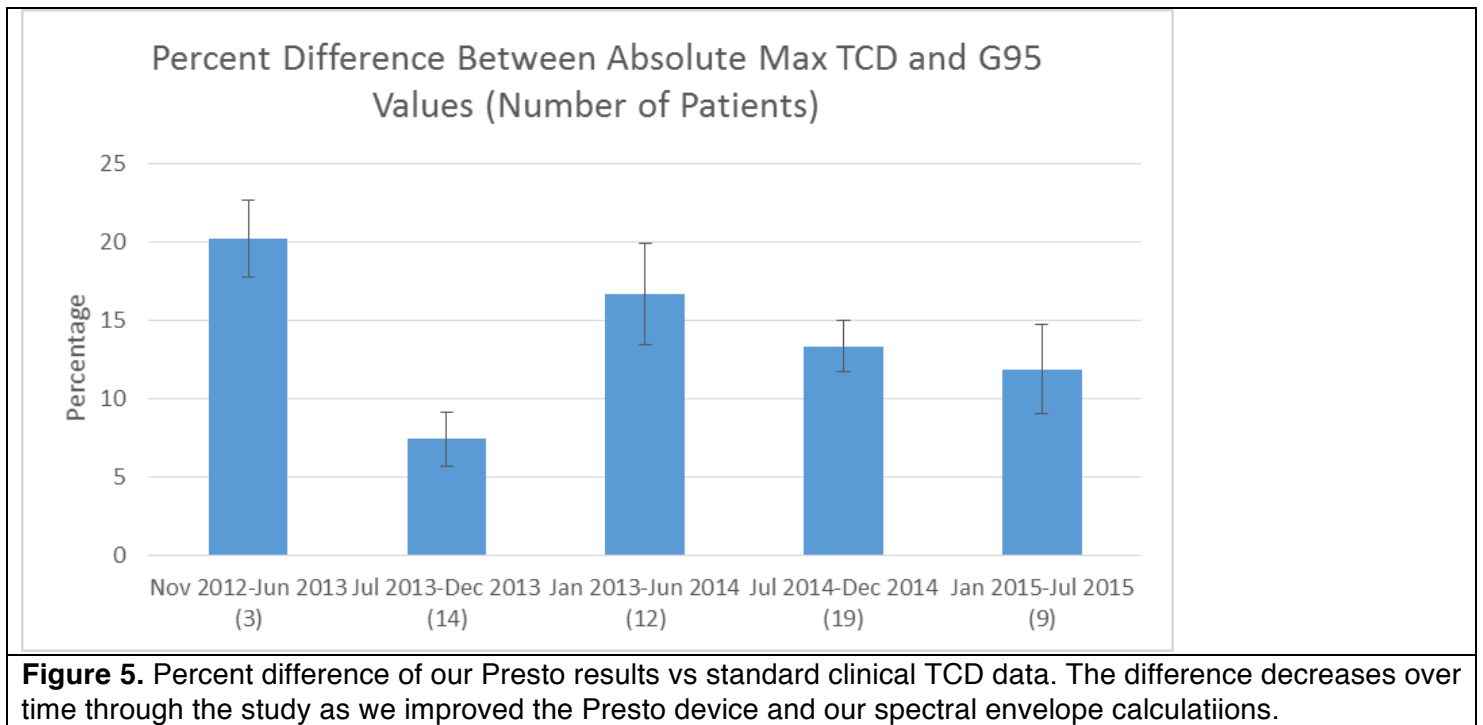

Figure 4(D). An example where the Presto's native envelope algorithm fails to capture the spectrogram accurately. The G95 model (yellow line) is much more effective and accurate in capturing the peaks in the data. Note that GMM95 corresponds to G95 in Fig 4(A).
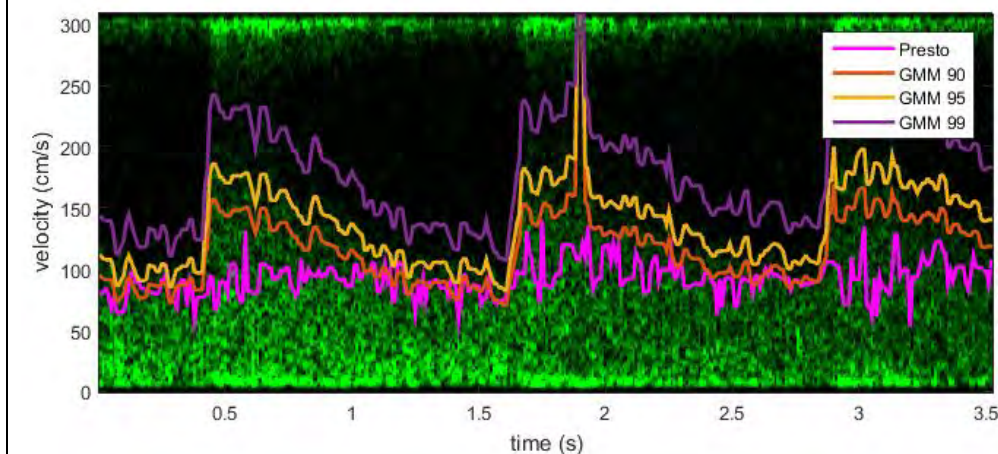
We also analyzed the results for the best envelope algorithm compared to standard TCD results as a function of percent difference over time during the study. The results show a steady trend toward greater accuracy in our Presto results compared to standard TCD. Our initial results in the first 6 months of data collection averaged 6.5% off from the standard TCD. By 18-24 months into the study, our results averaged less than 1.5% off from the standard TCD (Figure 5, below).

Figure 5. Percent difference of our Presto results vs standard clinical TCD data. The difference decreases over time through the study as we improved the Presto device and our spectral envelope calculatiions.

Milestone #2: Develop quantitative comparisons of the aTCD-derived and standard TCD-derived blood flow data from vasospasm patients, thereby highlighting short comings, if any, of the aTCD system for the case of vasospasm.

We have collected sufficient number of data sets from our patients to identify three problems with our existing aTCD system: [1a] the flow-envelope calculator fails to capture peak flow values and [1b] the device's search algorithm locks onto local peak flow velocities at too shallow a depth for many patients with vasospasm, all relative to the clinical gold standard. In addition, thanks to the formation of peripheral edema in several of these patients, we can say that [1c] the device's search volume is too shallow for an appreciable percentage of patients with vasospasm. Task 9 addresses problem #1a while Task 10 addresses problems #1b,c.

Task 7: Write up results for publication and presentations. (Q7-8; Q10-12) UW
(7.1) The Journal of Ultrasound in Medicine has published our paper (Marzban et al, 2013) that describes our first robust means of calculating optimal spectrogram envelopes for different patients. We have submitted two additional papers. One describes a second means of calculating optimal spectral envelopes (Morison et al, 2015), one based upon a first principles method described in our previous report and the results are summarized below beginning at Figure 10. This paper has been submitted to *Biomedical Signal Processing and Control.* We have published a third paper associated with this project, one based upon a new statistics-based modeling effort for calculating spectra, which we report below (Marzban et al, 2016).

Milestone #3: get feedback on the quantitative aspects of our work from our scientific and clinical peers.
Our clinical peers are quite excited by the prospect of successful semi-automation of the TCD process but recognize that we've a ways to go before we succeed. In particular, our military TCD consultant, Alex Razumovsky, PhD, has verified the importance of this approach to TCD measurements and has asked us to (a) increase the depth of field of search for fastest blood flow, to (b) improve the signal-to-noise ratio of our system, to (c) explore use of an intermediate variable – a time-varying map of the MCA based upon creation of an 'iso-surface' of Doppler-derived blood-flow speeds – a 'Doppler map', discussed below – to map the blood-vessel structure sufficiently to visualize the MCA in vasospasm. This last issue is particularly important because some patients after blast show large blood flow speeds in the MCA not because they are in vasospasm but because their hematocrit is sufficiently low that the resulting reduced effective viscosity of the blood allows for higher than normal blood flow speeds.
We have one paper in print, and now have submitted two more papers that describe and exercise our

11

flow envelope calculation.

Specific Aim #2: To modify as necessary the TCD holder for use on the ICA, and, the algorithms required to localize as well as extract the highest blood flow velocities in the MCA and ICA, in order to guarantee that the aTCD device can detect the highest levels of vasospasm. (Q3-Q12 out of 12 quarters)

Task 8: Modify as necessary the brace that ordinarily holds the transducer to the temple (to facilitate measurement of blood-flow from within the MCA) so that it will also automatically extract blood flow information from the ICA of *patients*. (Q4-Q8) PSI

(8.1) Our third version of the headset (reported in our second Annual Report) now covers both the MCA and internal carotid arteries. Patients remain uncomfortable using any headset, however. We have now developed a new headset, which is intended to minimize patient discomfort while stabilizing the transducers. Below are the computer modeled plans for the headset. The two transducers are clipped in place, and can be adjusted by sliding the holder and securing it with the knob. This should allow the headset design to function on most head shapes and sizes. Disposable foam pads would line the headset and would be replaced for each patient. All the plastic used in the headset should be autoclave safe, such that the entire headset (except for the foam pads) could be autoclaved.
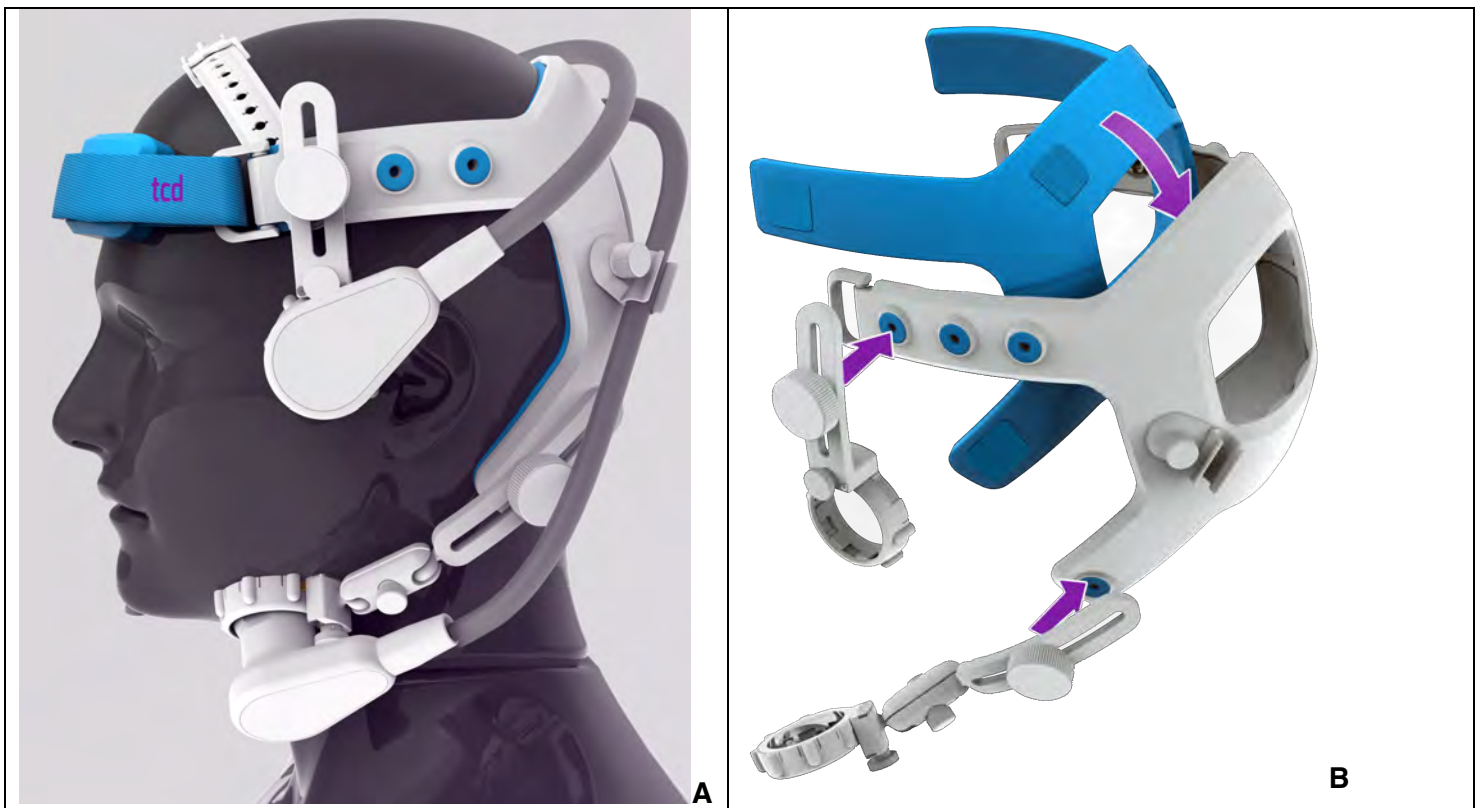

A   B

Figure 6.
(A) Computer generated model of the final headset design. Both transducers are placed on sliders such that they can be accurately positioned for a given patient's anatomy.
(B) Another view of the computer generated model of the headset, showing the placement of the foam pads between the patient's head and the plastic components of the headset.
(C) The actual produced prototype of the headset, modelled on a real person. The transducers would wrap around the back of the head to avoid interfering with a patient's movement.

Milestone #4: Deliver device that holds the transducer that supports the measurement of blood flow velocity in the MCA and ipsilateral ICA for its deployment in Aim #1. **Done.** We've encountered an important practical problem for this study, however, namely that no test subjects wish to use the headset, given the general discomfort of our patients, all of whom have not had sufficient subarachnoid hemorrhage to require induction of a therapeutic coma. The headset is comfortable enough, as tested by engineers. The vasospasm patients are profoundly uncomfortable, however, and not obliged to wear the headset per our existing IRB protocol. We will talk to the program manager about adding a new Task to this study where we will refine the designs of this headset using feedback from healthy volunteers.

Task 9: Modify as necessary the software within the aTCD device to optimize its ability to <u>calculate</u> the value of fastest blood flow (the spectral envelope) within the MCA and the ICA for vasospasm patients. (Q4-Q10) UW and PSI.

First recall that the device as delivered will report values of the spectral envelope. Our job requires optimization of this process for vasospasm patients, a notoriously difficult cohort. We have identified two pathways towards development of optimized means of calculating the value of fastest blood flow in the MCA and ICA, referred to here as the spectral envelope: a statistical analysis and a mathematical modeling analysis. We have published results from the first pathway and continue to refine the details of the second method. We have now begun the process of initiating data collection on vasospasm patients at Swedish Medical Center here in Seattle using a certain standard TCD device that allows us to access the raw flow data. We have had difficulties recruiting enough patients that actually enter vasospasm, so this expansion will, hopefully, lead to a greater vasospasm sample size on which to test our enveloping algorithms. We hope to begin collecting data on vasospasm patients at Swedish by the end of 2014.

(9.1) As reported earlier we have applied our Double-Gaussian spectral flow envelope calculator (Marzban et al, 2013) to our new vasospasm patients with success thus far. We have completed work on another means of calculating the spectral envelope. This new approach uses the 'mixture' paradigm of Marzban et al, 2013, where a sum of functions adds together to describe the distribution of blood-flow speeds a given instant in time, from which the point of fastest blood flow is derived for that instant. The earlier published work assumed that the instantaneous distribution of flow was best modeled by a Gaussian function. Here (Marzban et al, 2016) we relax that assumption, making use of two alternatives – a 'skewed' Gaussian function and an entirely non-Gaussian function (Figure 7-8). The skewed-Gaussian function has two additional parameters – the shape parameters for the signal and the background components. The non-Gaussian function uses a kernel method to estimate the flow velocity distribution. We found that, when it worked, the non-Gaussian function produced moderately superior envelopes than the skewed-Gaussian, however it did not work for all patients. We found that the skewed Gaussian function produced better envelopes than the regular

13

Gaussian function for the majority of patients and comparable envelopes (i.e., no worse) in some patients.
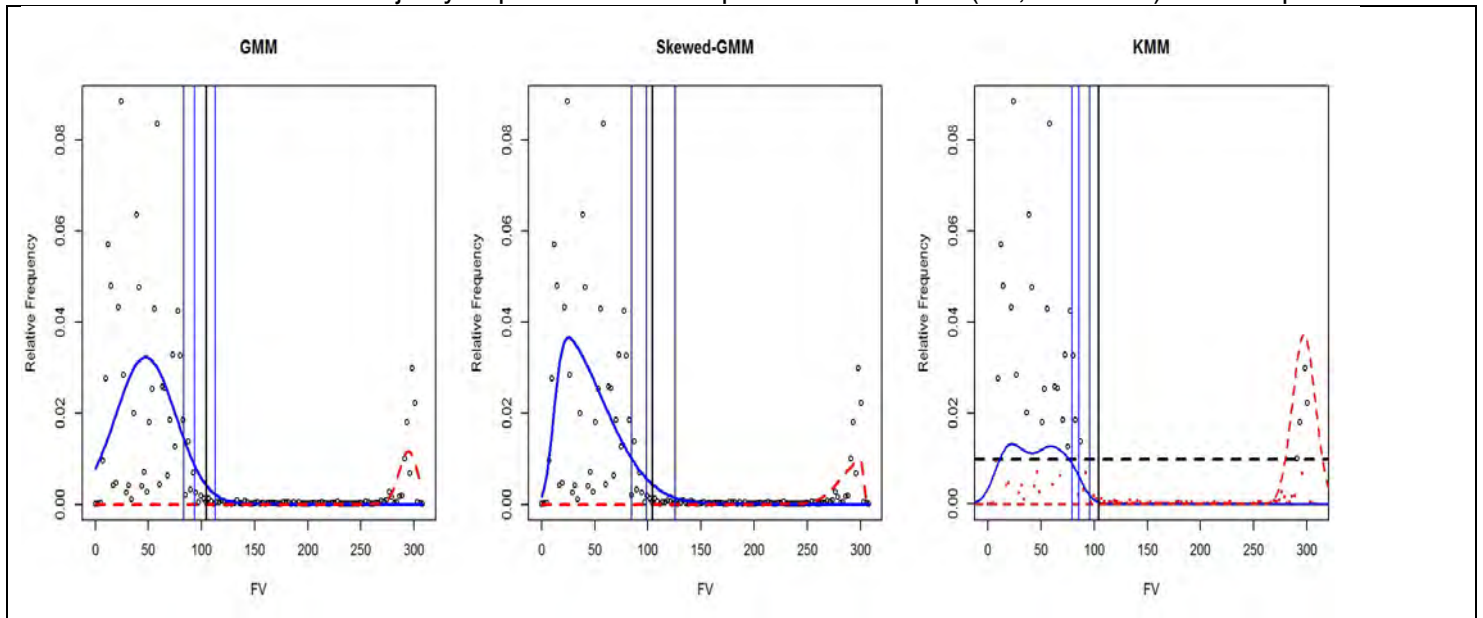

Figure 7. The distribution (more accurately, the probability density function) for the modeled signal (blue curve) and the background (red curve), as determined by mixture models – the Gaussian Mixture Model of Marzban et al, 2013 (GMM, left panel), Skewed-GMM (middle), and Kernel Mixture Model (KMM, right). The blue vertical lines denote the 90th; 95th; 99th percentiles of the signal flow velocity, and the black vertical line marks the maximum FV according to the industry standard Modified Geometric Method.
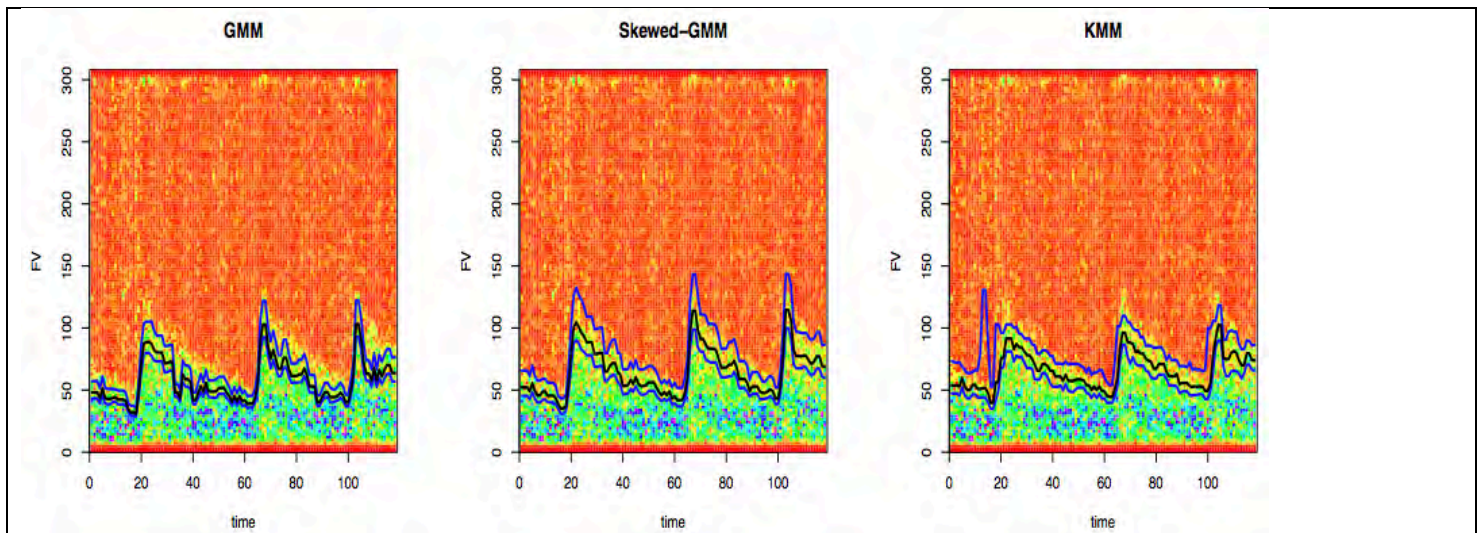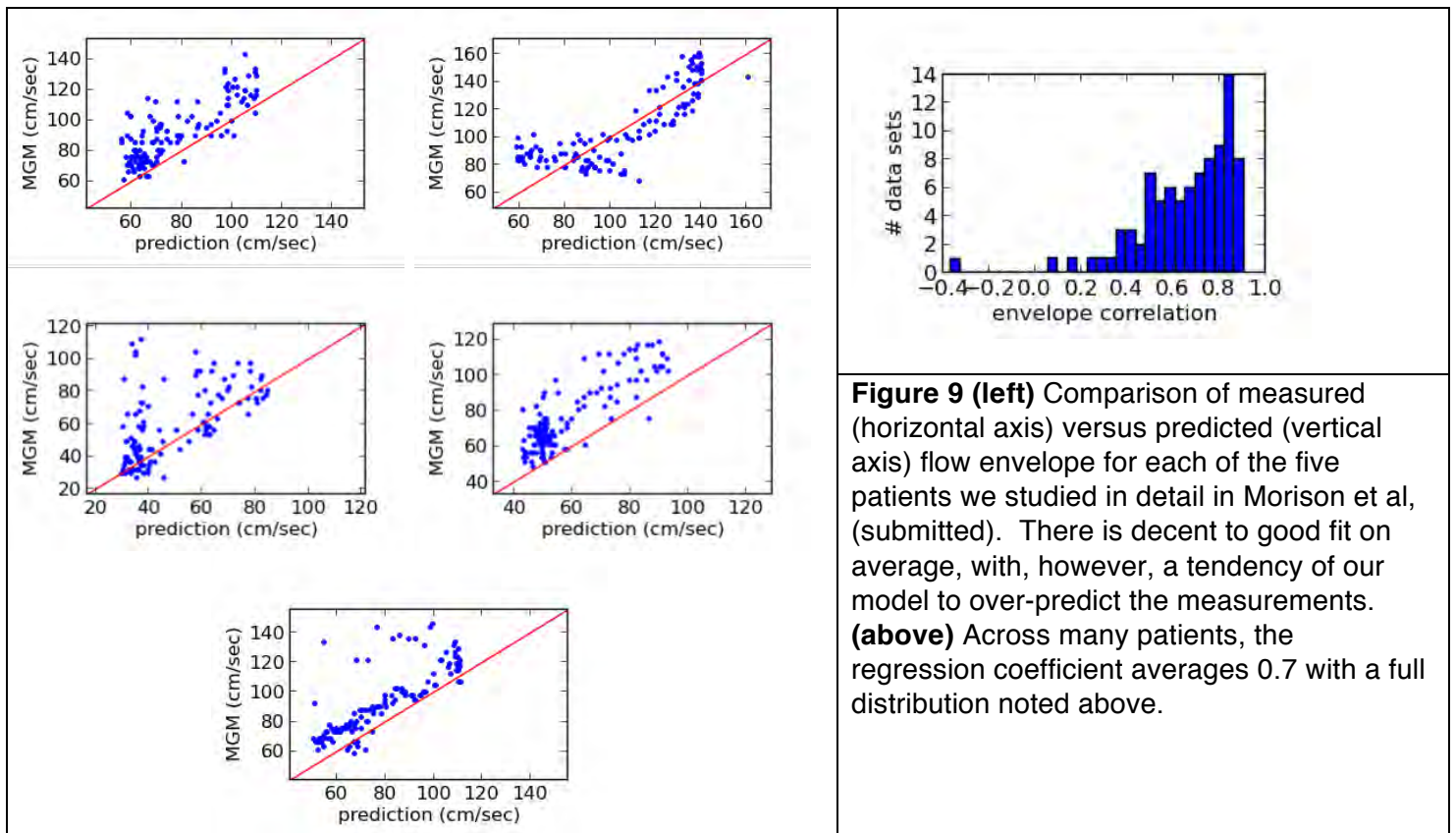

Figure 8. Sample spectrograms from our recently published paper (Marzaban et al. 2016), showing the fit of envelopes at the 90th, 95th, and 99th percentile of signal flow velocity for each of the Gaussian Mixture Model of (GMM, left), Skewed-GMM (middle), and Kernel Mixture Model (KMM, non-Gaussian, right).

(9.2) We have submitted our paper (Morison et al, 2015) on yet another means of calculating optimal spectral envelopes, one based upon a first principles method described in our previous report with final results discussed in Figure 9-14, below.

14

Figure 9 (left) Comparison of measured (horizontal axis) versus predicted (vertical axis) flow envelope for each of the five patients we studied in detail in Morison et al, (submitted). There is decent to good fit on average, with, however, a tendency of our model to over-predict the measurements. **(above)** Across many patients, the regression coefficient averages 0.7 with a full distribution noted above.

Here we use blood flow modeling because it helps us understand the underlying flow dynamics and provides diagnostic value. Spectrograms can often be corrupted by errors, such as limits associated with a finite pulse repetition frequency (setting a cap on the largest measurable velocity), Doppler signal from multiple portions of the vessel, and others. Therefore, if we can apply a model to these data we can improve the estimates of maximum flow. Figure 10 (below) shows the major components of the method for modeling flow. The basic idea is that a recursive estimation function cycles through the actual collected spectrogram data and the predicted spectrogram, and compares the two, iterating many times to improve the agreement between observed and predicted data.
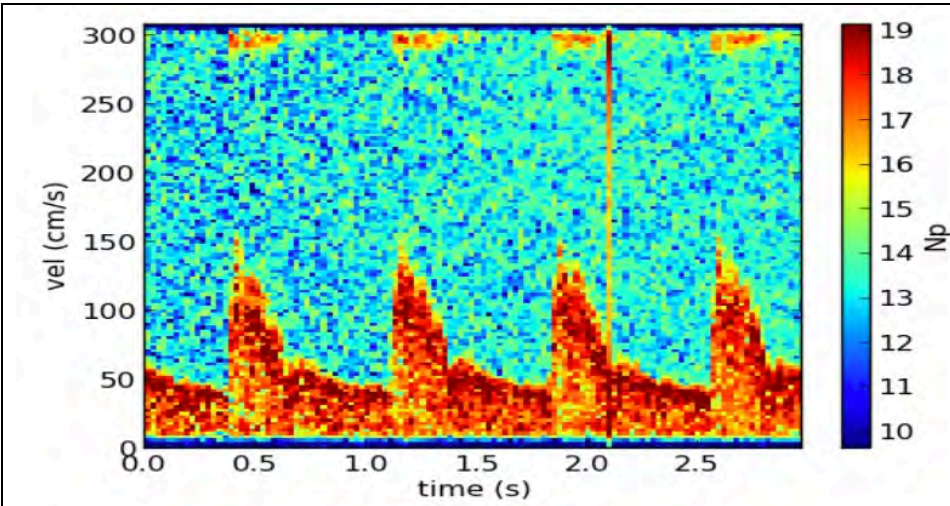

Figure 10. Flow chart showing the proposed methodology for modeling flow using existing spectrogram data.

15
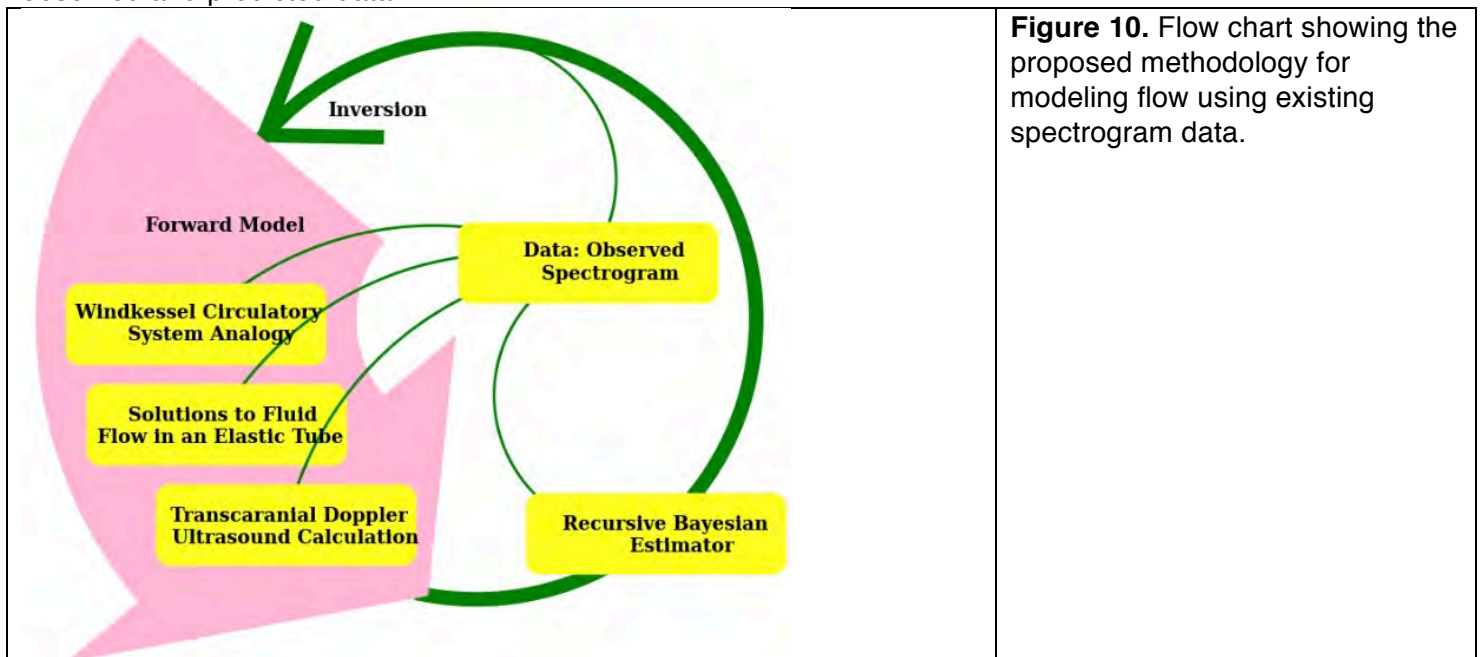
Figure 11. A sample spectrogram used as input to the first principles model of Morison et al.
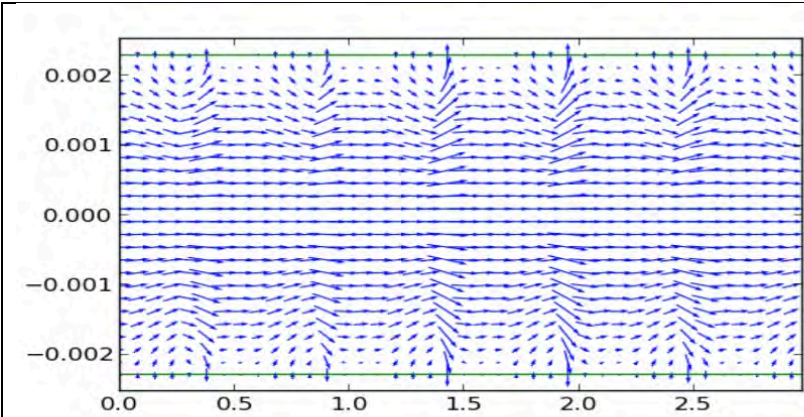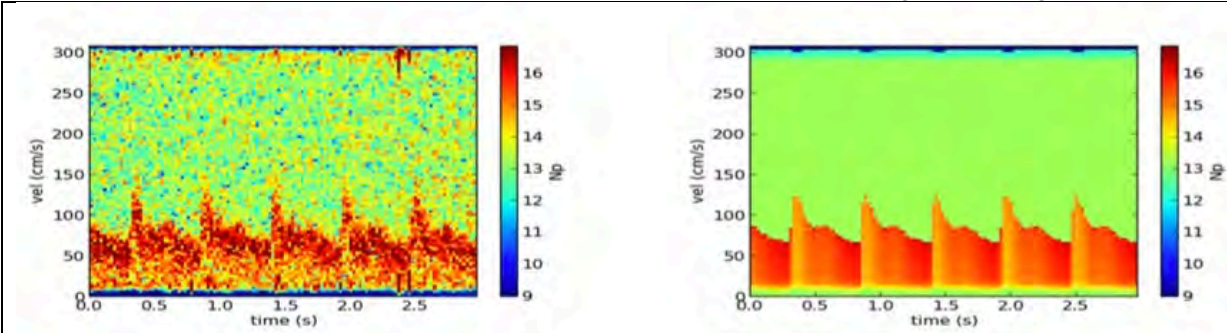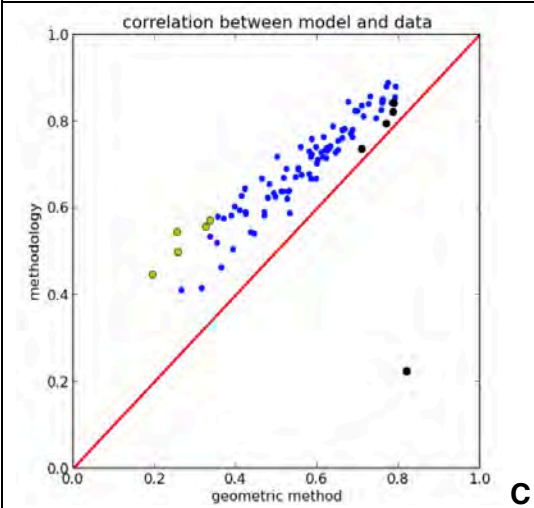

Figure 12. The output flow velocity, where horizontal arrow length is proportional to the axial velocity, and vertical arrow length is proportional to the radial velocity. The artery is shown in the center vertically, and the x axis represents time.

Below is an example of an observed and a predicted spectrogram, using the model we have developed.

A,B

C

Figure 13(A,B). An observed spectrogram (left) and a predicted spectrogram (right).
Figure 13(C). The correlation between our data and the model. Each dot represents a dataset - the vertical coordinate represents the correlation between the observed data and our methodology and the horizontal coordinate represents the correlation between observed data and the null methodology.
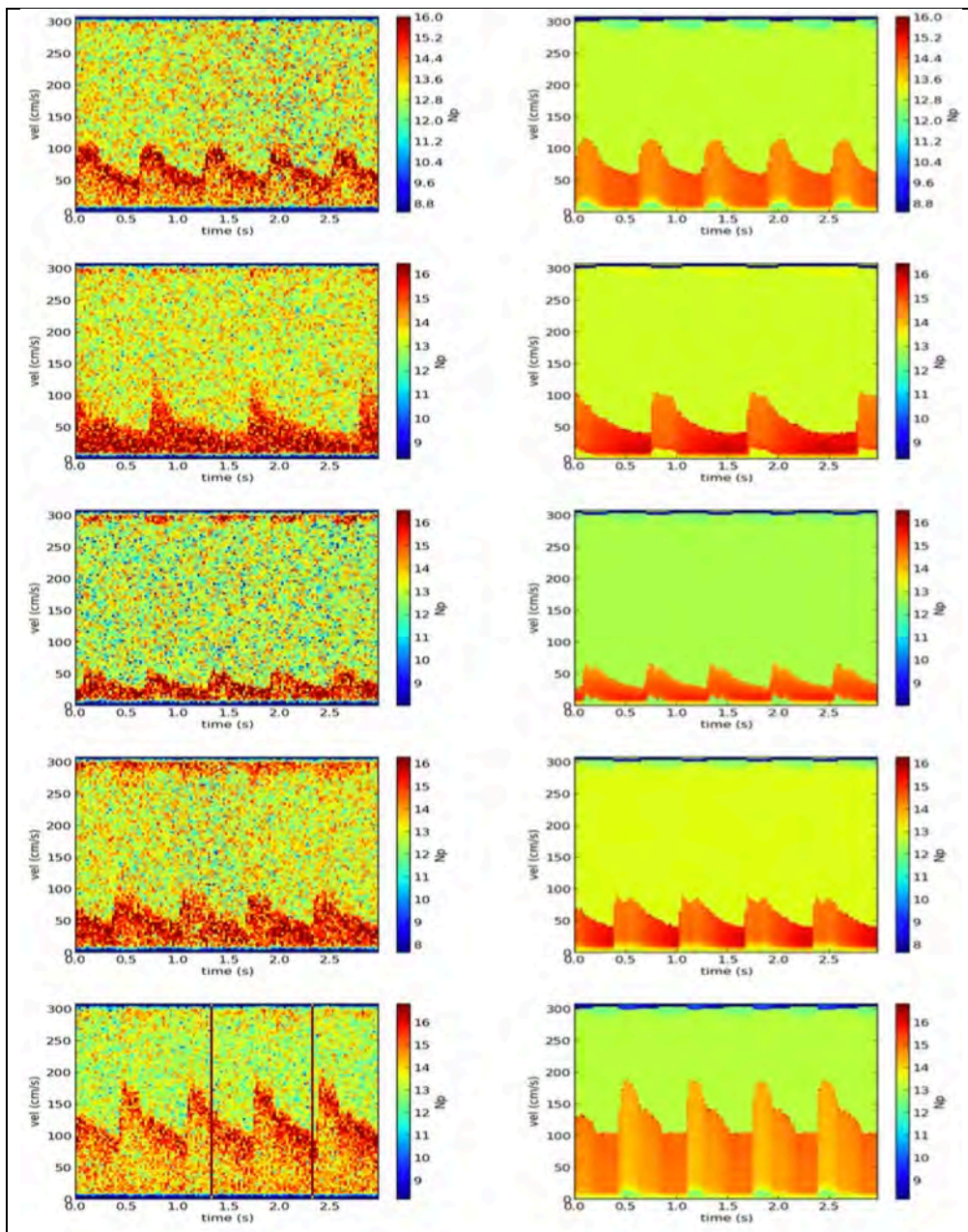
16

Figure 14. Observed spectrograms (left) and predicted spectrograms (right) for which our proposed methodology does best. Each pair of spectrograms represents data from the same patient.

Milestone #5: Deliver software that robustly measures the values of fastest blood flow measured within the MCA and ICA for testing and validation in Aim #1. UW. As described above we have developed two plausible pathways to replace existing commercial algorithms for *calculating* the fastest blood flow with new ones optimized for vasospasm, where the signal to noise ratio is low and the blood flow speeds are high, each testing the limits of the existing system. In future work we will seek additional means of calculating this quantity as well as test these new methods on our existing data sets.

Task 10: *Modify as necessary the TCD's controlling software so as to optimize its ability to <u>search for and locate</u> the point of fastest blood flow within the MCA and ICA for vasospasm patients.* (Q4-Q10) UW; PSI

(10.1) In year 2, we achieved a first iteration of this Task. Our studies with patients made clear the need to have the 'search algorithm' look for points of fastest blood flow deeper than the standard 60 mm within each of the middle cerebral artery and the ICA. We have made that change (Figure 15, reported earlier) and reduced the noise in the collected data.
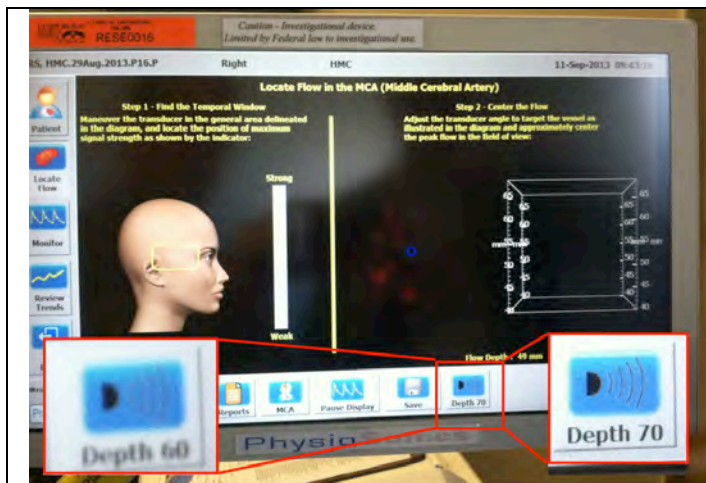
Figure 15. This figure shows the modified user interface that guides the user to setup the automatic TCD to locate the point of fastest blood flow in the middle cerebral artery. Here we photo-document (with a smart-phone camera) that the device can search up to 70 mm deep within the cranium. The user specifies the search depth (60 or 70 mm) and then lets the machine collect its data.

Despite the fact that our algorithm can search over a depth range up to 70 mm within the cranium, our search and locate algorithm thus far tends to lock on to plausible blood-flow maxima within the MCA at shallower depths (40-50 mm) as compared to the depth of vasospasm identified by the commercial TCD (50-65 mm), which facilitates search by hand for the global maximum in blood flow speed along the MCA. In Q9 we identified a potential solution to this issue and worked with our consultant Tom Anderson of Glacier River in Q10 to develop the necessary software changes. In Q11 we updated the search algorithm to allow the user to specify a search volume. Here, we have added a slider bar on the far right of the "Locate Flow" window that allows the user to slide a search box spanning 10 mm depth across the accessible volume (below, Figure 8a,b). We can access volumes between 40 mm and 70 mm. The search volume box can be moved in increments of 1mm. We can move the search volume box for both the MCA and ICA transducers. We continue to advance another portion of the search algorithm design to improve its means of identifying the point of fastest blood flow within a given volume.
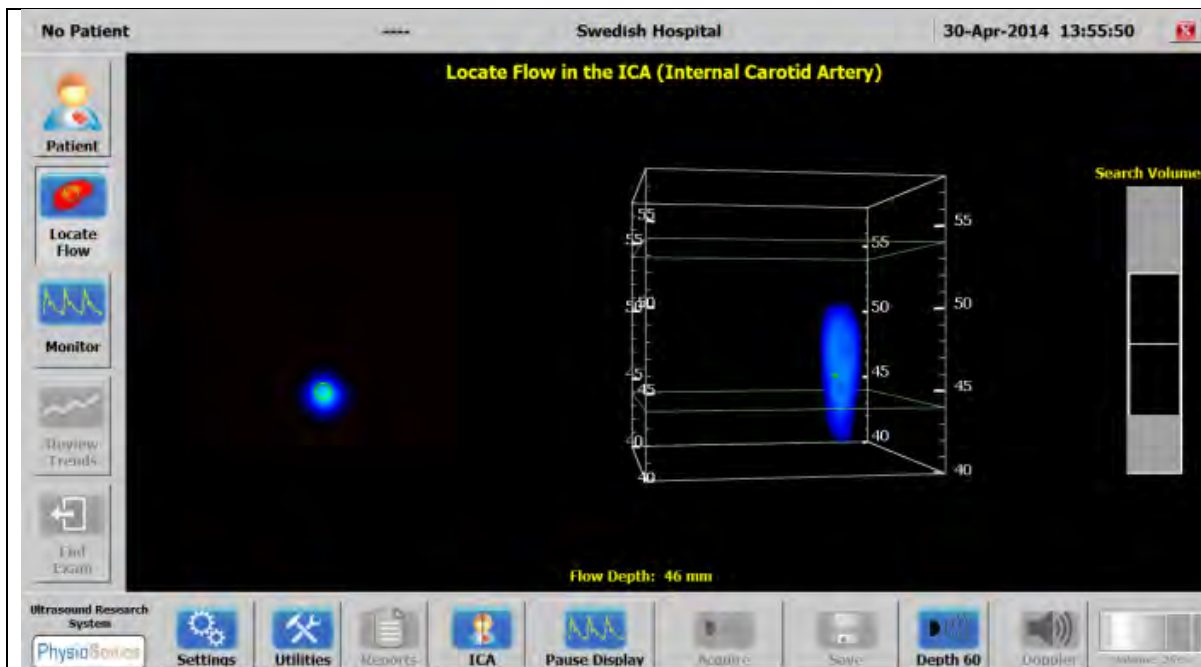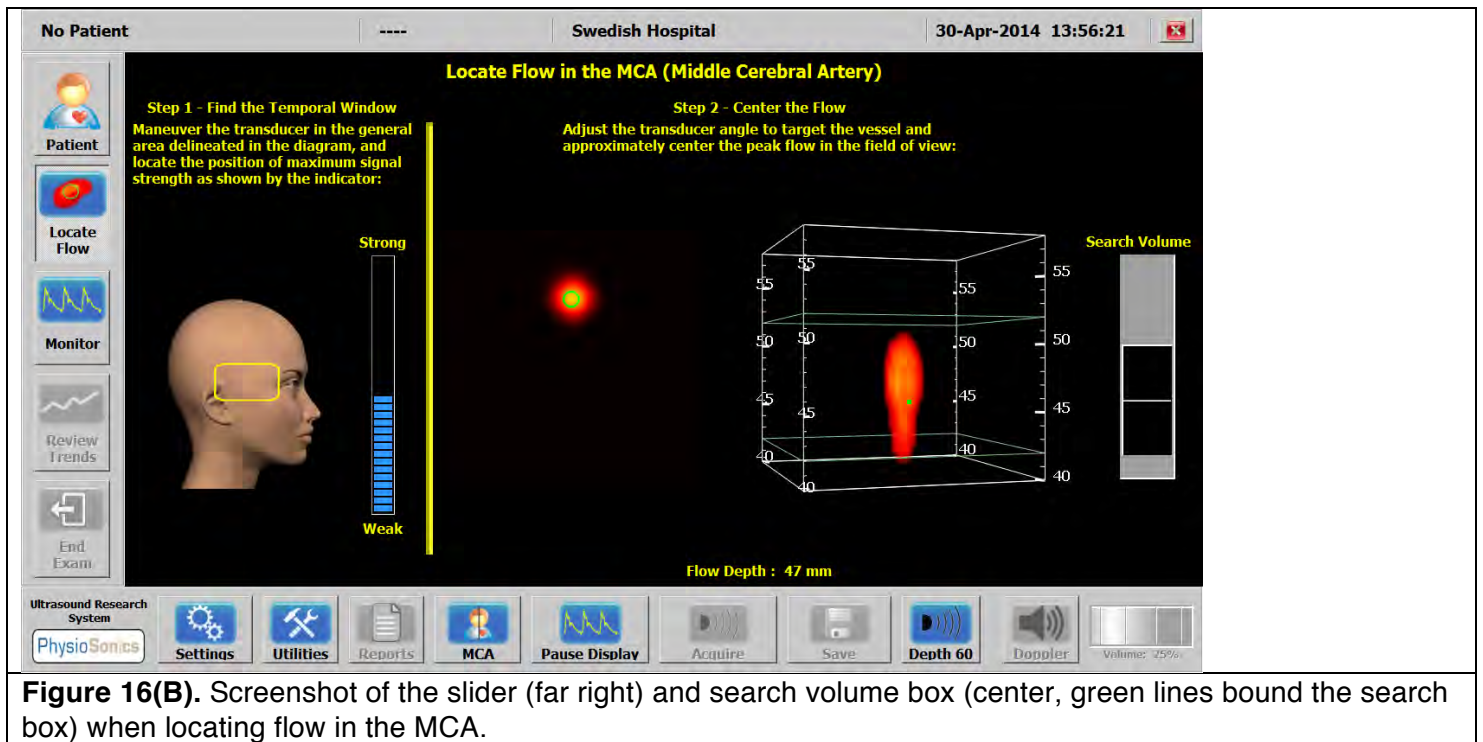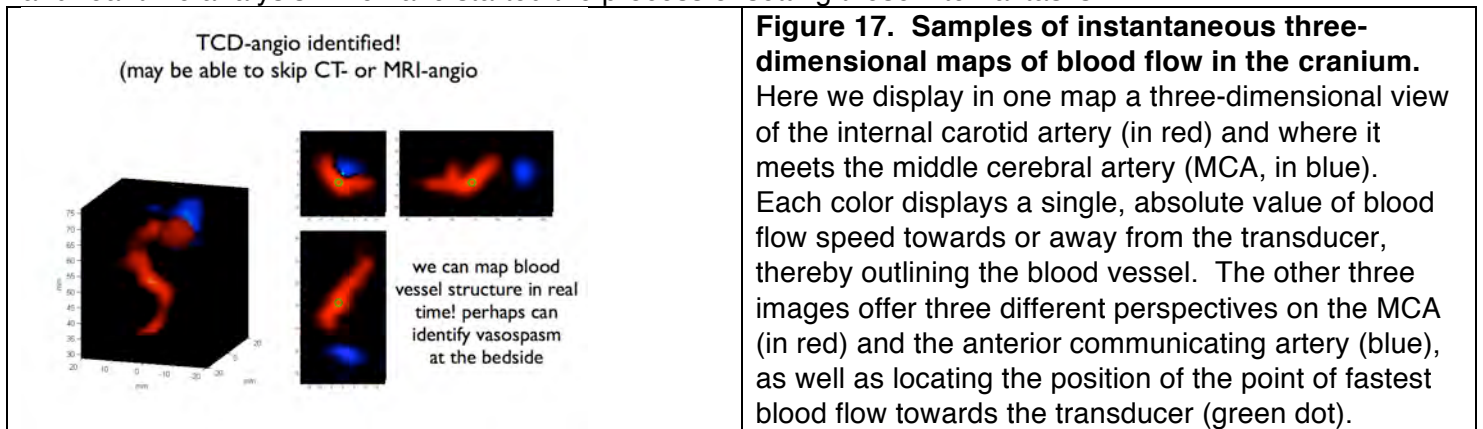

Figure 16(A). Screenshot of the slider (far right) and search volume box (center, green lines bound the search box) when locating flow in the ICA.

18

Figure 16(B). Screenshot of the slider (far right) and search volume box (center, green lines bound the search box) when locating flow in the MCA.

(10.2) We started to determine what it will take to access an internal variable within the aTCD system that facilitates identification of the point of fastest blood flow within the cranium in the region of the MCA, by producing a time-varying map of an iso-surface of Doppler-derived blood-flow speed (Figure 17). The potential benefits the projects are three-fold. (1) We expect to refine the process of identification of fastest blood flow by analyzing how this system collects and processes this internal imaging data. (2) We expect to produce the ability to *visualize* vasospasm by directly measuring the diameter of the blood vessels through analysis of these Doppler maps. (3) Production of these maps may allow assessment of vasospasm in the case of low hematocrit (which can produce large values of blood flow speed without vasospasm0 by superimposition of the identified point of fastest blood flow with the associated vascular anatomy.

This will require substantial work 'under the hood' to make these data readily available for both off-line and real-time analysis. We have started the process of setting these internal tasks.

Figure 17. Samples of instantaneous three-dimensional maps of blood flow in the cranium. Here we display in one map a three-dimensional view of the internal carotid artery (in red) and where it meets the middle cerebral artery (MCA, in blue). Each color displays a single, absolute value of blood flow speed towards or away from the transducer, thereby outlining the blood vessel. The other three images offer three different perspectives on the MCA (in red) and the anterior communicating artery (blue), as well as locating the position of the point of fastest blood flow towards the transducer (green dot).

(10.3) We improved the flow detecting algorithm of the Presto machine, after determining that sometimes the peak "power" flow site detected by the current algorithm was not the desired flow site. Ideally, the algorithm should detect the peak velocity flow site, not just peak power. We therefore provided two alternative algorithms, which are hybrids of power and velocity. The first algorithm searches for peak power with a high velocity boost, and the second searches for peak velocity with a low power cutoff. We also added a Persistence control option, which is accessible in all three of the imaging modes (Figure 18). This was formerly hardcoded in the Power Imaging mode.
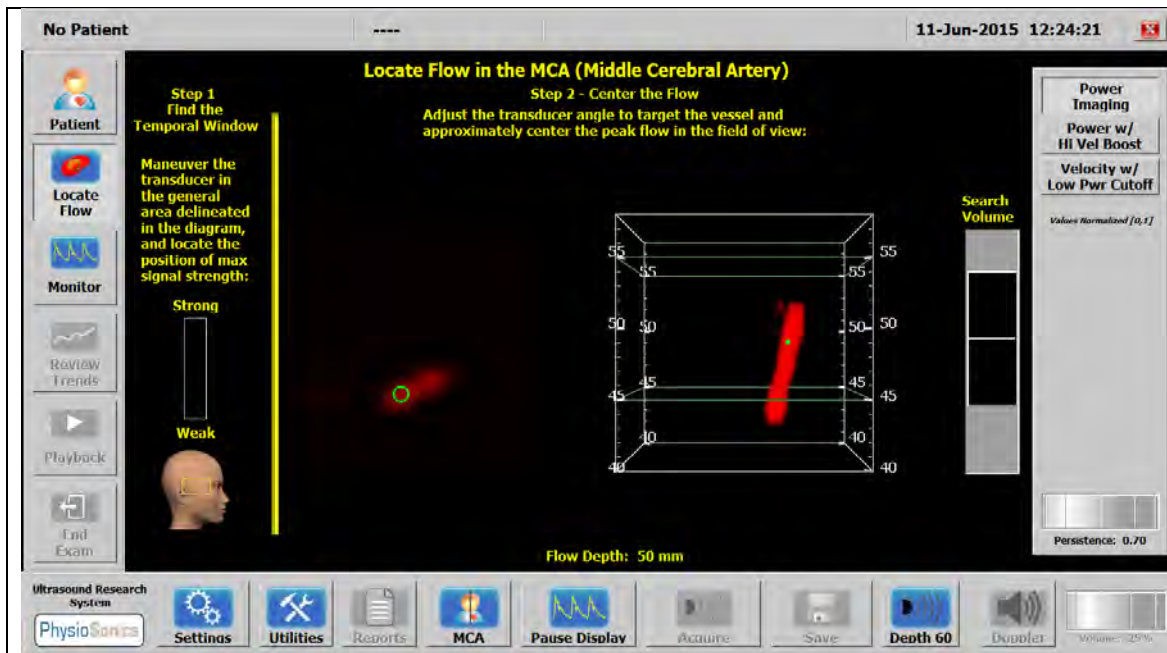
Figure 18. Implementation of the two new search algorithms on the Presto machine. The user can select between the original power imaging mode and the two new algorithms.

The power with high velocity boost algorithm is computed as follows (Figure 19, below):

      if(velocity > threshold for velocity boost) AND (power < low power threshold) AND

        (power is in the same direction as the search direction)

          then the flow estimate is power multiplied by the boost factor

    otherwise

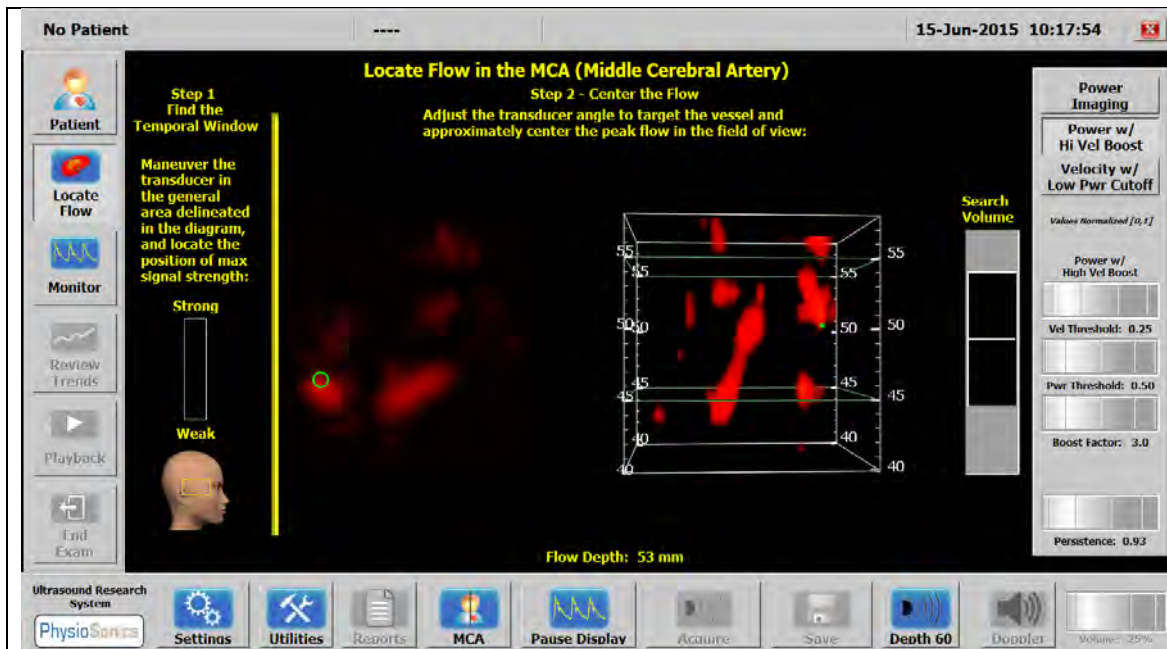   the flow estimate is power multiplied by the derate factor

Figure 19. When the Presto is using the power with high velocity boost search mode, controls are provided specific to that algorithm.

The velocity with low power cutoff algorithm is computed as follows (Figure 20, below):

      if (power > low power cutoff) AND (power is in the same direction as the search direction)

then the flow estimate is velocity multiplied by the color map gain
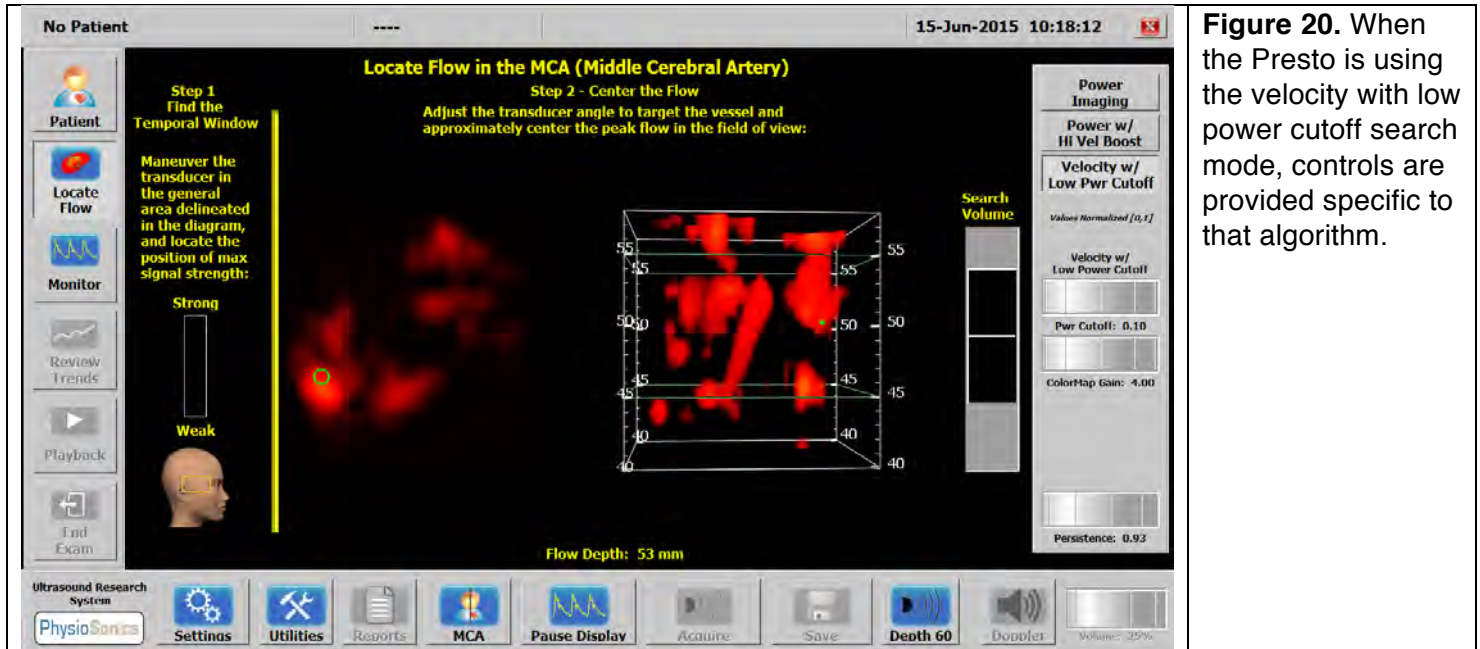
otherwise

the flow estimate is 0

Figure 20. When the Presto is using the velocity with low power cutoff search mode, controls are provided specific to that algorithm.

Milestone #6: Deliver software that optimally identifies the point of fastest blood flow in the MCA and ICA for vasospasm patients for testing and validation for its analysis in Aim #1. UW

Task 11: *Perform pilot study involving 32 patients that tests in a blinded fashion the efficacy of the aTCD compared with a standard TCD system.* (Q10-Q12). UW

(1) We present these results in Figures 4(A) and 5 above, showing agreement (within +/1 12%) between TCD measurements generated via our research TCD device and a clinical TCD device.

Task 12: *Travel to a military medical facility under the sponsorship of Dr. Armonda to determine what changes, if any need to be made to the FDA approved aTCD system for optimal deployment to military facilities.* Q10-12). UW

(1) We instead facilitated visits by Dr. Razmovsky, whose input is evidence in the headset design and in our pursuit of a means of mapping intra-cerebral major blood vessels.

Task 13: *Write up results in a final report for the sponsor, for publication, and within a follow-on proposal that will field trial an aTCD device at a military hospital involving patients with blast-induced TCV. (Q10-Q12). UW*

(1) In the works.

Milestone #7: Report results to the sponsor and begin the transition of this technology to the military.

KEY RESEARCH ACCOMPLISHMENTS

- We have created an improved headset for use in deploying simultaneous MCA and ICA monitoring.
- We have addressed a number of technical obstacles in the Presto system by implementing two new methods for locating the peak flow.
- We have determined a useful enveloping algorithm that tracks well with clinical TCD data and shows improvement in the Presto's peak flow detection over time.
- We have generated a useful technique for modeling blood flow based on actual raw spectral Doppler data.
- In total, we have collected 119 data sets on 83 patients over the 3 years of patient data collection. We believe these low numbers occurred due to a paucity of patients to consent relative to historical averages, and because only one third of the available patients are willing to participate due to their extreme discomfort.

CONCLUSIONS

- We can collect high quality TCD data using the aTCD system from vasospasm patients.
- TCD data collected on the Presto tracks well with standard clinical TCD data when our new enveloping method is applied.
- We have generated an improved TCD headset of direct use for our aTCD system and of likely use for traditional TCD measurements.

REPORTABLE OUTCOMES AND REFERENCES
(copies of these documents are attached to the end of this report, in the Appendix) 24

Marzban C, Illian PR, Morison D, Mourad PD (2013) A Double-Gaussian, Percentile-Based Method for Estimating Maximum Blood Flow Velocity. *J Ultrasound Med*. 32:1913–1920.

Morison D, <u>Marzban C</u>, **Mourad PD.** A model of blood flow based on transcranial Doppler ultrasound. Submitted to *Biomedical Signal Processing and Control.*

<u>Marzban C</u>, Gu W*, **Mourad PD** (2015) Mixture models for estimating maximum blood flow velocity. *Journal of Ultrasound in Medicine.* 35:93-101.

A Model of Blood Flow based on Transcranial Doppler Ultrasound

David Morison,Caren Marzban, Pierre D. Mourad

May 8, 2015

Abstract

Visually evaluating spectrograms produced by Doppler ultrasound has proven clinical utility, as a measure of blood flow. While a physiological understanding underlies such evaluations an explicit model capable of approximating any given spectrogram has not been available. Here, we propose a novel physiological model in which a simple circulatory system drives pulsatile flow through an elastic tube and a system of equations relate the resulting flow velocity field to their corresponding simulated spectrogram. The parameters of the model are then optimized to match measured data from Transcranial Doppler ultrasounds to produce simulated flow patterns and thus provide a quantitative physiological interpretation of the spectrogram.

1 Introduction

Modeling blood flow has been a topic of extensive research [1],[2],[3] and [4]. It is important not only for the purpose of understanding the underlying dynamics [5] and [6], but also for its diagnostic value [7] and [8].

Transcranial Doppler Ultrasound (TDU) provides one method for measuring blood flow [9] through the middle cerebral artery. The measurements are generally displayed in the form of a spectrogram. A spectrogram is a measure of the intensity of acoustic return to TDU as a function of time and velocity [1] Such spectrograms, however, are generally corrupted by a number of errors, including limits associated with a finite pulse repetition frequency (which sets

---

[1]In common usage the term spectrogram refers to a function of time and frequency; but

a cap on the largest measurable velocity), Doppler-signal return from multiple portions of the blood vessel of interest, inadequate acoustic windows, and other sources of error. A basic assumption in examining Flow Velocity (FV) data is that there exists an underlying spectrogram which adheres to certain physical constraints. For example, at a given time, the brightness/amplitude of a spectrogram is expected to drop to zero at a well-defined FV value corresponding to a maximum FV_{max}. However, observed spectrograms usually do not reflect such behavior. Also, observed spectrograms are often contaminated by random noise, i.e., random errors which cannot be attributed to any physical constraints. A physics- (or physiologically)-based model is required to allow one to attribute physical meaning to an observed spectrogram.

The approach proposed in this paper involves both statistical and physical models. Statistical models usually involve parametric, mathematical expressions whose structure is often dictated by the convenience of estimating their parameters. Regression models are canonical examples of such models ([11] and [13]). By contrast, physical models begin with physiologically-relevant components whose mathematical properties are well-understood, and describe the overall phenomenon (e.g., blood flow) by an assembly of such components. The awkward and often ill-conditioned problem of fitting the free parameters of a physical model to data is referred to as an inverse problem. [2] Physiologically based blood flow models of the type examined here have been considered in the past, but the model parameters have not been estimated to optimize the difference between observed and predicted spectrograms. For example Mirsa et al.[8] models blood flow through a constriction, but at no stage in that work is a spectrogram used to estimate the model parameters. Similarly, Garcia et al.[10] uses a physiological model to infer a velocity field from Doppler ultrasound but use a variable focus location in a relatively large area rather than a spectrogram. Notable examples of paired physiology and ultrasound models are given by Rune Aaslid and David H Evans. Aaslid offers [19] a sophisticated but proprietary simulation and teaching tool and Evans employs a model of Doppler ultrasound in multiple physiological scenarios. So precedents exist for the forward model used in this work, however those models are not fit to observed data. When a

---

in the present case there is a one to one correspondence between frequency and Doppler velocity. Also a spectrogram is a function of time in the sense that it is recorded over time.

[2]The distinction made here between statistical and physical models is fuzzy, but extreme examples are [14],[13] and [15],[16], respectively.

spectrogram is fully employed as an objective function, in for example Fernando et al.[11] and Marzban et al.[13], the focus of the work is an envelope not a 2-D flow velocity field. One novel feature of the proposed method is the manner in which a full physiologically-based blood flow model is utilized, and its parameters are estimated from an entire spectrogram. Part of the estimation method is a simple instance of *Recursive Bayesian Estimation* (RBE)[17] which involves iteratively making observations, and revising estimates about the system from which those observations originate. RBE has been proven useful in a wide range of applications [18], including the modeling of blood flow [20] and [21].
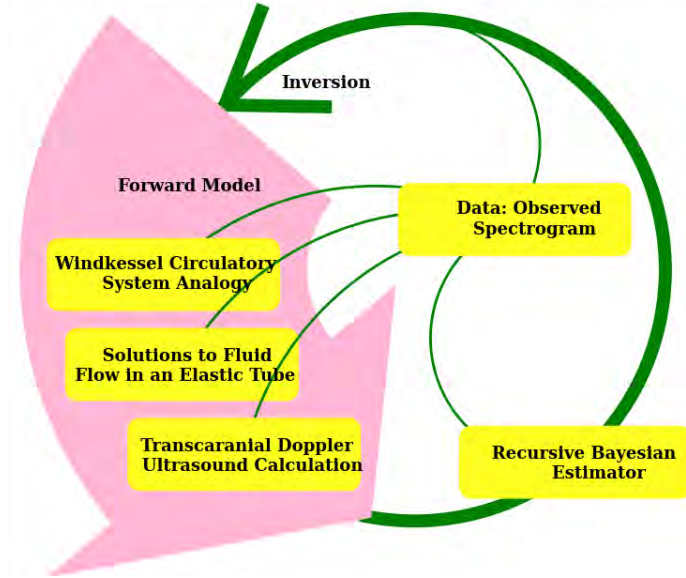

Figure 1: In the proposed methodology the forward model consists of several components, each with parameters which are to be estimated from observed spectrograms. The parameters are initialized, a recursive Bayesian estimator picks a time series through the output of the forward model which best matches the data. Then the predicted spectrogram is compared with the observed spectrogram and this whole process iterates with the goal of improving the agreement between observed and predicted.

The flow chart in Figure 1 highlights the major components of the methodology. As shown the forward model is comprised of three sub-models. First, a Windkessel model [3] in the style of [22] produces a one dimensional time series of FV_{max}. Second, solutions to Navier-Stokes equations in an elastic tube developed by [1] and [2] are set to match the FV_{max} boundary conditions

---

[3]i.e. an electric circuit analogy to the circulatory system

and return a 2-D flow field time series. Third, an equation is proposed to calculate the spectrogram resulting from measurement of the 2-D flow field with TDU. With arbitrary free parameter values the forward model outputs realistic simulated spectrograms, but the output does not resemble any particular patient. The purpose of the methodology developed here is to invert the forward model and find input parameters corresponding to the observed spectrogram of any patient. Most of the free parameters are constant for a given patient. For example neither the viscosity of blood (μ) nor the angle of the transducer relative to the artery (Φ) are assumed to change within a data set. The phase of a patient's cardiac cycle (θ) is expected to constantly advance in time albeit irregularly. Given values for all other free parameters the forward model specifies a spectrogram for any value of θ. The RBE combines an observed spectrogram recorded over time with a predicted spectrogram modeled over the domain of θ in order to output a predicted time series of θ. With the predicted time series θ the predicted spectrogram is compared directly to the observed spectrogram. This comparison feeds back into refined values for the free parameters. The whole process repeats, seeking a forward model that best matches the patients data. Seeking to invert our model with this methodology many iterations of the loop are performed with ad hoc shortcuts and/or in parallel.

2 Data

Ninety-six recorded spectrograms are examined, 73 of which are collected with a Spencer Technologies PMD 100 TDU device (Spencer Technologies, Inc., Seattle WA) at the following hospitals: Harborview Medical Center (Seattle, Washington), Columbia University Medical College (New York City, New York) and the University of Texas Medical School at Houston, Texas. The remaining 23 spectrograms are collected from patients at Harborview Medical Center with the Presto TDU device currently under development (PhysioSonics, Inc., Redmond WA). Of the 23 spectrograms collected with the Presto device the data sets are anonymized (as are all of the data sets) but a few appear to be drawn from repeated patients, suggesting fewer than 23 separate patients.

All of the spectrogram data analyzed are archived at a sample rate of 40 Hz and with 128 velocity bins from a bin-center at 0 cm/s to a bin-center at 308 cm/s. All patients experienced traumatic brain injury (TBI), with

4

the majority (59 out of the 73 Spencer data sets) closed head TBI and the remaining experiencing penetrating injuries. Additionally five of the patients also exhibited vasospasm.

The spectrograms for the 96 patients are complex and varied across patients. Although the spectrogram for almost every patient appears to be consistent with what one might expect from an ideal spectrogram, no simple ideal spectrogram emerges as a viable candidate when multiple patients are examined. In fact, the spectrograms for 9 of the patients data collected with the Spencer device are sufficiently complex to have failed a commonly-used envelope-detection algorithm, referred to as the modified geometric algorithm [11]. Figure 2 shows the spectrogram as measured by a Spencer TDU de-
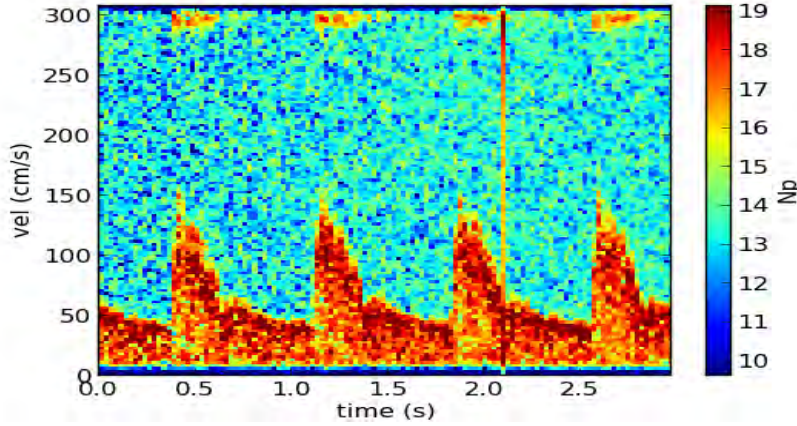

Figure 2: The observed spectrogram for one patient illustrating many relevant phenomena. FV_{max} is easy to pick out as a function of time demarcating the acoustic clutter (i.e. back ground static) above from the signal of interest below. Aliasing is visible as periodic bright spots near the top of the velocity axis lining up with systole. A variable brightness or shading is clear within the signal of interest, in this case bright near FV_{max} and dim near velocity equals zero. Also the "blip" right after two seconds is an example of non-additive noise.

vice. Note the varying shading in the "body" (i.e., the signal of interest in the lower portion) of the spectrogram, in contrast to the relatively constant background static. It is important to note that the amplitudes shown in this figure are in the dimensionless units of nepers (Np) or the natural log of the archived amplitude. Indeed, all of the following analysis is performed on the logarithm of the observed spectrogram amplitude. The logarithmic transformation is motivated by the empirical result that the histogram of the
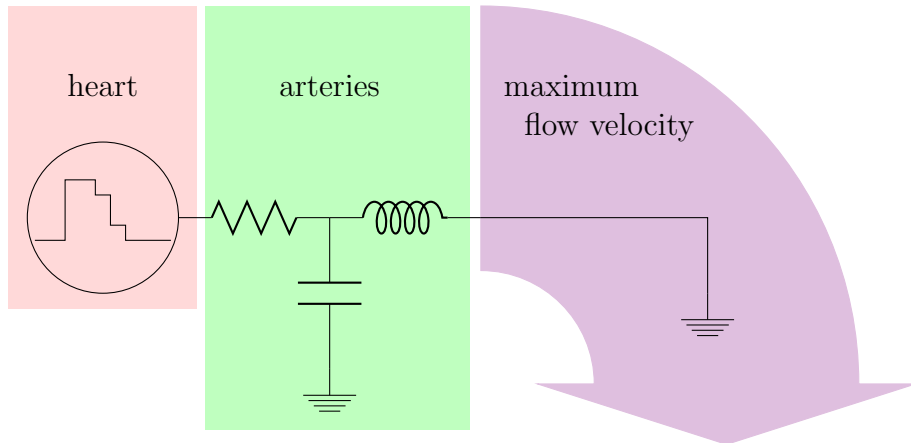
5

Figure 3: The circuit diagram corresponding to the Windkessel model used

logarithm of the amplitudes is bell-shaped, where as without the logarithm the histogram is heavy-tailed.

The data sets have been limited to three second excerpts. Three seconds was chosen for the reason that, for most patients, it is long enough to show multiple cardiac cycles yet short enough to display the details of each cycle. Sampled at 40Hz this leads to 120 time steps considered from each patient.

3 Methods

3.1 Windkessel Model

Driven with a four level square wave, the circuit illustrated in Figure 3 can produce realistic time series of FV_{max}. The use of a four level square wave is a computational expedient, rather than a physically based assumption. A more physically reasonable Windkessel model of the heart, with it's valves and nervous system, would require nonlinear circuit elements. When attempting to invert the forward model such a nonlinear circuit would become a computational bottle neck, while the circuit in Figure 3 may be simulated at negligible computational cost. Free parameters associated with the various components of the Windkessel model are tabulated in Table 1. As described in text, most of the free parameters are constant, while phase in cardiac cycle (θ) changes with time. Table 1 is written to present the true count of free parameters. In practice the domains of the free parameters are constrained

in an ad hoc manner, for example a linear combination of r and the V's are adjusted twice per iteration of the outer loop in 1. So there are ten constant, plus one dynamic, free parameters but in practice their domains are interrelated. An example of the Windkessel model output is shown in Figure 4.

parameter	symbol	domain	units (abstract)
phase in cardiac cycle	θ	0 to 2π	rad
heart rate	ω	0.6π to 6π	$\frac{1}{second}$
resistance	r	0 to 1	$\frac{pressure}{flow}$
capacitance	c	0 to 10	$\frac{flow \cdot time}{pressure}$
inductance	l	0 to 0.2	$\frac{pressure \cdot time}{flow}$
dwell a	Δ_a	0.05 to 0.25	$time$
dwell b	Δ_b	0.05 to 0.25	$time$
dwell c	Δ_c	0.00 to 0.20	$time$
amplitude a	V_a	0.0 to 1.	$pressure$
amplitude b	V_b	0.0 to 1.	$pressure$
amplitude c	V_c	1	$pressure$

Table 1: The dynamic and fixed parameters introduced in the Circulatory System Calculation component of the model. The physical units are general because the Windkessel model is an analogy, "flow" will be scaled to an FV_{max} time series in cm/s before it is input to the flow field calculation.

3.2   Flow Field Calculation

The time series FV_{max} constitutes the boundary condition for a fluid dynamic model of blood flow in the middle cerebral artery. In order to use solutions developed by [1] and [2] the middle cerebral artery is treated as an elastic tube, and blood is assumed to satisfy the incompressible Navier-Stokes equations. The tube is assumed to be straight; this assumption is reasonable because although the middle cerebral artery is convoluted, the typical radius of curvature along the artery is larger than the radius of the artery itself. The vessel wall is assumed to be thin, allowing one to treat it as a Hookean membrane[23], i.e., the 2-dimensional generalization of an ideal spring. We seek solutions for radial and axial velocities of the form $v(r,t)$ and $u(r,t)$, where r is the distance from the axis. As such, the solutions are rotationally symmetric, and there is no angular velocity. As is often, done
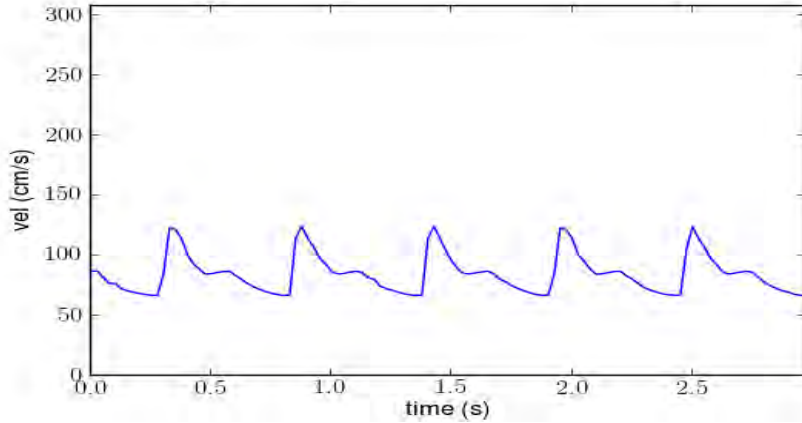
7

Figure 4: An example of FV_{max} produced by the circuit shown in Figure 3

approximations are made in order that solutions may be obtained through a Fourier decomposition of the forcing. In the end, two degenerate modes of wave propagation are found, for each harmonic component. In most prior work an appeal to experiment has been made at this point to determine the mode of wave propagation. In our case the relative phase and amplitude between the modes becomes a free parameter. The forward model inversion embodied in the flow chart of Figure 1 becomes an effort to determine the mode of wave propagation for each patient. The mechanical properties of blood and vessel walls are the subject of many studies [27] [28] [29] [30] [31] [32] [33] which provide useful bounds for the free parameters (Table 2) within which to optimize their estimated value from data. The output of model of blood flow in the middle cerebral artery is shown in Fig. 5. Typically, the radial velocity magnitude is much less than of the axial velocity magnitude; here, they have been scaled to achieve visual clarity. It may be tempting to ignore the lower amplitude radial component in favor of the higher amplitude axial component; however, because the observed spectrograms span the full domain of velocity, including near-zero velocity, the scale disparity between the two components does not justify discarding the lower amplitude velocities. The mathematical details of the flow model developed here are similar to that developed in [23] [4].

---

[4]except that Equations 17.134 and 17.135 seem to be in error and the reader will need to derive the correct equations from 17.128, 17.129, and 17.131

8

parameter	symbol	domain	units
density of blood	ρ	1.06	$\frac{g}{cm^3}$
viscosity of blood	μ	3 to 4	centipoise
density of vessel wall	ρ_w	0.98	$\frac{g}{cm^3}$
equilibrium radius of vessel	a_0	0.15 to 0.25	cm
thickness of vessel wall	h	5 to 20	% of a_0
Poisson's ratio of vessel wall	$\hat{\nu}_w$	0.3 to 0.7	dimensionless
Young's modulus of vessel wall	E	40 to 100	$\frac{g}{cm \cdot s}$
relative amplitude of "+" mode	X_+	unit normal	complex plane
relative amplitude of "-" mode	X_-	unit normal	complex plane

Table 2: The fixed parameters introduced in the Flow Field Calculation component of the model.
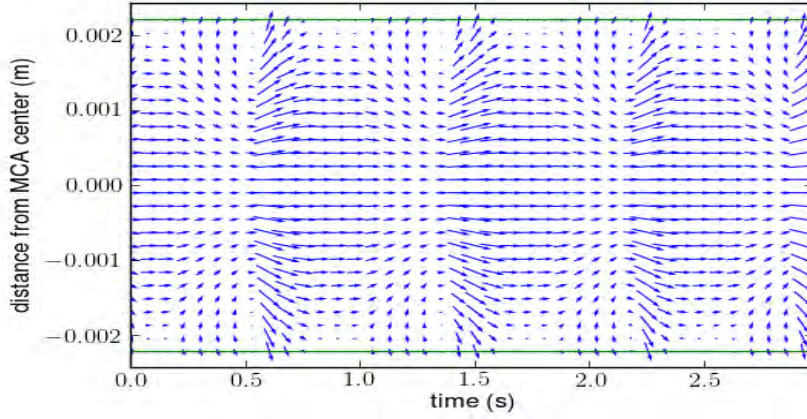

Figure 5: The output flow velocity is shown. The horizontal arrow length is proportional to the axial velocity and the vertical arrow length to the radial. The arrow base positions increment horizontally with time, and vertically with radial distance. To make the graphic more intuitively clear the artery center is shown in the center vertically and reflected axial velocities and radial positions are plotted.

9

3.3 Spectrogram Calculation

The preceding steps in the proposed model produce a 2-D flow velocity field. TDU, however, produces a spectrogram, i.e., a time series of the histogram of the volume corresponding to a Doppler velocity v where volume is assumed to be proportional to the total number of scatterers [24]. In order to compare the simulated blood flow velocity field to the observed Doppler ultrasound, therefore, a spectrogram must be derived from the modeled velocity field. The TDU considered here interrogates only the flow velocity
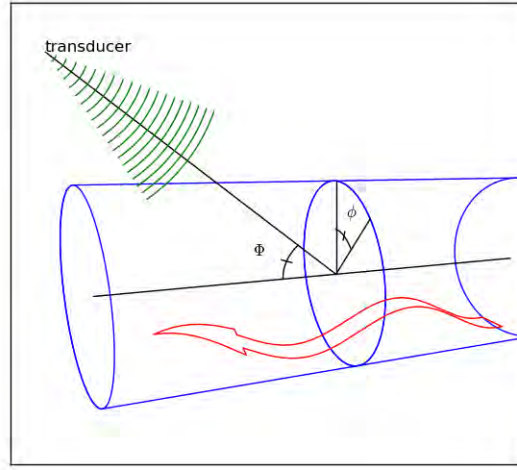

Figure 6: An overview of the off-bore angle Φ and the polar angle ϕ. This geometry determines the Doppler velocity from the transducer's perspective on the axisymmetric flow field.

field component parallel to the transducer axis. Though the simulated blood flow is axisymmetric the transducer is not assumed to be aligned with the middle cerebral artery. Introducing an off-bore angle Φ, the speed toward the transducer v' is given by

$$v'(r, \phi, \Phi) = v_{axial}(r) \cos \Phi + v_{radial}(r) \sin \Phi \cos \phi \ , \tag{1}$$

with ϕ the angle in cross section of the artery (see Figure 6). Said differently, ϕ is the polar angle around the symmetry axis of the artery and Φ is the angular misalignment between the two symmetry axes, that of the ultrasound

focus, and that of the artery. The location of the TDU focus is assumed to be offset from the artery center and variable in width. A finite focus volume enters into the calculation of a spectrogram simply as a location dependent weighting function $f(r, \phi)$. Values of v' from equation 1 are shown in Figure 7. The flow velocity field is the same as is shown in Figure 5 but in that graphic the flow is displayed over time and a diameter of the artery. This graphic illustrates the effect of Φ and ϕ with a snapshot of v' throughout a cross section of the artery. An ideal spectrogram is a measure of how much
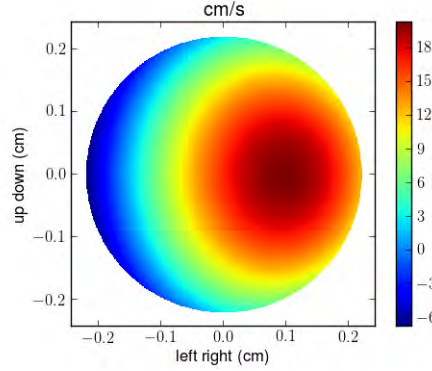

Figure 7: The Doppler velocity component, v', is shown as a scaled color in the symmetry plane of the artery. As shown r and ϕ would be polar coordinates in the Cartesian coordinate axes, with $\phi = 0$ illustrated as being the right. For this figure a relatively large off-bore angle of $\Phi = \frac{4\pi}{9} rad = 80°$ is chosen to illustrate the ϕ dependence of equation 1. In cases of Φ closer to 0 the axial contribution to the Doppler velocity dominates and the second term in equation 1 is not apparent.

volume within the focus area is moving at a velocity v In other words, given time t and velocity v the spectrogram is a measure of the infinitesimal volume for which $v' = v$ as a function of time. An ideal spectrogram $s_{ideal}(v)$ can be defined as

$$s(v) = \lim_{\epsilon \to 0} \frac{1}{2\epsilon} \text{Area in } r, \phi \text{ such that } |v'(r, \phi) - v| < \epsilon \qquad (2)$$

where the area is understood to be either inside the ultrasound focus or to be weighted by some function defining the focus $f(r, \phi)$. The ideal spectrogram is the infinitesimal area for which the Doppler component of the flow velocity field inside the ultrasound focus is equal to the ideal spectrogram velocity. It is relatively straightforward to show that for a broad class of v', the limit

11

in equation 2 can be written as

$$s(v) = \oint_{v=v'} \frac{f(r, \phi) \, dl}{|\nabla v'|} \tag{3}$$

where l is any parameterization of contours for which $v'(r, \phi) = v$. The relationship between an ideal spectrogram and a flow velocity field has been studied by Evans [4], but not in integral/closed form as in equation 3. The focus $f(r, \phi)$ is defined in the symmetry plane of the artery and specifically to be a 2-D Gaussian inside of the artery and zero outside.

$$f(r, \phi) = \begin{cases} e^{-\frac{(r\cos\phi - \text{offset}_x)^2 + (r\sin\phi - \text{offset}_y)^2}{2\text{width}^2}} / \left(2\pi\text{width}^2\right) & , r \leq a_0 \\ 0 & , r > a_0 \end{cases} \tag{4}$$

This 2-D Gaussian introduces three free parameters: offset_x an offset in the symmetry plane of the artery parallel to $\phi = 0$, offset_y an offset in the symmetry plane of the artery parallel to $\phi = \frac{pi}{2}$, and width a parameter governing the width of the focus. When width is large i.e. near $2a_0$, the offset parameters have little effect on the predicted spectrogram, reverting to the case of uniform insonification. In practice the bloods Doppler velocity v' is approximated with a piecewise planar triangular surface and the integral in equation 3 is approximated with a sum. This is one of the more computationally expensive steps in the methodology. To avoid performing this calculation twice per iteration of the outer optimization loop in the flow chart Figure 1 the spectrogram due to the tissue motion is calculated with a quick approximation. Additionally, the observed spectrogram is assumed to differ from the ideal spectrogram by the addition of two types of noise and by the unknown acoustic reflectivity of blood and tissue.

$$S(v, \theta) = B_b s\left(v_{axial}(\theta), v_{radial}(\theta)\right) + B_t s\left(\eta(\theta), \xi(\theta)\right) + B_0 \tag{5}$$

$$Z(v, t) = S(v, \theta(t)) + N(v, t) \tag{6}$$

Here S is the idealized spectrogram output by the forward model over the domain of spectrogram velocity v and phase in the cardiac cycle θ. Z is the observed spectrogram data which differs from S by zero mean one dimensional Gaussian random variable (i.e. noise) N and an unknown relationship between the domain variables θ and time. The free parameters B_0, B_b and B_t are the acoustic brightness of the background clutter, blood and tissue respectively.

parameter	symbol	domain	units
off-bore angle of transducer	Φ	$\tan^{-1}\sqrt{\frac{N^2+N^2}{2}}$	radians
vessel wall Doppler spread	σ_w^2	0 to 3	$\frac{1}{dv}$
focus width	focus_width	0.1 to 2.	$\frac{1}{a0}$
focus offset x	focus_offset_x	N	$\frac{1}{a0}$
focus offset y	focus_offset_y	N	$\frac{1}{a0}$
reflectivity of blood	B_b	$-\infty$ to ∞	Np
reflectivity of tissue	B_t	$-\infty$ to ∞	Np
background clutter	B_0	$-\infty$ to ∞	Np

Table 3: parameters introduced in the Spectrogram Calculation component of the model. The abbreviation Np stands for neper of the spectrogram amplitude. A neper is to the natural log as a decibel is to a base ten logarithm.

3.4   Recursive Bayesian Estimation (RBE)

The forward model outputs an ideal spectrogram $S(v,\theta)$, an expected amplitude as a function of velocity and phase in the cardiac cycle. Of course the observed spectrogram $z(v,t)$ is not naturally delineated into cardiac cycles. Within a recursive Bayesian framework the observed spectrogram $z(v,t)$ is combined with $S(v,\theta)$ to produce a posterior probability density function (PDF) over θ which evolves in time. The location of the maximum value of this posterior PDF is taken as an estimate of the time series $\theta(t)$. In sum-
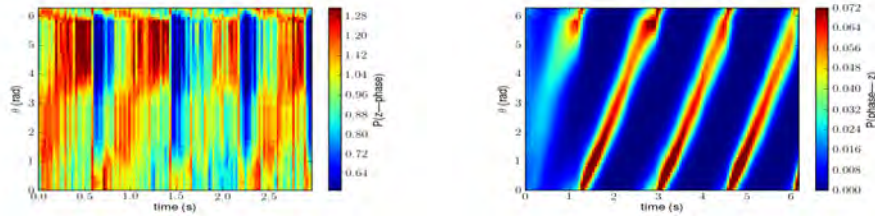

Figure 8: On the left is an example of the likelihood of the data, from one patient, conditioned on θ as a function of time. On the right is the cumulative probability density function over θ, as a function of time. For the earliest time steps, the cumulative PDF is ambiguous with regards to the value of θ, but soon a well defined mode in θ develops. The mode advances in time roughly in agreement with $\frac{d\theta}{dt} \approx \omega$.

mary, the forward model produces an ideal spectrogram over θ. The RBE compares each time step of the observed spectrogram to the ideal spectro-

gram at each each value of θ. Then the RBE uses the information that θ advances in time at approximately the heart rate (ω) to predict a time series of θ. RBE's have a long history of use in signal processing and the details of any given implementation may vary dramatically. Stylistically the RBE used here is similar to one used in Nodestar [18] in a few ways. The PDF of the state variable (θ in our case) is stored as a relatively fine grained histogram. The presumed relationship between the state variable and a measurements of the system is not linearly approximated. Also, discretized numerical integration is used at each time step to marginalize over previous values of the state variable. These attributes are all in contrast to the most typical RBE, a Kalman filter. Our RBE is formulated as it is to accommodate a relatively complex relationship between θ and $S(v, \theta)$.

3.5   Parameter Refinement and Feature Extraction

Each of the components of the proposed forward model introduces a number of free parameters (Tables 1,2 and 3) and with the exception of θ all are assumed constant throughout a patients data set. With a complete set of estimated free parameters including $\theta(t)$ the forward model as a whole is compared to the data. The total sum squared error between the predicted spectrogram and the observed spectrogram is assumed to determine the joint probability of that set of free parameter values [5]. In addition to the stated domain over which each free parameter will be optimized, multiple ad hoc estimates and refinements are made, graphically implied with curved green lines radiating from "Data: Observed Spectrogram" in the flowchart Figure 1. For example the acoustic reflectivity of blood (B_b) is stated to be optimized between $-\infty$ and ∞ because each successive value comes from a linear estimate. In fact B_b is refined twice per iteration of the loop in 1, first set equal to values given by linear estimation depending on a subset of the forward model and secondly with the whole set of free parameter trial values. The most effective ad hoc optimization strategy stems from the observation that the value of $\theta(t)$ given by the RBE is quite stable or consistent for every free parameter except heart rate (ω). To exploit this stability many iterations of the loop in 1 are performed in parallel all sharing a compromise

---

[5] The reader may object that the variance of the noise itself should be a free parameter subject to optimization, and while this would not directly affect the optimum set of free parameters found at this step it's value is implicit in $\theta(t)$.

ω and $\theta(t)$. [6] Successful optimization to a global, or even local, best set of free parameters is the subject of future work. Our current optimization simply searches subsets of free parameters iterating a fixed number of times and returns the best candidate values.

Armed with estimates of the dynamic parameters, one can generate a variety of useful quantities, such as a spectrogram, an envelope, mean flow or pulsatility index. An example of a predicted spectrogram is shown in Figure 9, where it is compared with the corresponding observed spectrogram. The fitted spectrogram closely matches the observed spectrogram in multiple ways. For example: the gross features such at systolic and diastolic velocities are similar, the overall brightness matches and both have a subtle dicrotic notch. Also at the time of systole both the data and the predicted have a slightly less bright spectrogram for velocities less than FV_{max} as compared to times of diastole. A pulsatility index can be constructed as follows: The
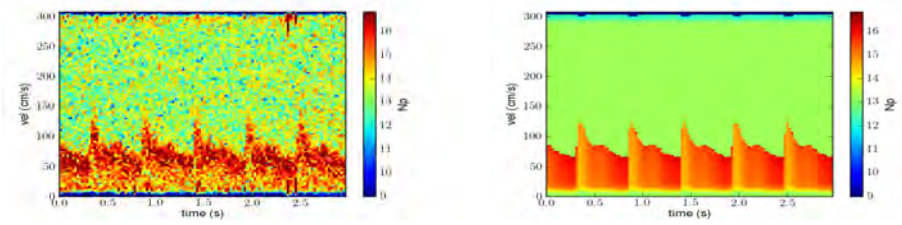

Figure 9: An example of an observed (left) and a predicted (right) spectrogram.

pulsatility is defined [6] over a cardiac cycle as the difference between the systolic and diastolic flow velocity, divided by the mean flow velocity, where systolic and diastolic are synonymous with the maximum and minimum of flow velocity. As any set of fixed parameters defines a cardiac cycle, they also define a pulsatility index. Similarly, any physical quantity that can be calculated from the forward model is thereby given by the fixed parameters.

---

[6]For initial iterations of the outer loop in Figure 1 the Windkessel model is used with fast approximations to the flow field and spectrogram calculations in order to perform parallel iterations on a single processor. A second round of iterations employ the full forward model with the flow field and spectrogram calculations but rather than repeatedly use the RBE a single ω and θ time series is shared for many iterations. Though it would be relatively easy to achieve we have yet to take advantage of hardware parallelization, because other algorithmic improvements are expected to yield dramatic speed gains.

4 Results

In order to assess the success of the above methodology it is applied to all of the data sets. First, the goodness of fit is assessed quantitatively by comparison to a null methodology. Second, the output is judged qualitatively, through a visual comparison of the predicted to the observed spectrogram.

Though there are notable examples of simulated spectrograms [19] and [4] there seem to be no instances of simulated spectrograms fit to data. There are, however, well established algorithms to draw the maximum flow velocity time series from an observed spectrogram. Any FV_{max} fitting algorithm may be considered to produce a fitted spectrogram with the following simple heuristic. Any given time series FV_{max} segregates the observed spectrogram into pixels which are due to blood flow ($FV < FV_{max}$) and pixels which are not ($FV > FV_{max}$). All pixels due to blood flow are assumed to have values drawn from a normal distribution with a mean value of $null_{signal}$. Similarly the values of the pixels not due to blood flow are assumed to be drawn from a normal distribution with the mean value $null_{clutter}$. The modified geometric method [11] is long established, and is currently in use in the Spencer device. In the null method the modified geometric method provides FV_{max} and the sample mean of the pixels above FV_{max} are taken as an estimate of $null_{clutter}$ and the sample mean of the pixels below, an estimate of $null_{signal}$ An example of this null methodology spectrogram is shown in Figure 10. The pixel by
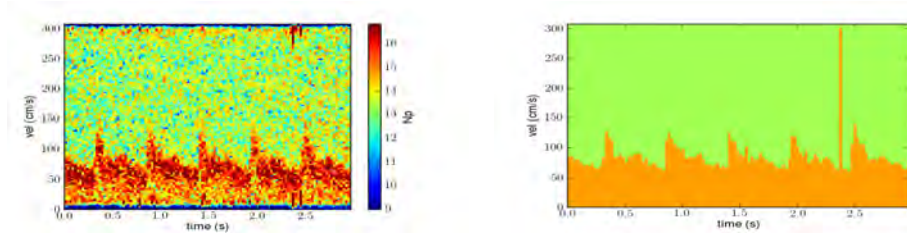

Figure 10: An example of a spectrogram predicted with the null methodology(right) along with the observed spectrogram (left)

pixel Pearson's correlation between predicted and observed spectrogram is calculated for each patient. This is done both for spectrograms predicted by the methodology of this paper and also for spectrograms predicted by the null method. Using the correlation between predicted and observed, as a simple performance measure, we compare the proposed methodology to

16

the null method in Figure 11. This within-data set correlation shows clearly
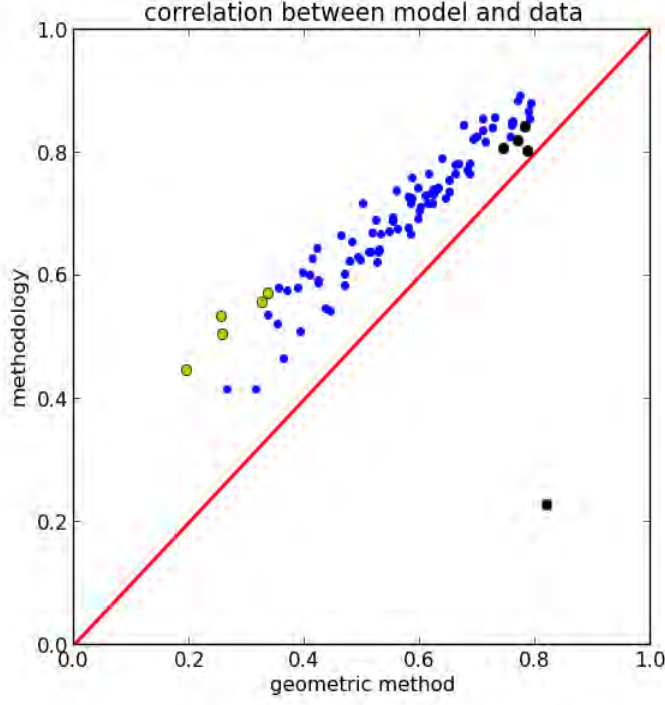

Figure 11: Each dot represents one data set. The correlation between the observed data set and the spectrogram predicted by the methodology of this paper is the vertical coordinate. The horizontal coordinate is the correlation between the observed data the null methodology

that the proposed methodology more closely fits the data, but to asses the goodness of fit we need to account for the number of free parameters in the null versus the proposed methodologies.

The Akaie information criterion (AIC) is a commonly used measure of goodness of fit, [12] intended to rank the generalizabiliy and performance of statistical models.

$$AIC = 2N_{params} - 2\ln\left(P\left(data|params\right)\right) \tag{7}$$

Where the number of free parameters, N_{params}, and the likelihood of observing the data given the optimized parameter values, $P\left(data|params\right)$ give a metric which is predictive of a model's cross validation performance. The

17

smaller a model's AIC the better. The null method gives an independent value of FV_{max} for every time step in the data, giving 120 free parameters. It also assigns a mean spectrogram value for pixels above and below FV_{max}, giving two more free parameters. The proposed methodology assigns a different phase in the cardiac cycle for each time step in the data, giving 120 free parameters. The Windkessel model introduces ten more parameters, the flow field calculation nine and the spectrogram calculation eight. So for the record length considered the proposed methodology has a total of 147 free parameters per data set and the null method 122. It is clear from figures
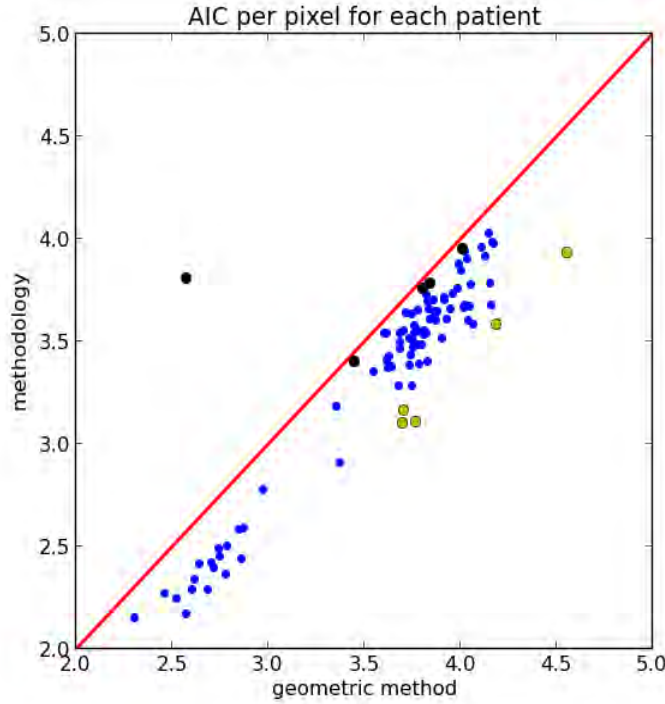
Figure 12: Each dot shows the AIC for a patients data set, the null method horizontally and proposed method vertically. With one exception every dot is below the diagonal indicating the proposed methodology is better. The data set corresponding to the lone point above the diagonal appears to consist solely of static and one "blip".

11 and 12 that the proposed methodology improves upon the null method. However the null method is a minimal standard. The true significance of this work is better demonstrated via a qualitative result.

18

A ready application of the methodology is in blind signal processing of observed spectrograms. Since there is no ground truth reference signal the reader may compare the original observed spectrogram in the left column of figures 13, 14, 15 and 16 to the predicted on the right, and judge subjectively how well the signal in the data is captured by the predicted spectrogram. To convey some of the variety present in the 96 data sets present the five worst and the five best are shown. The terms "best" and "worst" are defined by the relative performance measure difference between the null and the proposed methods. This is done for both performance measures leading to ten data sets for consideration. Notice that these "worst" and "best" data sets are highlighted in black and yellow respectively in figures 11 and 12

5 Summary and Discussion

A methodology has been proposed, modeling blood flow through an artery and the measurement of it with ultrasound. The approach involves a combination of physiologically-based and statistical models. For a given patient, each component of the overall model involves parameters that are estimated from observed spectrograms. The resulting models may then be used to produce a variety of useful quantities, including the spectrogram, the envelope, and the flow field.

A fundamental signal processing limitation in use of TDU leads to aliasing, namely spurious features at the top of the spectrogram which appear to reflect the true signal of interest at the bottom of the spectrogram. Another artifact that signal processing is designed to minimize is the true acoustic signal due to reflections from the vessel wall, which tends to be brighter than the signal from blood flow. Because aliasing and the acoustic signal from the vessel wall are explicitly included in the forward model they are trivially easy to remove from the predicted spectrogram. Figure 17 shows an illustration of this utility. The bottom left figure qualitatively resembles the true spectrogram (top); the bottom right figure shows the spectrogram with the aliasing and vessel wall reflection removed.

Another novel feature of the work here is the articulation of a closed-form relationship between a general two or three dimensional flow field and a spectrogram, namely Equation 3. This expression allows one to compute a spectrogram from **any** flow field, regardless of how it is generated. The ability to relate the flow field to a spectrogram is important for any attempt
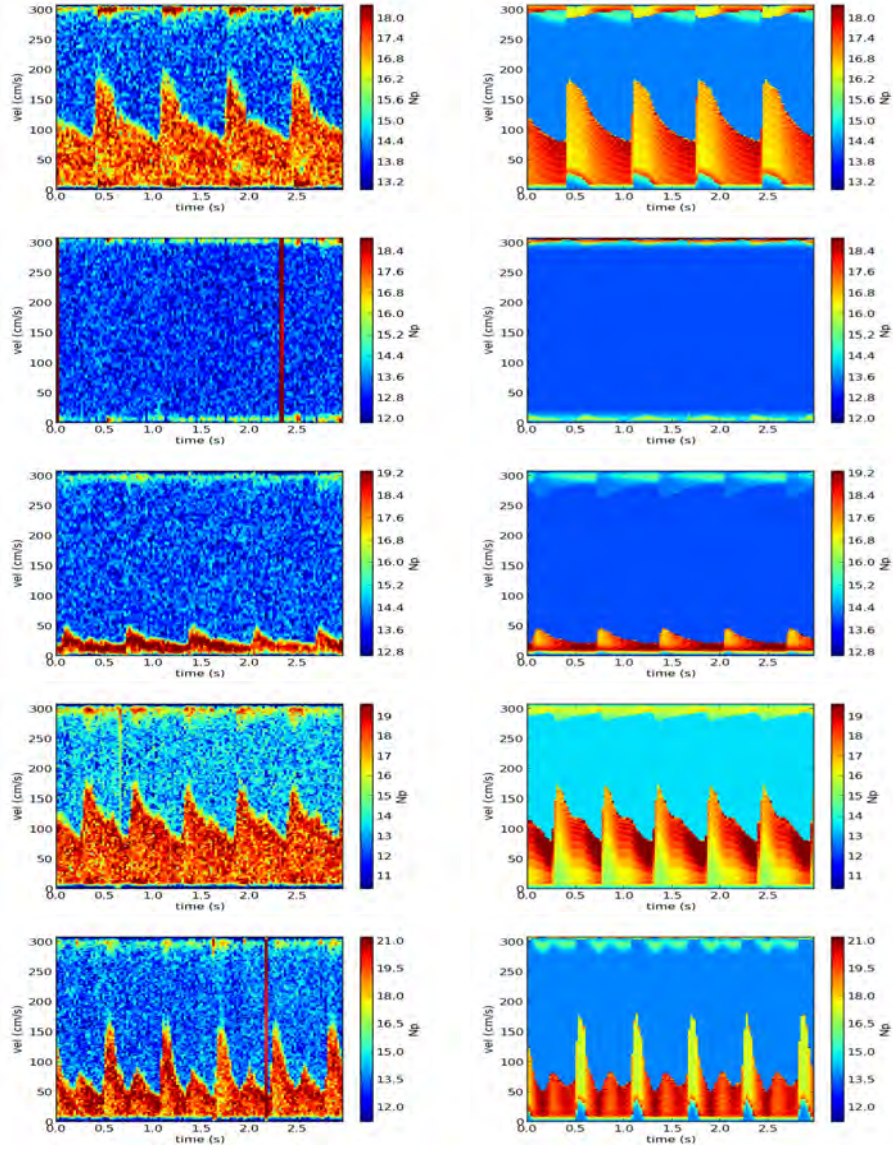
Figure 13: Observed spectrogram (left) and predicted spectrogram (right) of the five patients for which the proposed methodology is "worst". In this case we mean worst in the sense that difference between the pixel by pixel correlation of the methodology minus the null method is minimal.
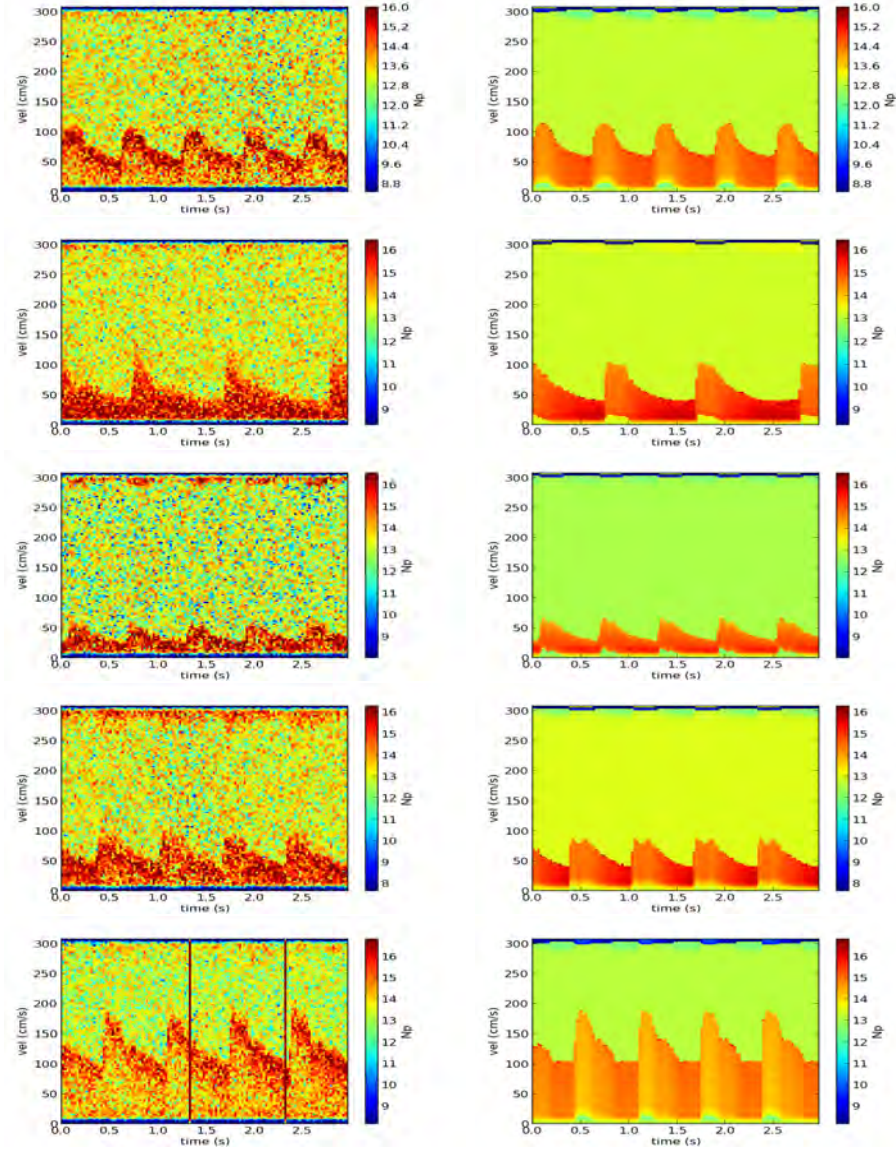
20

Figure 14: Observed spectrogram (left) and predicted spectrogram (right) of the five patients for which the proposed methodology does "best". Where we mean best in the sense that the correlation of the proposed methodology minus correlation of the null method is maximal.
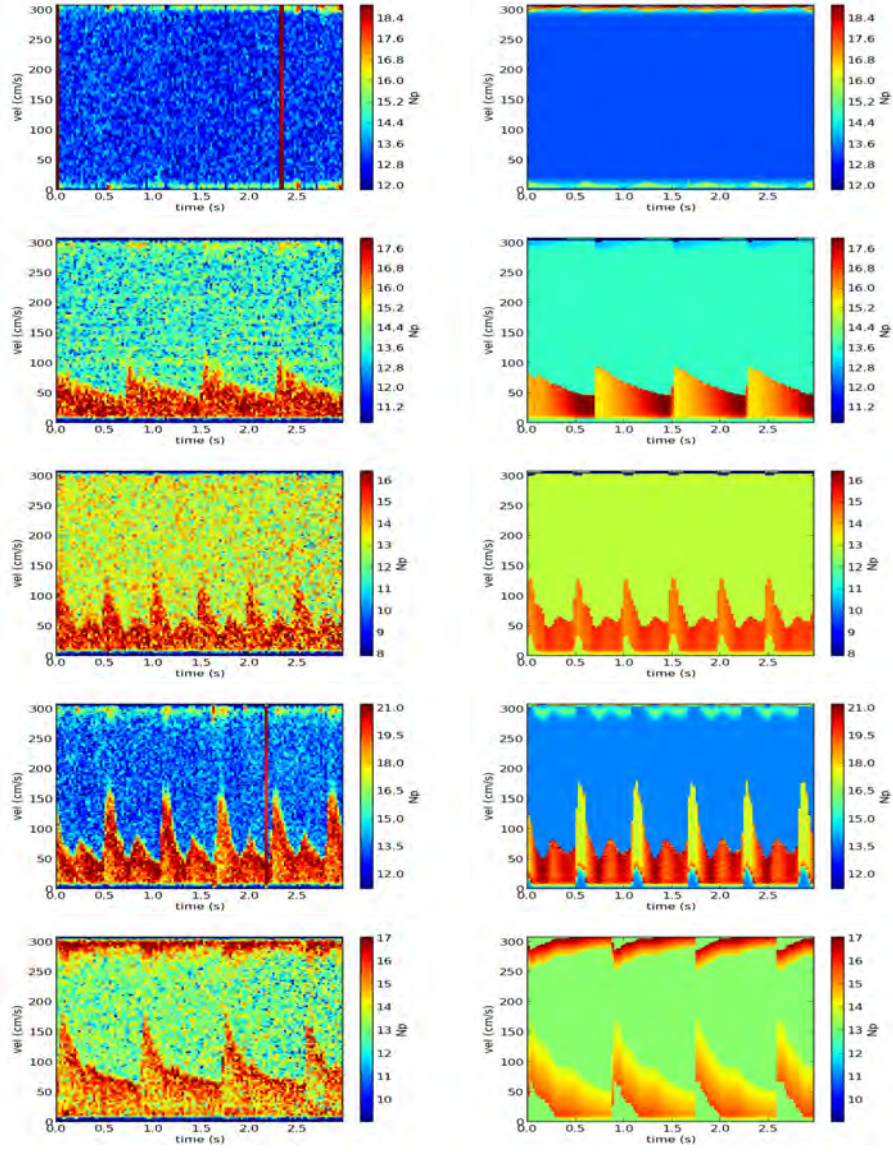
Figure 15: Observed spectrogram (left) and predicted spectrogram (right) of the five patients for which the proposed methodology is "worst". In this case we mean worst in the sense that difference between the Akaike information criterion of the methodology minus the null method is maximal.
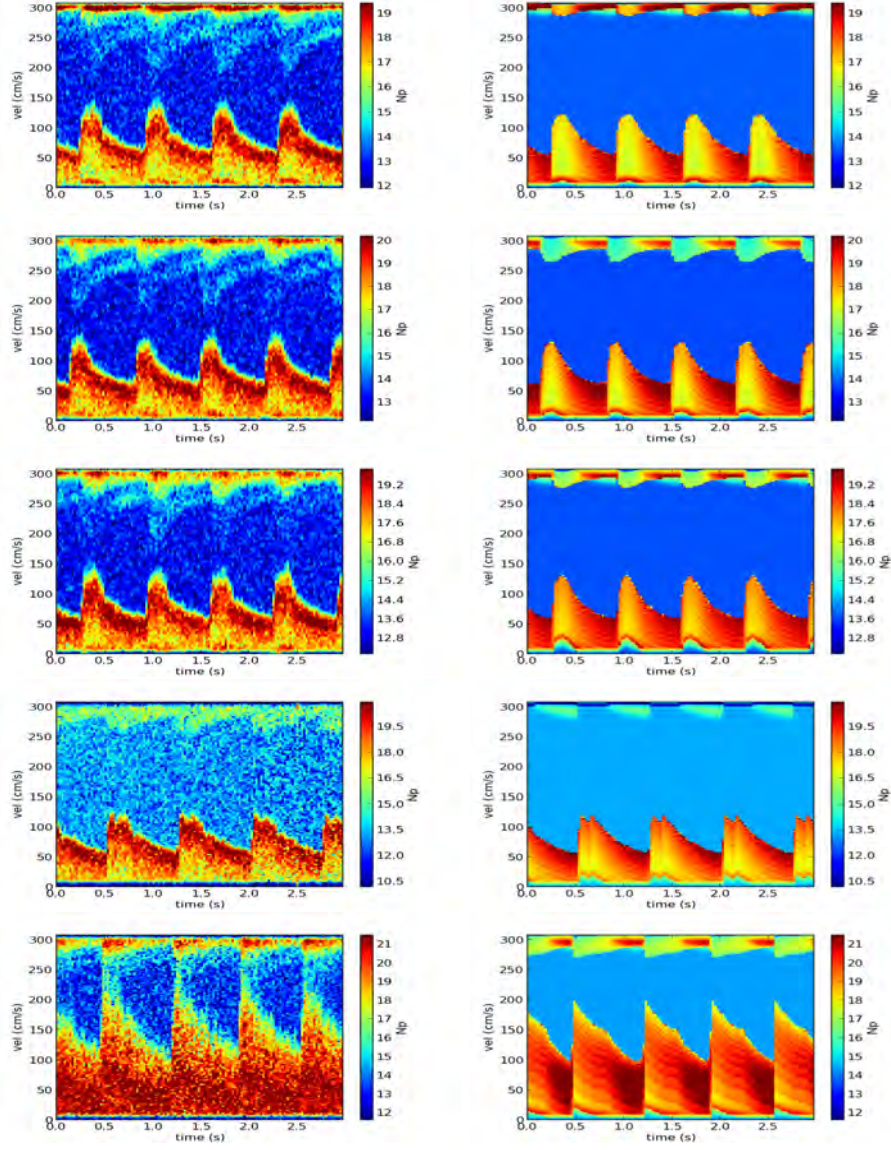
Figure 16: Observed spectrogram (left) and predicted spectrogram (right) of the five patients for which the proposed methodology does "best". Where we mean best in the sense that the AIC of the proposed methodology minus AIC of the null method is minimal.
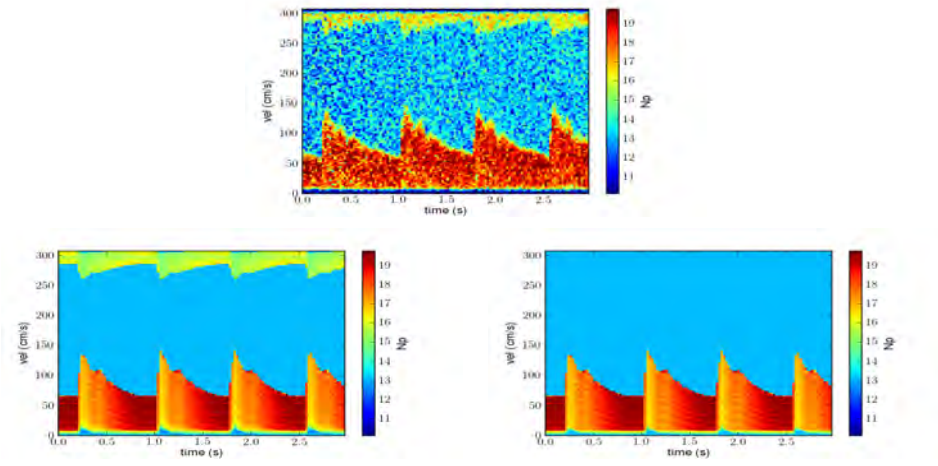
Figure 17: From an observed spectrogram (top) the methodology returns a forward model designed to best the data (bottom left). Simply omitting the contributions to the predicted spectrogram from aliasing and tissue motion (bottom right) amounts to signal processing the data so as to remove these artifacts.

at modeling of blood flow, because models generally produce flow fields, but TDU observations are generally not of the flow field but of the spectrogram. Expression 3, therefore, allows one to verify or validate models of blood flow. For instance, closed-form solutions to pulsatile fluid flow in an elastic tube date from the 1950's in [2] and [1]. But, more recent work by Myers[3] develops analytic solutions for a curved artery. As such, one could test Myers' model by simply replacing the component for flow-field calculation with Myers' solutions.

Another exercise made available by the proposed methodology is as follows: All of the data sets are anonymized but it appears that a few are drawn from repeated patients; that they are drawn from a single subject differing in only adjustment of the TDU device. An estimate of $\theta(t)$ and the free parameters of the spectrogram calculation are made as usual but in a slight change to the methodology free parameters for the Windkessel model and the flow field calculation are shared between the two data sets. In other words the free parameters representing the physiology of the patient are constant across the two data sets and optimized for the data sets jointly while the free parameters representing the TDU and the time of their cardiac cycles are separate and optimized for each data set independently. The resulting predicted spectrograms are shown in the middle row of Figure 18, and the

corresponding observed spectrograms shown in the top row. Also, as long as we have a forward model representative of a patients physiology we may do away with the free parameters of the spectrogram calculation entirely and replace them with idealized values. In this application the flow velocity field could be thought of as the more fundamental quantity and the simulated spectrogram as merely a flow visualization graphic. This is shown in the bottom row of Figure 18 Beyond the predicted spectrograms we can report
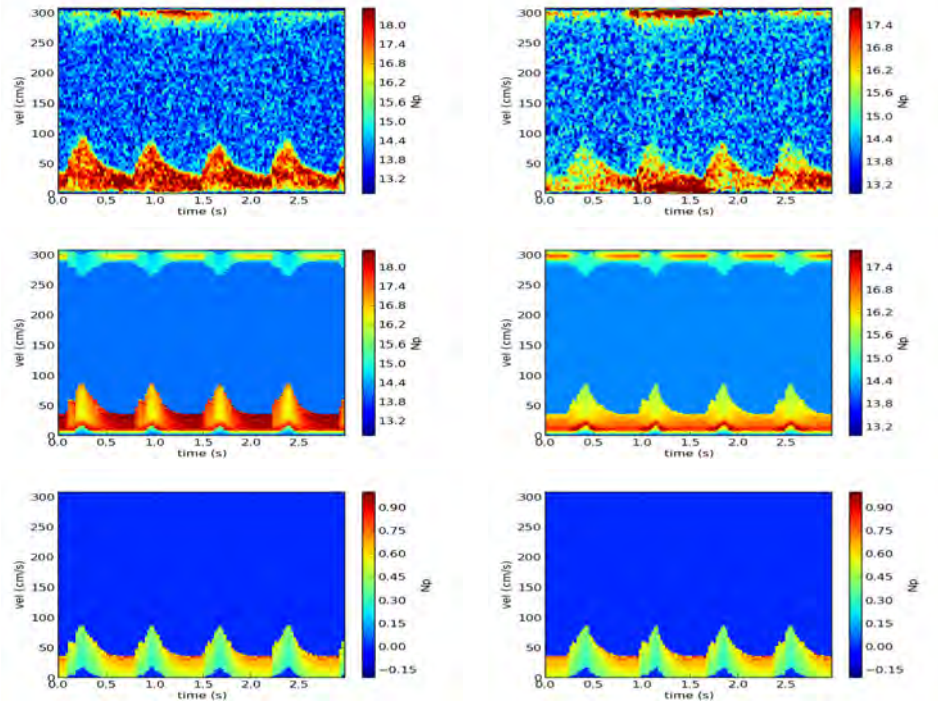

Figure 18: Two data sets presumed to originate from the same patient are shown at the top. Shown in the middle are the predicted spectrogram's with shared Windkessel models and flow field calculations. In the bottom row the forward models are identical to those shown in the middle row, with the exception that the spectrogram calculation free parameters values are replaced with idealized values.

(Table 4) the optimized values of the free parameters of the spectrogram calculation corresponding to Figure 18. With the caveat that we do not expect to have found a global optimum for these free parameters, we can say that out of all the sets of trial parameter values these are the most likely. Without a methodology like the one of this paper no such an analysis would be possible.

parameter	left	right	idealized
focus offset x	0.003565 cm	0.003163 cm	0.0
focus offset y	0.001167 cm	0.002609 cm	0.0
focus width	0.003518 cm	0.002170 cm	a_0
off-bore	0.125520 rad	0.342641 rad	0.0
aliasing integer	2,	2,	N/A
wall spread	6.904307 cm/s	7.930820 cm/s	7.21875 cm/s

Table 4

The motivation for this work is that the optimized values of the free parameters will be found useful, but optimization and attainment of their most likely values remains an aim for future work. Fixed parameter values which could reliably be fit to data would have novel applications. For example, although not explicitly clear, the methodology developed here leads to a model of autoregulation, the response of smooth muscle to the CO_2 concentration in blood [25]. In current clinical practice the visual assesment of a spectrogram is an important tool for assessing autoregulation. In the proposed forward model, the Young's modulus, Poisson's ratio, and the rest diameter for the middle cerebral artery, are all parameters describing the properties and state of the smooth muscle. With estimates of these parameters, the resulting model is implicitly a model of autoregulation.

References

[1] J.R. Womersley, Oscillatory motion of a viscous liquid in a thin walled elastic tube. I. The linear approximation for long waves, Philosophical Magazine, 1955b, 46:199-221

[2] G.W. Morgan, J.P. Kiely, Wave Propagation in a viscous liquid contained in a flexible tube, The Journal of the Acoustical Society of America, 1954, 26(3):323-328

[3] Lance Jonathan Myers and Wayne Logan Capper, Analytical Solution for Pulsatile Axial Flow Velocity Waveforms in Curved Elastic Tubes, IEEE TRANSACTIONS ON BIOMEDICAL ENGINEERING, VOL. 48, NO. 8, AUGUST 2001, 864-873

[4] David H. Evans, Some Aspects of the relationship Between Instantaneous Volumetric Blood Flow and Continuous Wave Doppler Ultrasound Recordings - I, Ultrasound in Medicine and Biology , volume 8 number 6, first received 17 July 1980,final form 24 March 1982, 605-609

[5] M G Taylor, An experimental determination of the propagation of fluid oscillations in a tube with visco-elastic wall, Phys. Med Biol., 4, 63, 1959, 63

[6] R.G. Gosling, D.H. King, Arterial assessment by Doppler shift ultrasound, Proc R Soc Med, 67 (1974), 447-449

[7] Ochi H, Matsubara K, Kusanagi Y, Taniguchi H, Ito M, Significance of a diastolic notch in the uterine artery flow velocity waveform induced by uterine embolisation in the pregnant ewe, Br[itish] J[ournal] Obstet Gynaecol, 1998 Oct, 105(10):1118-21

[8] J.C. Mirsa, G.C. Shit, Blood flow throught arteries in a pathological state: A theoretical study, International journal of Engineering Science, December 13, 2005, 662-671

[9] V.L. Babikian, L.R. Wechsler, Transcranial Doppler Ultrasonography, Second Edition. Butterworth Heinemann, Boston, 1999

[10] Garcia D, Del Alamo JC, Tanne D, Yotti R, Cortina C, Bertrand E, Antoranz JC, Perez-David E, Rieu R, Fernandez-Aviles F, Bermejo J, Two-dimensional intraventricular flow mapping by digital processing conventional color-Doppler echocardiography images, IEEE Trans Med Imaging, 2010 Oct, 29(10):1701-13

[11] Fernando KL, Mathews VJ, Clark EB, A mathematical basis for the application of the modified geometric method for maximum frequency estimation, IEEE Trans. Biomedical Engineering, 2004, 51:2085-2088

[12] Stone M, An Asymptotic Equivalence of Choice of Model by Cross-Validation and Akaike's Criterion, Journal of the Royal Statistical Society: Series B (Methodological), (1977), 39 (1): 4447

[13] Caren Marzban, Ph.D., Paul R. Illian, B.S. David Morison, B.S., Pierre D. Mourad, Ph.D., A Double-Gaussian, Percentile-based Method for

Estimating Maximum Blood Flow Velocity, Journal of Ultrasound in Medicine, 2013 Nov, 32(11):1913-20

[14] Bernhard Schmidt, Marek Czosnyka, Andreas Raabe, Hilal Yahya, Jens Jurgen Schwarze,Dieter Sackerer, Dirk Sander and Jurgen Klingelhofer, Adaptive Noninvasive Assessment of Intracranial Pressure and Cerebral Autoregulation, Stroke, published online December 12, 2002, 84-89

[15] Ursino M, A simple mathematical model of the interaction between intracranial pressure and cerebral hemodynamics, J Appl Physiol (1985), 1997 Apr, 82(4):1256-69

[16] Kashif FM, Verghese GC, Novak V, Czosnyka M, Heldt T, Model-based noninvasive estimation of intracranial pressure from cerebral blood flow velocity and arterial pressure, Sci Transl Med, 2012 Apr 11, 4(129):129ra44

[17] M. Sanjeev Arulampalam, Simon Maskell, Neil Gordon, A tutorial on particle filters for online nonlinear/non-Gaussian Bayesian tracking, IEEE Transactions on Signal Processing, 2002, 174-188

[18] Lawrence D. Stone, Thomas L. Corwin, James B. Hofmann, Technical Documentation of Nodestar, Metron, Inc., Advanced Information Technology Branch, Information Technology Division, Reston, VA, December 11, 1995

[19] Rune Aaslid commercial software avalible from http://www.transcranial.com/

[20] Sunghan Kim, Mateo Aboy, James McNames, Pulse pressure variation tracking using sequential Monte Carlo methods, Biomedical Signal Processing and Control, 8 (2013), 333-340

[21] Esther-S. Platzer, Frank Deinzer, Dietrich Paulus, Joachim Denzler, 3-d Blood Flow Reconstruction from 2-d Angiograms, Bildverarbeitung fur die Medizin, 2008, 288-292

[22] Taous-Meriem Laleg, Emmanuelle Crepeau, Michel Sorine, Separation of arterial pressure into a nonlinear superposition of solitary waves and a windkessel flow, Biomedical Signal Processing and Control, Volume 2, Issue 3, July 2007, 163-170

[23] Pijush K. Kundu, Ira M. Cohen, Fluid Mechanics fourth edition, Academic Press, Waltham, Massachusetts, 2008

[24] Jorgen Arendt Jensen, Estimation of Blood Velocities Using Ultrasound: A Signal Processing Approach, Cambridge University Press, Cambridge England, published March 29, 1996

[25] R Aaslid, K F Lindegaard, W Sorteberg and H Nornes, Cerebral autoregulation dynamics in humans, Stroke, 1989, 20:45-52

[26] Peter Guttorp, Vladimir N. Minin, Stochastic Modeling of Scientific Data, CRC Press, Boca Raton, FL, United States, Aug 1, 1995

[27] Jonathan Black, Garth Hastings Handbook of Biomaterial Properties Springer Feb 28, 1998

[28] Song Shou Mao, MD, Nasir Ahmadi, MPH, Birju Shah, M.B.B.S, Daniel Beckmann, BS, Annie Chen, BS, Luan Ngo, BS, Ferdinand R Flores, BS, Yan lin Gao, MD, and Matthew J Budoff, M.D. Normal Thoracic Aorta Diameter on Cardiac Computed Tomography in Healthy Asymptomatic Adult; Impact of Age and Gender

[29] Thomas Sandgren, MD, Bjrn Sonesson, MD, PhD, sa Rydn Ahlgren, MD, Toste Lnne, MD, PhD The diameter of the common femoral artery in healthy human: Influence of sex, age, and body size

[30] Jaroslaw Krejza, MD, PhD; Michal Arkuszewski, MD; Scott E. Kasner, MD, PhD; John Weigele, MD, PhD; Andrzej Ustymowicz, MD, PhD; Robert W. Hurst, MD, PhD; Brett L. Cucchiara, MD; Steven R. Messe, MD Carotid Artery Diameter in Men and Women and the Relation to Body and Neck Size

[31] Jain, K.K. Some observations on the anatomy of the middle cerebral artery Canad. J. Surg. 7(2):134-139. 1964

[32] G D Lowe, F G Fowkes, J Dawes, P T Donnan, S E Lennie and E Housley Blood viscosity, fibrinogen, and activation of coagulation and leukocytes in peripheral arterial disease and the normal population in the Edinburgh Artery Study. Circulation 1993 87:1915-1920

[33] Bergel, D.H. The elastic properties of the arterial wall J. Physiol London 1961

[34] Funk and Wagnalls Encyclopedia Blood 1985

[35] Paulson OB1, Strandgaard S, Edvinsson L. Cerebral autoregulation. Cerebrovasc Brain Metab Rev Summer;2(2):161-92. 1990

Mixture Models for Estimating Maximum Blood Flow Velocity

Caren Marzban, PhD, Wenxiao Gu, MS, Pierre D. Mourad, PhD

Objectives—A gaussian mixture model (GMM) was recently developed for estimating the probability density function of blood flow velocity measured with transcranial Doppler ultrasound data. In turn, the quantiles of the probability density function allow one to construct estimators of the "maximum" blood flow velocity. However, GMMs assume gaussianity, a feature that is not omnipresent in observed data. The objective of this work was to develop mixture models that do not invoke the gaussian assumption.

Methods—Here, GMMs were extended to a skewed GMM and a nongaussian kernel mixture model. All models were developed on data from 59 patients with closed head injuries from multiple hospitals in the United States, with ages ranging from 13 to 81 years and Glasgow Coma Scale scores ranging from 3 to 11. The models were assessed in terms of the log likelihood (a goodness-of-fit measure) and via visual comparison with the underlying spectrograms.

Results—Among the models examined, the skewed GMM showed a significantly ($P < .05$) higher log likelihood for 56 of the 59 patients and produced maximum flow velocity estimates consistent with the observed spectrograms for all patients. Kernel mixture models are generally less "robust" in that their quality is inconsistent across patients.

Conclusions—Among the models examined, it was found that the skewed GMM provided a better model of the data both in terms of the quality of the fit and in terms of visual comparison of the underlying spectrogram and the estimated maximum blood flow velocity. Nongaussian mixture models have potential for even higher-quality assessment of blood flow, but further development is called for.

Key Words—blood flow; brain; head injury; noninvasive; transcranial Doppler ultrasound

The importance of estimating blood flow in major cerebral arteries has been well documented.[1–5] The reduction of blood flow through a major cerebral artery, such as caused by cerebral vasospasm, can lead to a wide range of disorders; therefore, monitoring blood flow has important clinical consequences.[6] Transcranial Doppler ultrasound imaging is one of the methods for assaying blood flow.[7,8] Vasospasm leads to reduced blood flow but an increased blood flow velocity; therefore, estimating the maximum blood flow velocity is of particular importance.[9]

The time series of a flow velocity histogram is called a spectrogram, and the time series of the maximum flow velocity is called an envelope. Despite their clinical importance, neither the spectrogram nor the maximum flow velocity can be observed directly. From a statistical perspective, they must be considered population parameters

that are to be estimated from data. Moreover, the very notion of maximum flow velocity is ambiguous because theoretically flow velocity has no upper bound. Many envelope estimation algorithms have been proposed[10–15]; one that is frequently[16] used is the modified geometric method (MGM).[10] That method essentially searches for a "kink" in the cumulative histogram of flow velocity and defines the maximum flow velocity as the flow velocity at which the kink occurs. It provides reliable envelope estimates but lacks the important feature of allowing one to quantify the uncertainty in maximum flow velocity. By contrast, the mixture model described by Marzban et al[15] allows one to quantify flow velocity in terms of percentiles. For example, one may examine the envelope corresponding to the 90th, 95th, and 99th percentiles of flow velocity. Each of these provides a unique and well-defined measure of "maximum" flow velocity, and the ability to do this is the main advantage of mixture models. Furthermore, the maximum flow velocity as defined by the MGM is in close agreement with that produced by the 90th percentile envelope in a mixture model.[15] As such, mixture models enjoy two important features: (1) they produce envelopes corresponding to multiple percentiles of flow velocity; and (2) one of the percentiles (ie, the 90th) produces an envelope that is approximately equal to the envelope estimated by the MGM.

However, the specific type of mixture model developed by Marzban et al[15] assumes that the distribution of flow velocity, at any point in time, as measured by a transcranial ultrasound device, is gaussian. The agreement between an envelope produced by such a gaussian mixture model (GMM) and that produced by the MGM suggests that either the distribution of flow velocity truly is gaussian, or that the envelope is not sensitive to violations of that assumption. As shown below, the distribution of flow velocity varies with time; at certain times, it is gaussian (or at least, near gaussian), while at other times it is not. The deviations from normality manifest themselves mostly as a skew. For this reason, one of the models described here assumes that the underlying distributions of flow velocity are skewed gaussian. Data are used to estimate the mean, the variance, and the shape (or skew) parameter of the distributions. Here, this model is referred to as a skewed GMM.[17–19] Another model discussed (briefly) does not assume a parametric form for the distribution of flow velocity at all; instead, the distribution is inferred by using kernel estimates.[20–24] Such kernel mixture models (KMMs) are flexible in that they accommodate a wide range of distributions (including gaussian). However, kernel methods involve a smoothing parameter whose value is a priori unknown. Generally, extreme values of the parameter correspond to

either a smooth distribution (eg, gaussian) or a highly irregular distribution. One often uses some criterion (such as the maximization of likelihood) to optimize the smoothing parameter.

In this study, the skewed GMM and KMM were developed for estimating the envelope for each of 59 patients in our data set. Although quantitative measures for goodness of fit were used to compare the various models, qualitative comparisons were also used. This practice is necessary because, as the true envelope is not directly observable, the estimated envelope is assessed by visually comparing it with the underlying spectrogram.

Materials and Methods

Data
The data for this work were collected from a preclinical study involving 59 patients with closed head injuries from multiple hospitals in the United States, with ages ranging from 13 to 81 years and Glasgow Coma Scale scores ranging from 3 to 11. A PowerMode 100 transcranial Doppler device (Spencer Technologies, Northborough, MA) was used at the Harborview Medical Center (Seattle, WA), Columbia University Medical College (New York, NY), and the University of Texas Medical School (Houston, TX). The device has an ultrasound carrier frequency that ranges between 1.75 and 2 MHz and pulse repetition frequencies of 8000 to 10,000 Hz. The transcranial Doppler probe was placed on the temple of the patient by the sonographer after application of ultrasound gel. In all cases, the sonographer sought to produce an optimal spectrographic signal, defined here as one with a maximum systolic flow velocity in the main branch of the middle cerebral artery. To do so, the sonographer manipulated the angle of insonation of the middle cerebral artery by the probe, the power of the ultrasound, as well as the depth within the brain from which the Doppler spectral data were obtained. Further details on this data set can be found in previous studies by Marzban et al.[15,25] The former used only the ultrasound-derived transcranial Doppler spectra for the purpose of developing the aforementioned GMMs for envelope estimation. In the latter, the data were used to develop a model of arterial blood pressure, which can in turn be used to predict intracranial pressure. In accordance with the Institutional Review Board for each hospital, informed consent was obtained from all patients or their families.

With clinically approved transcranial Doppler units, blood flow velocity in the middle cerebral artery was measured with Doppler ultrasound. Data were collected for periods from 5 to 30 minutes. All retrospective data pro-

cessing and analysis were conducted at the Applied Physics Laboratory of the University of Washington. Although the Doppler spectral time series were initially sampled at 125 Hz, they were down-sampled at 40 Hz. This resolution was sufficient to resolve each patient's systolic rise, diachrotic notch, and diastolic minimum. For each patient, envelopes were produced over a fixed duration (118 sampled points, or about 3 minutes). This duration is sufficiently long to include several cardiac cycles while allowing details of the envelopes to be visually evident.

Data Processing and Statistical Analysis

In previous work, it was shown that the GMM is a natural extension of the MGM in that the former provides for multiple estimators of maximum flow velocity based on percentiles of the probability density function of the flow velocity. It was found that the envelope corresponding to the 90th percentile of the probability density function is comparable with the envelope estimated by the MGM.[15] As such, the GMM is superior (to the MGM) in that it allows one to estimate the highest blood velocities, and effectively their uncertainty, through multiple percentiles of the probability density function of flow velocity. The MGM is included in the analysis here only for the purpose of providing a comparison with the GMM. In fact, since the GMM outperforms the MGM, the skewed GMM and KMM were both compared with the GMM. The KMM leads to envelopes that are moderately superior to those based on the skewed GMM but not for all patients; for this reason, the KMM is discussed only briefly and only for the purpose of discussing future work.

As explained in Appendix 1, in a GMM, the distribution (more accurately, the probability density function) of flow velocity for each patient and at any time is assumed to be a linear combination of two gaussians. The coefficients, called mixing coefficients, as well as the parameters of the gaussians are estimated from data. In the study by Marzban et al,[15] it was shown that the two gaussians represent the "signal" and the "background" portions of the distribution, respectively. Those, then, allow one to use the upper percentiles of the former to quantify the maximum flow velocity. The left panel of Figure 1 shows an instance of the signal gaussian (blue), the background gaussian (red), the 90th, 95th, and 99th percentiles of the former (blue vertical lines), and the maximum flow velocity according to the MGM (black vertical line). The data (black circles) are from a single patient and at a given time.

The generalization from a GMM to a skewed GMM is relatively straightforward in that each gaussian in the mixture model is replaced by a skewed gaussian (Appendix 1). This process introduces only 1 more parameter: namely, the shape parameter, which affects the skew of the gaussian. The difference in the models may be visualized by the example in Figure 1. The middle panel of Figure 1 shows the various components. The data are for the same patient and same time as in the left panel. Note the evident skew in the signal and the background components. The skewed GMM algorithm is implemented by an R package called mixsmsn,[18,19] available online from the Comprehensive R Archive Network.[26]

In the KMM the distribution of flow velocity is assumed to be a linear combination of two distributions, but unlike the GMM and skewed GMM, each distribution is estimated by using kernel methods (Appendix 1). The kernel method followed here uses the expectation maximization algorithm for fitting multivariate nonparametric mixtures with com-

Figure 1. Distribution (more accurately, probability density function) for the signal (blue) and background (red), as determined by the GMM, skewed GMM, and KMM. The blue vertical lines denote the 90th, 95th, and 99th percentiles of the signal flow velocity (FV), and the black vertical line marks the maximum flow velocity according to the MGM.
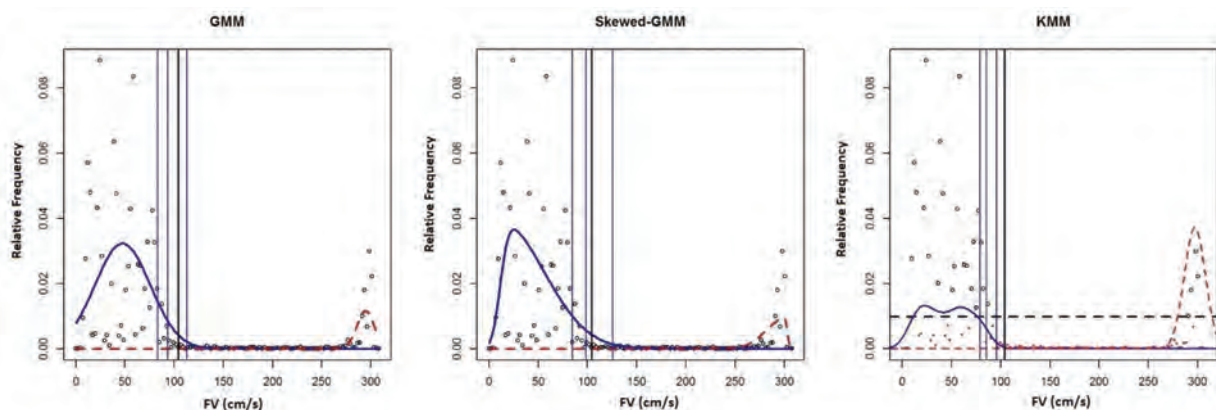
pletely unspecified component densities,[19–21] except for a conditional independence assumption described by Benaglia et al.[23] The kernel is the standard normal density function. The algorithm is implemented in an R package called mixtools,[23–25] available from the Comprehensive R Archive Network.

The right panel of Figure 1 shows the resulting distributions. Note that the distributions are now more irregular, capturing the nonsmooth structure evident in the data (black circles). Appendix 1 explains the manner in which the smoothing parameter is set.

Results

As mentioned previously, the comparison of the various models examined here has both a quantitative component as well as a qualitative (visual) component. The "visual envelope" suggested by a visual inspection of the spectrogram is contingent on the color coding underlying the spectrogram.[15] Given that the true envelope is unknown, the visual envelope can be considered yet another estimate, and despite its qualitative nature, the visual envelope provides a background against which all of the other estimates may be viewed. Then a model is declared as useful if the estimated envelope is visually consistent with the underlying spectrogram. Another qualitative criterion that is applied to assess the usefulness of the models is the consistency (in time) with which the estimated envelope agrees with the spectrogram. For example, if the estimated envelope has stand-alone peaks or troughs interspersed throughout the time window of the spectrogram, then the model is deemed not useful, or at least worthy of further research.

The spectrograms and envelopes for the GMM, skewed GMM, and KMM for a single patient are shown in Figure 2. (The corresponding patient is different than that for Figure 1; the reason why different patients were used for different figures was to illustrate different characteristics of the various methods.) For this particular patient, it can be seen that the 3 percentiles according to the GMM (left panel) are close to one another and generally lower than the envelope based on a visual inspection of the spectrogram. By contrast, the 3 envelopes based on the skewed GMM are more widely spread and more consistent with the spectrogram (middle panel). The KMM's envelopes (right panel) have similarities with and differences from the GMM and the skewed GMM. For example, they underestimate the flow velocities (as for the GMM) but are relatively spread out (as for the skewed GMM). These patterns are generally true across many patients. Also, note the complete disagreement between the spectrogram and the 99th percentile envelope at the time just before 20 (0.025 seconds). This type of failure is characteristic of the KMM, and it is discussed further in the "Discussion" section.

Another noteworthy feature in Figure 2 is that GMM envelopes are generally lower than the aforementioned visual envelope but only for relatively high flow velocity values. This characteristic is evident in the manner in which the envelope is "below" the highest flow velocities in the spectrogram but only when flow velocities are highest. The skewed GMM solves that problem. It is a consequence of the fact that low flow velocity values are consistent with gaussian distributions, but for high flow velocity values, the distributions are more skewed.

The time dependence of the shape of the distributions can be confirmed by examining the values of the shape parameter as a function of time. Figure 3 shows the time series for the estimated shape parameter for the signal (left panel) and background (right panel). It can be seen that for most of the time series, the values of the shape parameters are approximately 0; ie, the distribution of the flow

Figure 2. Spectrograms (color background) and 90th, 95th, and 99th percentile envelopes (black) according to the GMM, skewed GMM, and KMM for a single patient.
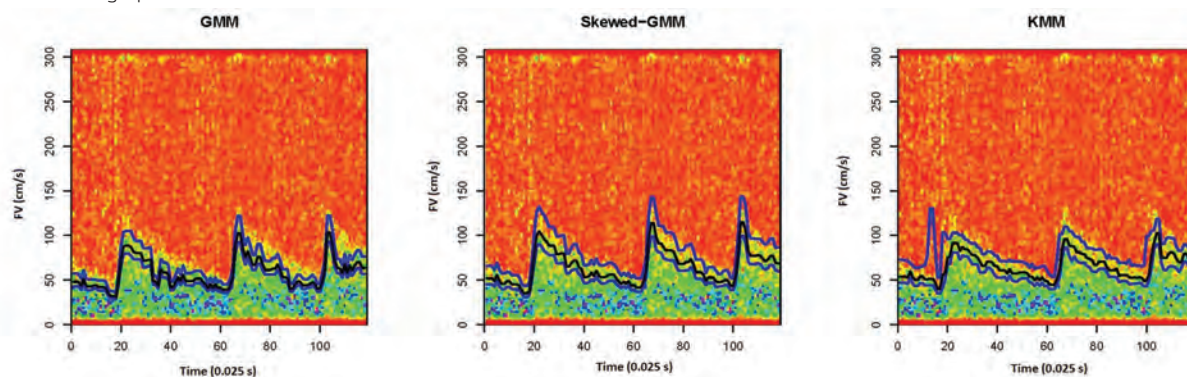
velocity is gaussian. However, there are also times at which the shape parameters are unambiguously not 0. The times correspond to regions of the spectrogram where flow velocities take their highest values. Note that when the shape parameters are not 0, they are positive for the signal and negative for the background components of the mixture model. (A positive shape parameter value corresponds to a right-skewed gaussian.)

As seen for the patient corresponding to Figure 3, the shape parameter is 0 for most times. However, that is not true for all patients; Figure 4 shows a histogram of the estimated shape parameters for a different patient. Note the bimodal structure; the left mode corresponds to the background, whereas the right mode is for the signal. It follows that the background component is consistently left skewed (with shape parameters in the –30 range), and the signal component is either gaussian (corresponding to the peak at 0) or right skewed (with shape parameters between 0 and +30).

Figures such as those in Figure 2 are useful for assessing the quality of an envelope. However, they were impractical for addressing the quality of the envelopes for all 59 patients. Consequently, although we performed this visual inspection for all patients, the results are not shown here. Instead, one can rely on the goodness-of-fit measure itself, not the envelope, to compare the various models developed here. There are numerous quantities that can be used for measuring how well a model fits the data. One commonly used measure is the log likelihood (LL). Given that the fitting of the model is performed at each time, there exists a time series for the LL as well (not shown). For the purpose

of comparing two models, however, it is sufficient to examine the difference between LL values of the models. Therefore, for each patient, the histogram, or box plot, of this quantity provides a visual assessment of the relative performance of the models. If two models are comparable in terms of goodness of fit, then the box plot will be centered on the number 0. Otherwise, the models can be deemed different. It is important to point out that the LL assesses the goodness of fit of the mixture model used for estimating an envelope, not the quality of the estimated envelope itself; an assessment of the quality of the estimated envelope would require the true envelope, which is unobservable. The reason for evaluating the models here in terms of LL and the quality of envelopes is to allow for the possibility that one model may outperform another model in terms of LL but not necessarily in terms of the quality of the envelope; or vice versa.

Figure 5 shows a box plot of LL (skewed GMM) minus LL (GMM) for all 59 patients. (Recall that the variability of these box plots is due to time.) The fact that most box plots are "above" the vertical line at 0 implies that for most of the patients, the LL of the skewed GMM is generally higher than that of the GMM across time. In other words, on average (across time), the skewed GMM is a better model of the data than the GMM. A few exceptions are patients 19, 41, and 53, for whom the box plots are mostly centered around 0, and as such, there is no significant difference between the GMM and skewed GMM. To assess whether the skewed GMM has higher LL values than the GMM, a 1-sided t test was performed. All of the P values were found to be less than .05, except those for patients 19,

Figure 3. Time series of the estimated shape parameter for the signal and background distribution for a single patient.
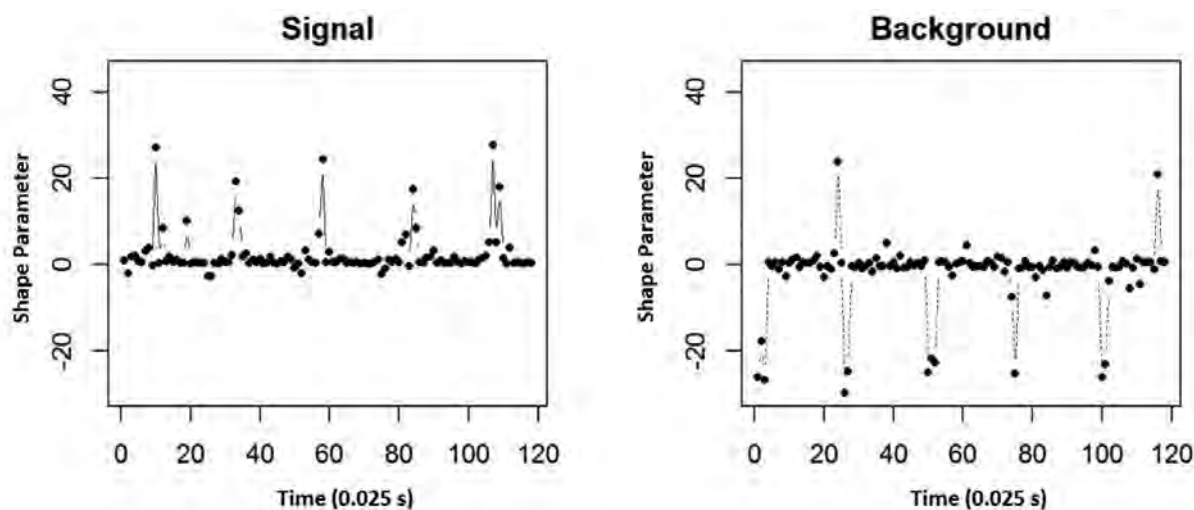
41, and 53 (shaded box plots in Figure 5). (The assumption of normality for the t test is confirmed by a visual inspection of the normal quantile-quantile plot.[26])

The comparison between the KMM and GMM can be done in the same fashion. A box plot for the difference between their LL is shown in Figure 6. Given the systematic presence of the boxes to the right of the vertical line at LL = 0, it is evident that the KMM has a generally higher LL than the GMM. (All of the P values were <.05.) It is important to emphasize that this conclusion is not unexpected. The KMM allows for more flexible distributions and, consequently, leads to higher LL values than the GMM. The more important question is whether the KMM also leads to better envelopes than the GMM, and the answer to that is no. The KMM envelopes for all 59 patients were compared with the corresponding envelopes from the GMM (both skewed and not) in terms of a visual comparison of the envelopes, a scatterplot of two envelopes (eg, Figure 5 of Marzban et al[15]), and a comparison of scalar summary measures (eg, Figure 6 of Marzban et al[15]). Although the details of the comparison are not shown here, the results suggest that the KMM envelopes are no better than those of the GMM and are often comparable with those produced by the skewed GMM. The KMM is also not as consistent (across time) as the GMM or skewed GMM, as seen by the "peak" in the right panel of Figure 2. Therefore, although there is sufficient evidence to advocate the use of the skewed GMM, that is not the case for the KMM. Further discussion of the KMM is provided in the next section.

Figure 4. Histogram of the estimated shape parameter for a single patient. The left (right) mode in this histogram corresponds to the background (signal) component of the mixture model.
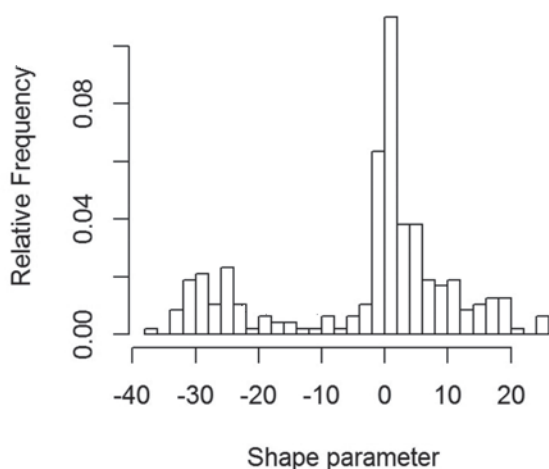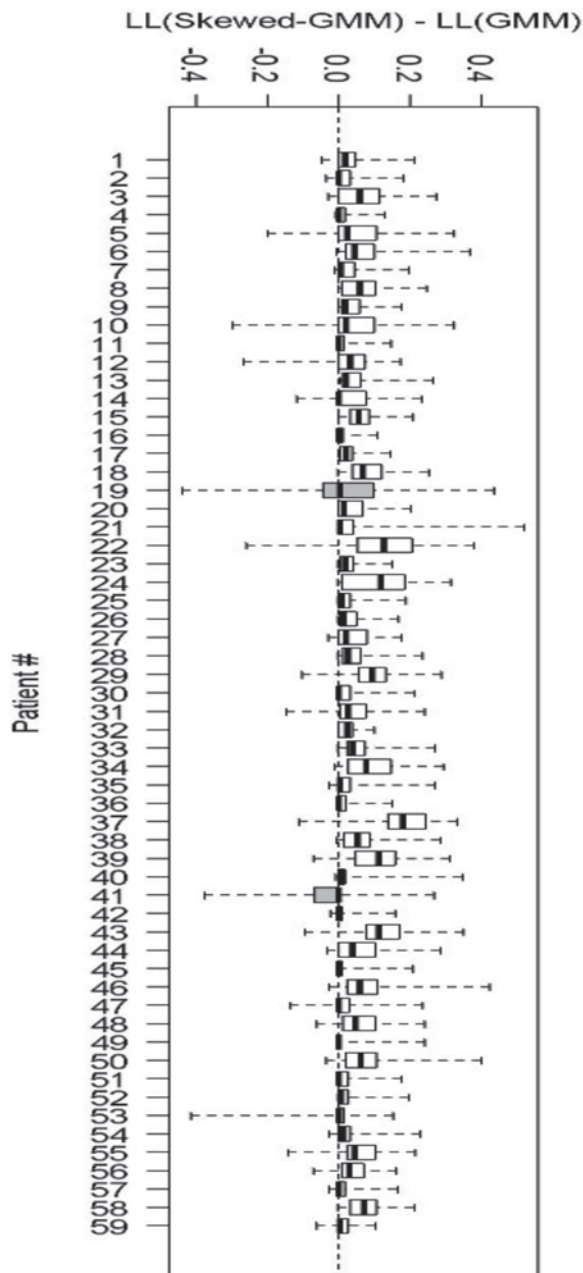

Discussion

In an earlier study, it was shown that the GMM has numerous advantages over the MGM for estimating the envelope. Here, it has been shown that a skewed GMM has the same qualitative advantages as the GMM (eg, allowing for a percentile-based notion of maximum flow velocity) but also outperforms it in terms of both the quality of the envelope (assessed through a visual comparison of the spectrogram and the envelopes) and a quantitative comparison (in terms of the goodness of fit). One may wonder whether the higher goodness-of-fit values for the skewed GMM (compared with the GMM) may be a consequence of overfitting. This concern is unwarranted because the skewed GMM has only 2 additional parameters: the shape parameters for the signal and background components. As such, the total number of independent parameters to be estimated is only 7 (mean, standard deviation, and shape parameter for each of the signal and background components, plus 1 for the mixing coefficient). There exists a large body of theoretical work on the relationship between the number of parameters and the number of observations; eg, see the Vapnik-Chernovenkis dimension in the work by Hastie et al[27] (page 210). On the practical side, one guideline that is often followed is from the classic book by Ryan[28] (page 20), who recommends at least 10 times as many observations as the number of parameters. Here, the data used for estimating the 7 parameters number in the hundreds; therefore, overfitting is not a concern.

An issue that arises in the mixture model approach to envelope estimation is the identifiability of the two components with signal and background. More specifically, a mixture model with two components will identify two components in the distribution of flow velocity values; however, an additional criterion must be introduced to decide which of the components should be identified as the signal. This factor is important because it is the percentiles of the signal component that lead to the envelope. Visually, the signal component can be identified as the one on the left, but quantifying what is meant by "on the left" is nontrivial. The approach adopted here for identifying the signal and background components of the mixture model is outlined in Appendix 2. That proposal is somewhat ad hoc, so it would be desirable to develop a more statistically sound method for identifying the signal component of mixture models.

As described above, the smoothing parameter of the KMM determines the shape of the kernel estimate of the probability density function. Here, an algorithmic criterion is used to set the values of that parameter, but the criterion optimizes the goodness of fit (ie, LL). As such,

the criterion does not automatically lead to improved envelopes. An instance of this is shown in Figure 2, where the KMM envelope displays an abrupt peak at approximately time 15 (0.025 sec), which is clearly inconsistent with the observed spectrogram. This is one of the main reasons why the KMM is not wholeheartedly advocated here.

Another reason is more computational: the procedure for estimating kernels is rather computer intensive and, therefore, slow. In fact, for this study, the KMM was developed on data for which the lowest 5% of flow velocity values

Figure 5. Box plot of LL for the skewed GMM minus LL for the GMM for all 59 patients. The shaded boxes indicate *P* > .05.

Figure 6. Same as Figure 5 but for LL for the KMM minus LL for the GMM.
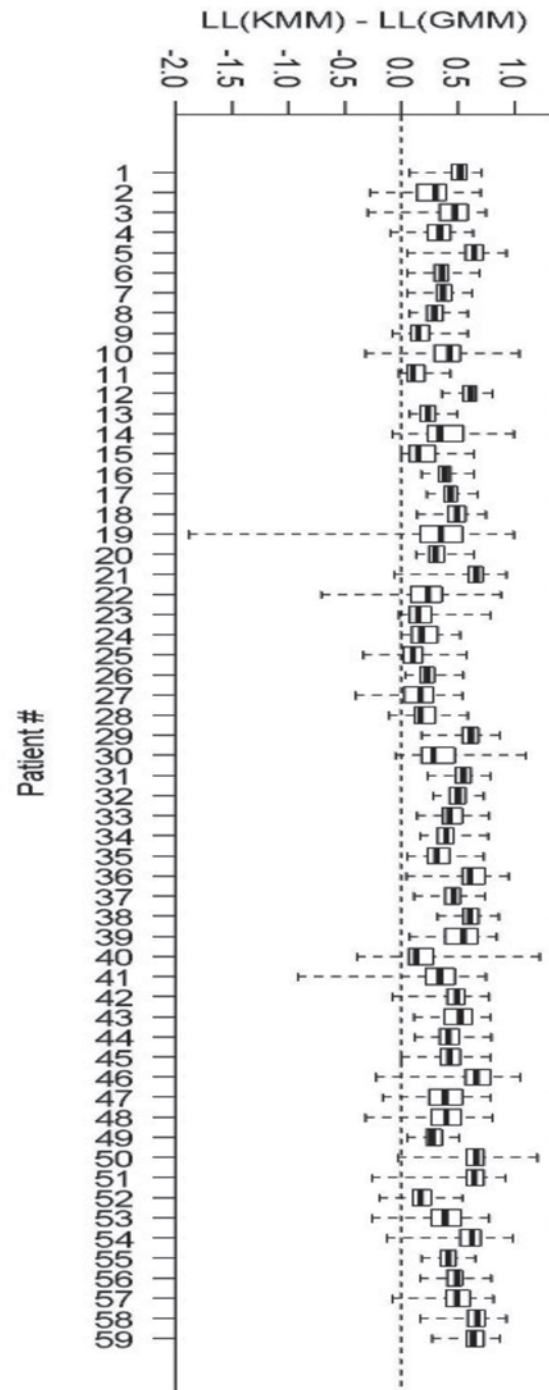
were trimmed (deleted). This process substantially increases computational speed but introduces an ad hoc parameter (ie, the 5%). In short, more work is required before one can benefit from the flexibility the of KMM as a useful envelope estimation method.

Appendix 1: Mixture Models

In a mixture model, one generally assumes that the data are generated from an underlying probability density function $[f(x)]$ that can be written as a linear combination of more well-known probability density functions. For example, for the case of two components (as considered in this study), the probability density function is written as

$$(1) \qquad f(x) = \sum \lambda_k f_k(x),$$

where λ_k are called mixing coefficients and must sum to 1. For GMMs, $f_k(x)$ is given by

$$\phi \left(\frac{x - \mu}{\sigma} \right),$$

where μ and σ^2 are mean and variance parameters, and $\phi(.)$ is the standard gaussian probability density function. Consequently such a mixture model has 5 independent parameters: the mean and variance parameters for each of the two gaussian probability density functions and one for the mixing weights, which must be estimated from data.

In a skewed GMM, the component probability density functions are assumed to be given by

$$(2) \qquad f_k(x) = 2\phi \left(\frac{x - \mu}{\sigma} \right) \Phi (\alpha x),$$

where $\Phi(x)$ is the gaussian cumulative probability distribution, and α is called the shape (or skew) parameter.[19] Large positive values of the shape parameter lead to a probability density function with a more pronounced tail for large values of x (ie, a right-skewed distribution), whereas large negative values of α have the same effect but for large negative values of x (ie, a left-skewed distribution). In this application, the skewed GMM, therefore, has 2 more parameters than the 5 parameters in the GMM. Estimated values of the shape parameter are shown in Figure 3, and the skewed probability density functions are shown in the middle panel of Figure 1. The presence of the shape parameter allows one to fit a more general class of data than can be fit with GMMs.

Even more general data can be fit with kernel methods, in which the component probability density functions in the mixture model are themselves assumed to be a sum

of the form

$$(3) \qquad f_k(x) = \frac{1}{nh} \sum K \left(\frac{x - x_i}{h} \right),$$

where x_i are the observed data; n is the sample size; and the function $K(.)$, which is called the kernel, can be any function that integrates to 1; commonly, and in the present application, $K(.)$ is taken to be the standard gaussian probability density function.[27] The additional parameter h, called the bandwidth, effectively determines the smoothness of the probability density function; a small value of h will lead to a highly "spiky," nonsmooth probability density function, whereas larger values of h will lead to smoother, more gaussian-looking, probability density functions. For this study, its value was determined as follows: The default choice of the bandwidth h minimizes a quantity called asymptotic mean integrated squared error[29] and is given by

$$(4) \qquad h = 0.9 n^{-1/5} \min \left\{ SD, \frac{IQR}{1.34} \right\},$$

where SD and IQR are the standard deviation and interquartile range of all n observations, respectively. It has been shown that this estimate is somewhat smaller than the true optimal value,[24] so the value chosen here is taken to be larger than the default value, which in turn leads to smoother fits. As a result, at each time, and for each patient, $h = 10$ is used, unless equation 4 gives a larger value, in which case the larger value is selected. The fits are visually inspected to ensure that the chosen value of the bandwidth does not lead to overfitting.

Appendix 2: Identifying the Signal Distribution

As described above, the mixture model identifies two components in the distribution of flow velocity values. However, the task of identifying which of the components is the signal (and which is the background), is nontrivial. Here, the following 3 criteria are used to derive an algorithm for the identification task: The signal component is more likely the one with (1) a lower mean, (2) a higher peak, and (3) a larger standard deviation. The means, peaks, and standard deviations of the two components are denoted as (μ_1, μ_2), (p_1, p_2), and (s_1, s_2), respectively. The ratios are defined as $a = \mu_1/\mu_2$; $b = p_1/p_2$; and $c = s_1/s_2$. As such, the signal component is more likely to be the component labeled 1 when a is small and b and c are large. Therefore, if $x = (1/a) \times b \times c$ is larger than 1, then the component labeled 1 should be identified as the signal. Similarly, $x < 1$ indicates that the component labeled 1 should be identified as the background.

References

1. Aaslid R, Nornes H. Musical murmurs in human cerebral arteries after subarachnoid hemorrhage. *J Neurosurg* 1984; 60:32–36.

2. Aaslid R, Huber P, Nornes H. Evaluation of cerebrovascular spasm with transcranial Doppler ultrasound. *J Neurosurg* 1984; 60:37–41.

3. Aaslid R, Huber P, Nornes H. A transcranial Doppler method in the evaluation of cerebrovascular spasm. *Neuroradiology* 1986; 28:11–16.

4. Aaslid R. Transcranial Doppler assessment of cerebral vasospasm. *Eur J Ultrasound* 2002; 16:3–10.

5. Armonda RA, Bell RS, Vo AH, et al. Wartime traumatic cerebral vasospasm: recent review of combat casualties. *Neurosurgery* 2006; 59:1215–1225.

6. Babikian VL, Wechsler LR, Toole JF (eds). *Transcranial Doppler Ultrasonography*. Boston, MA: Butterworth-Heinemann; 1999.

7. Sloan MA, Wozniak MA, Macko RF. Monitoring of vasospasm after subarachnoid hemorrhage. In: Babikian VL, Wechsler LR, Toole JF (eds). Transcranial Doppler Ultrasonography. Boston, MA: Butterworth-Heinemann; 1999:109–128.

8. Tegeler CH, Rotanakorn D. Physics and principles. In: Babikian VL, Wechsler LR, Toole JF (eds). *Transcranial Doppler Ultrasonography*. Boston, MA: Butterworth-Heinemann; 1999:3–11.

9. Tsivgoulis G, Alexandrov AV, Sloan MA. Advances in transcranial Doppler ultrasonography. *Curr Neurol Neurosci Rep* 2009; 9:46–54.

10. Fernando KL, Mathews VJ, Clark EB. A mathematical basis for the application of the modified geometric method for maximum frequency estimation. *IEEE Trans Biomed Eng* 2004; 51:2085–2088.

11. Güler I, Hardalac F, Kaymaz M. Comparison of FFT and adaptive ARMA methods in transcranial Doppler signals recorded from the cerebral vessels. *Comput Biol Med* 2002; 32:445–453.

12. Moraes R, Adin N, Evans DH. The performance of three maximum frequency envelope detection algorithms for Doppler signals. *J Vasc Invest* 1995; 1:126–134.

13. Östlund N, Yu J, Karlsson JS. Improved maximum frequency estimation with application to instantaneous mean frequency estimation of surface electromyography. *IEEE Trans Biomed Eng* 2004; 51:1541–1546.

14. Rubin JM, Bude RO, Fowlkes JB, Spratt RS, Carson PL, Adler R. Normalizing fractional moving blood volume estimates with power Doppler US: defining a stable intravascular point with the cumulative power distribution function. *Radiology* 1997; 205:757–765.

15. Marzban C, Illian PR, Morison D, Mourad PD. A double-gaussian, percentile-based method for estimating maximum blood flow velocity. *J Ultrasound Med* 2013; 32:1913–1920.

16. Pereira M, Freire M. *Biomedical Diagnostics and Clinical Technologies: Applying High-Performance Cluster and Grid Computing*. Hershey, PA: IGI Global; 2010:263.

17. McLachlan GJ, Peel D. *Finite Mixture Models*. Hoboken, NJ: John Wiley & Sons; 2000.

18. Basso R, Lachos V, Cabral C, Ghosh P. Robust mixture modeling based on scale mixtures of skew-normal distributions. *Comput Stat Data Analysis* 2010; 54:2926–2941.

19. Prates M, Cabral CH, Lachos V. mixsmsn: fitting finite mixture of scale mixture of skew-normal distributions. *J Stat Software* 2013; 54:1–20.

20. Dinov ID. Expectation maximization and mixture modeling tutorial. California Digital Library, Statistics Online Computational Resource website. http://repositories.cdlib.org/socr/EM_MM. December 9, 2008.

21. Dempster AP, Laird NM, Rubin DB. Maximum likelihood from incomplete data via the EM algorithm. *J R Stat Soc Ser B* 1977; 39:1–38.

22. Benaglia T, Chauveau D, Hunter DR, Young D. mixtools: an R package for analyzing finite mixture models. *J Stat Software* 2009; 32:1–29.

23. Benaglia T, Chauveau D, Hunter DR. An EM-like algorithm for semi- and non-parametric estimation in multivariate mixtures. *J Comput Graph Stat* 2009; 18:505–526.

24. Benaglia T, Chauveau D, Hunter DR. Bandwidth selection in an EM-like algorithm for nonparametric multivariate mixtures. In: *Nonparametric Statistics and Mixture Models: A Festschrift in Honor of Thomas P. Hettmansperger*. Singapore: World Scientific Publishing Co; 2011:15–27.

25. Marzban C, Illian PR, Morison D, et al. A method for estimating zero-flow pressure and intracranial pressure. *J Neurosurg Anesthesiol* 2013; 25:25–32.

26. R Development Core Team. R: a language and environment for statistical computing. R Project website; 2011. http://www.R-project.org.

27. Hastie T, Tibshirani R, Friedman J. *The Elements of Statistical Learning*. New York, NY: Springer; 2001.

28. Ryan T. *Modern Regression Methods*. Hoboken, NJ: John Wiley & Sons; 2009.

29. Silverman BW. *Density Estimation*. London, England: Chapman & Hall; 1986.

A Double-Gaussian, Percentile-Based Method for Estimating Maximum Blood Flow Velocity

Caren Marzban, PhD, Paul R. Illian, BS, David Morison, BS, Pierre D. Mourad, PhD

Objectives—Transcranial Doppler sonography allows for the estimation of blood flow velocity, whose maximum value, especially at systole, is often of clinical interest. Given that observed values of flow velocity are subject to noise, a useful notion of "maximum" requires a criterion for separating the signal from the noise. All commonly used criteria produce a point estimate (ie, a single value) of maximum flow velocity at any time and therefore convey no information on the distribution or uncertainty of flow velocity. This limitation has clinical consequences especially for patients in vasospasm, whose largest flow velocities can be difficult to measure. Therefore, a method for estimating flow velocity and its uncertainty is desirable.

Methods—A gaussian mixture model is used to separate the noise from the signal distribution. The time series of a given percentile of the latter, then, provides a flow velocity envelope. This means of estimating the flow velocity envelope naturally allows for displaying several percentiles (eg, 95th and 99th), thereby conveying uncertainty in the highest flow velocity.

Results—Such envelopes were computed for 59 patients and were shown to provide reasonable and useful estimates of the largest flow velocities compared to a standard algorithm. Moreover, we found that the commonly used envelope was generally consistent with the 90th percentile of the signal distribution derived via the gaussian mixture model.

Conclusions—Separating the observed distribution of flow velocity into a noise component and a signal component, using a double-gaussian mixture model, allows for the percentiles of the latter to provide meaningful measures of the largest flow velocities and their uncertainty.

Key Words—blood flow; brain; head injury; noninvasive; transcranial Doppler sonography
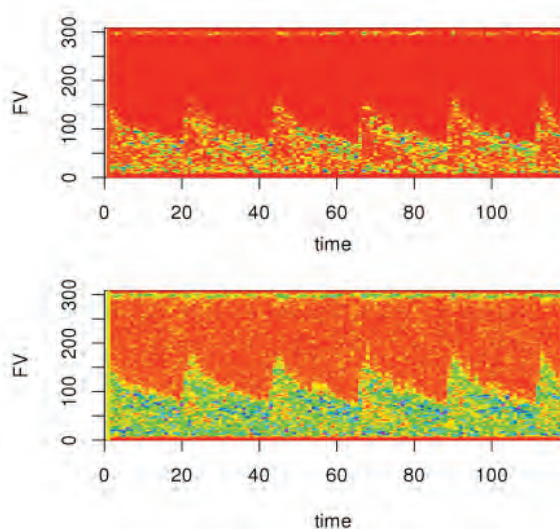
Address correspondence to Caren Marzban, PhD, Department of Statistics, University of Washington, Box 354322, Seattle, WA 98195-4322 USA.

E-mail: marzban@stat.washington.edu

Transcranially derived Doppler measurements of blood flow in major cerebral arteries have found many clinical applications.[1] In addition to assaying stroke risk due to sickle cell disease, dysfunction of cerebral autoregulation, and a patent foramen ovale, among other etiologies, some of the earliest applications targeted monitoring for vasospasm after subarachnoid hemorrhage.[2–5] Cerebral vasospasm, the transient reduction of the diameter of 1 or more major cerebral arteries, can lead to reduced blood flow into the brain and hence cerebral ischemia and an increasing chance for neurologic damage.[1] Monitoring for the onset of vasospasm remains an important application of transcranial Doppler sonography, with more 30,000 patients per year requiring daily monitoring for 1 week or more.[6] Adding to this primarily

civilian population are military patients with head injuries after exposure to explosions, typically roadside bombs, with half of these patients having cerebral vasospasm.[7]

Transcranial Doppler sonography measures the distribution of blood flow speeds within a blood vessel toward or away from the transducer, with negligible flow speeds adjacent to the blood vessel wall and maximum flow speeds near the center of the vessel.[8] Critical for the assay of cerebral vasospasm, among other uses of transcranial Doppler sonography, is successful capture of the speed of the fastest flowing blood within the major cerebral arteries, since this value acts as a useful proxy for blood vessel narrowing.[1] Capturing this speed is a particularly challenging problem, since vasospasm reduces the volume of blood flow while accelerating the blood flow speed,[9] hence reducing the target for transcranial Doppler measurements while straining against the upper limits of ultrasound data processing due to aliasing.[10]

The time series of a flow velocity histogram is generally referred to as a spectrogram, and the time series of the maximum flow velocity is called an envelope. Although the spectrogram conveys a great deal of information, the envelope is often the only quantity a clinician examines. This practice is reasonable because the information contained in a spectrogram can be displayed in different ways, leading to different conclusions. For example, Figure 1 shows a spectrogram with 2 different color schemes; in the top panel, the spectrogram is linearly related to the color scale, whereas in the bottom panel, the colors are proportional to the square root of the spectrogram.

This inherent ambiguity in the information gleaned from a spectrogram also reflects itself in the corresponding envelope. In practice, observed flow velocity values can range from 1 to 300 cm/s. Therefore, to obtain a useful estimate of maximum flow velocity, one must introduce some criterion that defines what is meant by maximum. Many such criteria (standards for transcranial Doppler measurements[11–15]) are based on the cumulative histogram of flow velocity. Figure 2 shows an example of the relative frequency histogram of flow velocity (top) and the corresponding cumulative histogram (bottom) at a specific time for a specific patient (hereafter, patient X); the latter is obtained by integrating the former from left to right. One may define the maximum flow velocity as the value at which the cumulative histogram "levels off," but there exist different criteria corresponding to different objective measures of that point.[11–15] The vertical bar in Figure 2 marks the flow velocity at which it is maximum according to the modified geometric method.[11,12] The top panel in Figure 3 shows the spectrogram and the modified geometric method envelope (in black) for patient X.

Given that the proposed algorithm is compared with the modified geometric method algorithm, a brief review of the latter is in order. The modified geometric method algorithm and its variants[11,12] effectively rotate (clockwise and about the origin) the cumulative histogram by some amount. The effect of such a rotation is that the point at which the cumulative histogram levels off translates to a point at which the rotated cumulative histogram reaches

Figure 1. Spectrograms of 2 different mappings for assigning color to the flow velocity (FV) values: linear (top) and square root (bottom).


Figure 2. Histograms of flow velocity (FV) for patient X at a given instant in time (top), and the corresponding cumulative (ie, integrated) histogram (bottom).
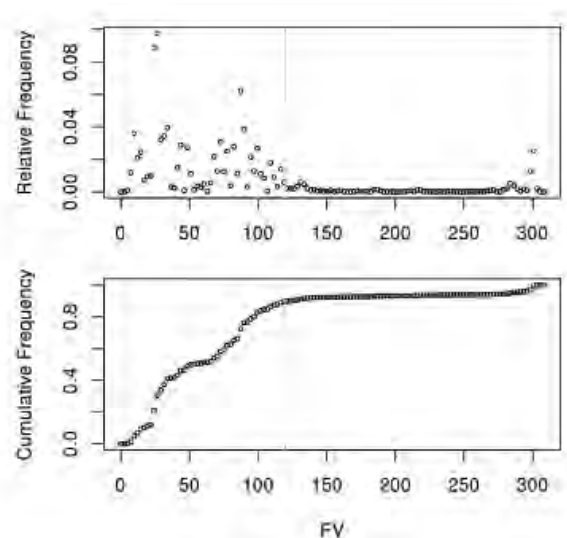
the maximum. Given certain smoothness constraints, it has been shown that this point corresponds to the maximum flow velocity.[12] Note that the modified geometric method algorithm generates only point estimates of the maximum flow velocity and so provides no natural measure of uncertainty. This limitation is evident in the cumulative histogram in Figure 2: Although the modified geometric method provides an estimate of the point at which the cumulative histogram levels off, quantifying the corresponding uncertainty is by no means unambiguous. Conveying uncertainty is important because different levels of uncertainty call for different clinical actions.

The main proposals in this study were (1) to develop a new means of separating the noise and the signal components of a spectrogram and (2) to quantify the largest values in the signal using the concept of percentile. The nth percentile of a quantity x is defined as the value of x for which $n\%$ of the x values are smaller. For example, the 95th percentile of flow velocity is the flow velocity value at which 95% of flow velocity values are smaller. An envelope based on the 95th percentile of the histogram, then, provides a meaningful estimate of the "top 5%" of flow velocities. Moreover, 2 (or more) envelopes at different percentiles can convey some notion of uncertainty. In this study, envelopes based on 3 percentiles were considered: 90th, 95th, and 99th.

Figure 3. Top, Spectrogram for patient X (color background) and 4 estimates of the envelope: modified geometric method envelope (black) and 90th, 95th, and 99th percentile-based envelopes. Bottom, Modified geometric method envelope (black), 95th percentile-based envelope (red), and 90th and 99th percentile-based envelopes (blue). FV indicates flow velocity.
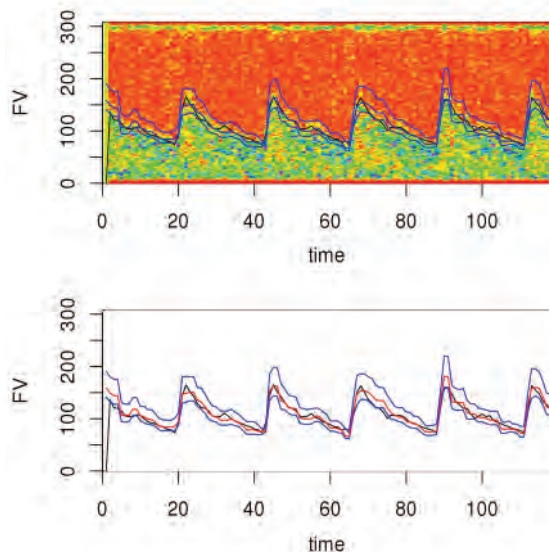
The use of a percentile to quantify the largest flow velocity presumes that the histogram is the correct histogram of flow velocity. In practice, observed spectrograms are contaminated by various types of noise. One of these sources of noise is evident in the small "hump" appearing on the right side of the (relative frequency) histogram in Figure 2. Flow velocity values and their associated percentiles are useful only if they pertain to the non-noise component of the histogram, hereafter called the *signal distribution*. In fact, the 90th percentile of the histogram shown in Figure 2 is near the right-most hump and therefore unrealistic. Therefore, to compute useful percentile-based envelopes, one must first disambiguate the signal and noise contributions to the histogram. To that end, here, a gaussian mixture model with 2 components[16,17] was used to represent the noise and signal components, respectively. The component appearing to the left (closest to the origin) was defined as the signal distribution. Armed with the signal distribution, the 3 percentiles were computed at each time, and their time series was computed for 59 patients. The 3 percentile-based envelopes for patient X are shown in Figure 3, both with the spectrogram (top panel), and without (bottom panel).

In this article, the details of this percentile-based approach for estimating an envelope are presented. It was found that the estimates are visually consistent with the underlying spectrograms, and the modified geometric method envelope is approximately consistent with the 95th percentile envelope. Also, it is shown that percentile-based envelopes naturally allow for displaying envelope uncertainty.

Materials and Methods

Data
Patient data for this preclinical study were collected from a variety of hospitals in the United States, following a study at the University of Washington led by Dr Mourad. The data included arterial blood pressure and intracranial pressure, but those data were not used for this study; only sonographically derived transcranial Doppler spectra were used. Further details on the patient data may be found in an article by Marzban et al.[18] In accordance with the Institutional Review Board for each hospital, informed consent was obtained from all patients or their families.

Doppler spectral time series of blood flow speed in the middle cerebral artery (or flow velocity – flow velocity) were acquired at each institution via clinically approved transcranial Doppler units. Data acquisition lengths varied from 5 to 30 minutes. All retrospective data processing and

analysis were conducted at the Applied Physics Laboratory of the University of Washington. Doppler spectral time series data collected via the Applied Physics Laboratory's hospital cohort were initially digitized at 125 Hz in time and with a frequency resolution of 128 Hz at a given time. We then down-sampled these Doppler time series to a resolution of 40 Hz in time, sufficient to resolve all of the following features in all of our patients' data: systolic rise, diachrotic notch, and diastolic minimum. We also selected a fixed duration (118 time steps, or ≈3 minutes) from each of the 59 patients for statistical analysis. This duration was sufficiently long to include several cardiac cycles while still allowing details of the envelopes to be visually evident.

Data Processing and Statistical Analysis

As mentioned in the introduction, the main aims of the proposed method were to first represent the instantaneous Doppler frequency distribution of the flow velocity at a given moment in time and then to produce spectral envelopes of those frequency distributions through time based on percentiles of that distribution in the Doppler frequency. Distinguishing the signal from the noise requires a model. In this article, it is assumed that the underlying distribution of flow velocity consists of 2 distributions, corresponding to the signal and noise, and that both are gaussian. This type of model is a special case of gaussian mixture models, wherein a distribution is assumed to be a linear combination of gaussian distributions.[16,17] The weights in the linear combination (called mixing proportions) and the parameters of the gaussian distributions are then estimated from data via some optimization procedure. (In this study, the expectation-maximization algorithm was used, but other parameter estimation methods are equally adequate. The expectation-maximization algorithm maximizes the conditional expected log likelihood.[19]) Figure 4 shows the signal component (black) and the noise component (red) for the example shown in Figure 2. Also shown are the locations of the maximum flow velocity according to modified geometric method (black vertical line) and the 90th, 95th, and 99th percentiles of the signal distribution (blue vertical lines). All statistical analyses were performed in R.[20]

Results

The previous section illustrates the proposed method on a given patient and at a given time. The top panel in Figure 3 shows the 3 percentile-based envelopes (blue curves) for patient X. It is evident that the percentile-based envelopes are consistent with the underlying spectrogram. The bot-

tom panel in Figure 3 shows 4 envelopes; the modified geometric method envelope (black) is comparable with the 95th percentile envelope (red), sandwiched between the 90th and 99th percentile envelopes (blue). Clearly, displaying multiple percentile-based envelopes conveys a sense of the uncertainty in the maximum flow velocities.

Although technical, it is also worth mentioning 2 additional steps taken to generate the percentile-based envelopes shown in Figure 3: (1) The optimization algorithm used for the gaussian mixture model requires initial estimates of the parameters of interest. At time 0, the initial values of the parameters are assigned randomly, and the optimization algorithm produces parameter values that characterize the 2 best-fit gaussian components of the flow velocity histogram at that time. At all "future" times, the initial values of the parameters are set to the final values obtained at the previous time step. This process allows some of the serial (auto) correlation in the spectrogram to be reflected in the envelopes. If the values of the gaussian mixture model parameters are initialized randomly for every and all time steps, the resulting envelopes are somewhat less smooth than those shown in Figure 3. (2) A running-median filter with a window size of 3 seconds is applied to the envelopes to smooth them even further. The size of the window (ie, 3) is obtained by trial and error and by a visual comparison with the modified geometric method envelope. The modified geometric method envelope too is smoothed by a variety of techniques, eg, an averaging (over multiple cardiac cycles) filter and a finite impulse response

Figure 4. Histogram of flow velocity (FV) for patient X (circles) and the estimated densities for the 2 gaussian components. The black vertical bar denotes the maximum flow velocity according to the modified geometric method, and the blue vertical bars correspond to the 90th, 95th, and 99th percentiles of the signal distribution on the left.
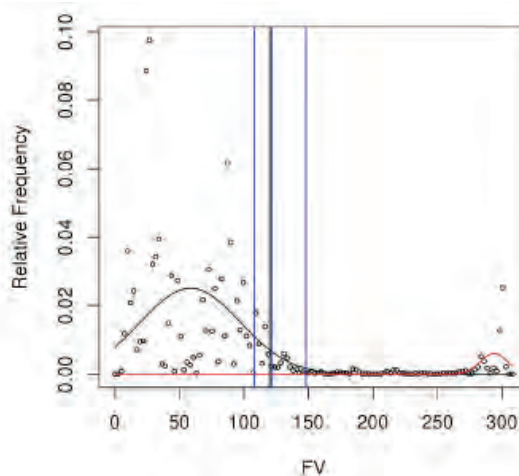
filter. Although the smoothness of the displayed envelopes is important in a clinician's decision making, it is a feature that is easily controlled (eg, by a single parameter, such as the window size of the running-median filter) and so is not of serious concern.

The procedure was applied to all 59 patients in the data set. It is impractical to show all 59 figures analogous to Figure 3. Instead, the 3 percentile-based envelopes were compared with the modified geometric method envelope using scatterplots, which were then further summarized into scalar measures.

Each panel in Figure 5 shows the scatterplot of one of the percentile-based envelopes versus the modified geometric method envelope for patient X. There are 118 points on each scatterplot, corresponding to the 118 time steps displayed in Figure 3. The diagonal line is simply a line of slope 1, y-intercept 0. It is clear from the middle panel that the 95th percentile envelope generally agrees with the modified geometric method envelope. As expected, the 90th and 99th percentile envelopes are generally lower and higher, respectively, than the modified geometric method envelope. The disagreements between the percentile-based envelopes and the modified geometric method envelope are largest for higher flow velocity values. This result is especially evident in the 99th percentile envelope (bottom panel) in the manner in which the deviation of the scatterplot from the diagonal line is largest for higher flow velocity values. In other words, the systolic peaks of the 99th percentile envelope are in fact higher than might be expected from the modified geometric method envelope.

One may further summarize each of these panels by computing the root mean squared error between the modified geometric method envelope and each percentile-based envelope. For patient X, the root mean squared error values corresponding to the 3 panels in Figure 5 are 17.9, 16.9, and 31.2 cm/s. In addition to confirming that the modified geometric method envelope is closest to the 95th percentile envelope (for patient X), these numbers have useful interpretations as well; eg, it can be said that the modified geometric method envelope and the 95th percentile envelope have a typical deviation of about 16.9 cm/s across the 118 time steps examined.

Although useful for comparing different envelopes, root mean squared error values do not assess whether the difference in the envelopes is due to the amount of scatter in the scatterplot or to an overall shift. There exists a decomposition of root mean squared error that allows one to examine both contributions. The details of the decomposition are presented in "Appendix." Here, suffice it to say that the correlation coefficient (denoted

Corr) and bias (ie, mean [modified geometric method] – mean [percentile-based method]) gauge the amount of scatter and the overall shift, respectively. The Corr values for the 3 panels in Figure 5 are 0.80, 0.81, and 0.81 (from top to bottom), suggesting that the amount of scatter in the 3 panels is comparable. Said differently, any of the 3 percentile-based envelopes provides an adequate approximation to the modified geometric method envelope, if/when correlation is the measure of agreement. The main difference between the 3 panels is in the Bias values: 8.5, –2.6, and –23.5 (from top to bottom). These numbers have useful interpretations, too; eg, one can say that the 95th percentile envelope is generally shifted above the modified geometric method envelope by about 2.6 cm/s for patient X.

To compare the various envelopes across all of the patients, root mean squared error, Corr, and Bias were computed for all 59 patients. Their distributions are shown in Figure 6. The left-most box plot in the top panel summarizes the histogram (across 59 patients) of the root mean squared error computed for the 90th percentile envelope and the modified geometric method envelope (across 118 time steps).

The middle panel in Figure 6 is analogous to the top panel except that the measure of agreement between the modified geometric method envelope and the percentile-based envelope is Corr. The 3 box plots are comparable, implying that all 3 percentile-based envelopes are comparably correlated with the modified geometric method envelope across all 59 patients. The bottom panel shows that, on average (across all 59 patients), the 90th and 99th

Figure 5. Scatterplots of the 3 percentile-based envelopes and the modified geometric method envelope for patient X. FV indicates flow velocity.
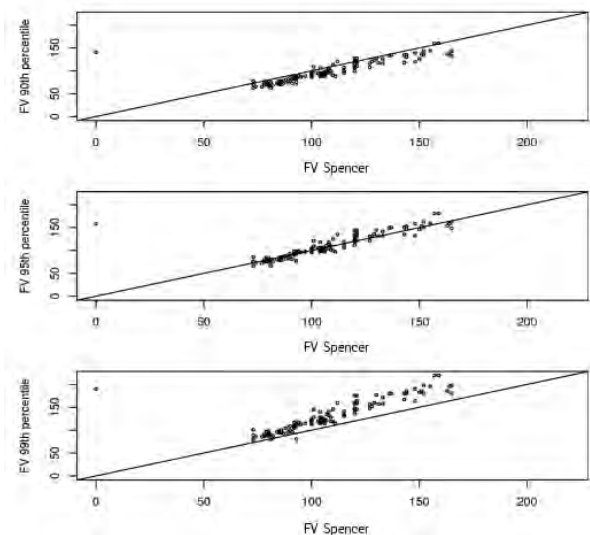
percentile envelopes are below and above the modified geometric method envelope, respectively. By comparing the 3 box plots in the top or bottom panel, it can be seen that the agreement between the modified geometric method envelope and the 95th percentile envelope, noted for patient X, extends to all 59 patients.

It is worth displaying the envelope for a patient for whom such scalar measures are generally poor. Figure 7 shows the spectrogram and envelopes for the patient with the lowest Corr value. It is clear that the modified geometric method envelope (black) is in fact incorrect and that the percentile-based envelopes (blue) are more consistent with the underlying spectrogram. In other words, the low Corr value for this patient does not imply a defect on the part of the percentile-based envelope but rather a defect in the modified geometric method envelope.

Discussion

It has been shown that a double-gaussian mixture model can be used to identify a component of the histogram of flow velocity corresponding to a "signal." In turn, percentiles of this signal distribution provide envelopes, which meaningfully quantify the largest flow velocity. Not only are these percentile-based envelopes visually consistent with their underlying spectrograms, they are also objectively consistent with a commonly used envelope based on the modified geometric method. The percentile-based envelopes not only objectively quantify

what is meant by "largest flow velocities" but also have the added advantage (over existing envelopes) of allowing for a natural display of uncertainty in the envelopes.

Given that the analysis is performed on real (not simulated) data, the true envelope is not known. As such, the quality of each envelope cannot be assessed objectively on its own merit. For that reason, the analysis here has been based on visually comparing an envelope with the underlying spectrogram (eg, as in Figure 3), or objectively comparing each of the percentile-based envelopes with the modified geometric method envelope (eg, Figures 5 and 6). In spite of the central role played by the modified geometric method envelope in comparing envelopes, it is important to recall that the modified geometric method envelope is not the true envelope (eg, see Figure 7). Here, it is used as a standard only because of its common usage.

Of the 3 percentile-based envelopes, the 95th percentile envelope is closest to the modified geometric method envelope, but the agreement is not perfect, as seen by the box plots in Figure 6. For example, according to the middle box plot in the bottom panel, on average (across patients), the 95th percentile envelope is slightly above the modified geometric method envelope. One may ask what is the exact percentile corresponding to the modified geometric method envelope, but the question itself is inappropriate because it elevates the status of the modified geometric method envelope to a "reference standard," when in fact it is not. What is more important is that the proposed approach produces a useful spectrogram as well

Figure 6. Distribution of the root mean squared error (RMSE), correlation coefficient (Corr), and Bias (defined in "Appendix") for all 59 patients examined in this work.
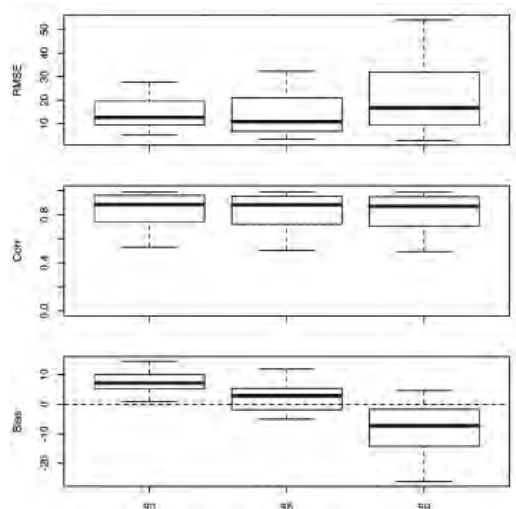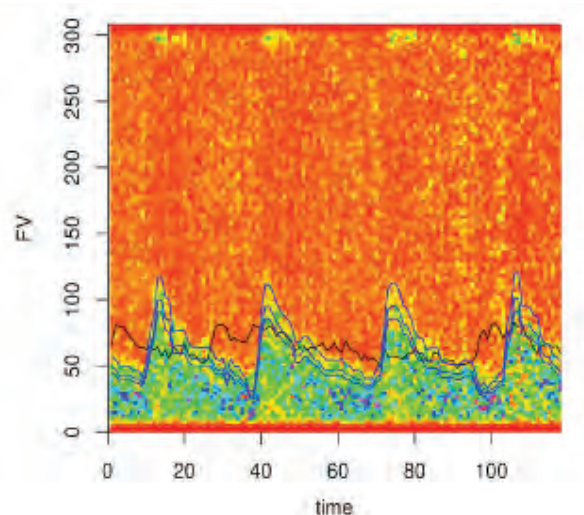

Figure 7. Same as Figure 3, but for a patient for whom the modified geometric method envelope (black) is clearly incorrect. FV indicates flow velocity.

as an interpretable (in terms of percentiles) generalization of approaches that naturally produce only a single envelope (eg, modified geometric method).

A percentile-based envelope is based on a percentile of the signal distribution, in which the signal (and noise) distribution is defined from fitting a gaussian mixture model with 2 components to the whole histogram, at a given time. There is some justification for examining the 3 components. For example, in Figure 4, one may argue that there are possibly 3 overlaying histograms: 1 corresponding to the large hump on the left (ie, the signal), 1 associated with the small hump on the right (ie, associated with an aliasing reflection on Doppler imaging, and another corresponding to a uniform "background" spanning the full range of flow velocity values. We repeated the entire analysis but with 3 gaussian components. The results are inconclusive and require further research. For some patients, the results do not change substantially, but for others, they do in ways that can be considered "better" or "worse" depending on the measure of quality.

The percentiles of the signal distribution allow for meaningful envelopes, which can objectively assess the largest flow velocity. In addition, displaying multiple envelopes can convey information on the uncertainty in the observed flow velocity. One can envisage an alternative measure of uncertainty. For example, one may consider the envelope corresponding to a fixed percentile, say 95th, and then obtain the distribution of that quantity via some resampling method.[21] In turn, that (sampling) distribution can be used to compute confidence intervals for the true 95th percentile envelope. Such interval estimates of the envelope can be useful in conveying uncertainty if/when a specific percentile is of interest. Otherwise, displaying multiple envelopes corresponding to different percentiles, as done here, is sufficient for conveying uncertainty.

Appendix

Let x_i and y_i denote the values of the modified geometric method envelope and a percentile-based envelope, respectively, at time i. The root mean square error between 2 envelopes is defined as the square root of the mean square error (MSE):

$$(1) \qquad MSE = \frac{1}{n-1} \sum (y_i - x_i)^2,$$

where n is the length of the time steps (here, 118). It can be shown that

$$(2) \qquad MSE = s_x^2 + s_y^2 - 2(\text{Corr})s_x s_y + \frac{n}{n-1}(\text{Bias})^2,$$

where s_x and s_y are the sample standard deviations of x and y, respectively, Corr denotes the Pearson correlation coefficient, and

$$(3) \qquad \text{Bias} = \text{mean } x - \text{mean } y.$$

According to Equation 2, a comparison of 2 envelopes in terms of mean square error (or root mean square error) is equivalent to a comparison in terms of Corr and in terms of Bias; the former compares the correlation between the envelopes, and the latter measures the overall shift between them.

References

1. Sloan MA, Wozniak MA, Macko RF. Monitoring of vasospasm after subarachnoid hemorrhage. In: Babikian VL, Wechsler LR, Toole JF (eds). *Transcranial Doppler Ultrasonography*. Boston, MA: Butterworth-Heinemann; 1999:109–128.

2. Aaslid R, Nornes H. Musical murmurs in human cerebral arteries after subarachnoid hemorrhage. *J Neurosurg* 1984; 60:32–36.

3. Aaslid R, Huber P, Nornes H. Evaluation of cerebrovascular spasm with transcranial Doppler ultrasound. *J Neurosurg* 1984; 60:37–41.

4. Aaslid R, Huber P, Nornes H. A transcranial Doppler method in the evaluation of cerebrovascular spasm. *Neuroradiology* 1986; 28:11–16.

5. Aaslid R. Transcranial Doppler assessment of cerebral vasospasm. *Eur J Ultrasound* 2002; 16:3–10.

6. Oertel M, Boscardin WJ, Obrist WD, et al. Posttraumatic vasospasm: the epidemiology, severity, and time course of an underestimated phenomenon—a prospective study performed in 299 patients. *J Neurosurg* 2005; 103:812–824.

7. Armonda RA, Bell RS, Vo AH, et al. Wartime traumatic cerebral vasospasm: recent review of combat casualties. *Neurosurgery* 2006; 59:1215–1225.

8. Babikian VL, Wechsler LR, Toole JF (eds). *Transcranial Doppler Ultrasonography*. Boston, MA: Butterworth-Heinemann; 1999.

9. Tsivgoulis G, Alexandrov AV, Sloan MA. Advances in transcranial Doppler Ultrasonogrphy. *Curr Neurol Neurosci Rep* 2009; 9(1):46-54.

10. Tegeler CH, Rotanakorn D. Physics and principles. In: Babikian VL, Wechsler LR, Toole JF (eds). *Transcranial Doppler Ultrasonography*. Boston, MA: Butterworth-Heinemann; 1999:3–11.

11. Moraes R, Adin N, Evans DH. The performance of three maximum frequency envelope detection algorithms for Doppler signals. *J Vasc Invest* 1995; 1:126–134.

12. Fernando KL, Mathews VJ, Clark EB. A mathematical basis for the application of the modified geometric method for maximum frequency estimation. *IEEE Trans Biomed Eng* 2004; 51:2085–2088.

13. Güler I, Hardalaç F, Kaymaz M. Comparison of FFT and adaptive ARMA methods in transcranial Doppler signals recorded from the cerebral vessels. *Comput Biol Med* 2002; 32:445–453.

14. Östlund N, Yu J, Karlsson JS. Improved maximum frequency estimation with application to instantaneous mean frequency estimation of surface electromyography. *IEEE Trans Biomed Eng* 2004; 51:1541–1546

15. Rubin JM, Bude RO, Fowlkes JB, Spratt RS, Carson PL, Adler RS. Normalizing fractional moving blood volume estimates with power Doppler US: defining a stable intravascular point with the cumulative power distribution function. *Radiology* 1997; 205:757–765.

16. McLachlan GJ, Peel D. *Finite Mixture Models*. Hoboken, NJ: John Wiley & Sons; 2000.

17. Bishop C. *Pattern Recognition and Machine Learning*. New York, NY: Springer; 2006.

18. Marzban C, Illian PR, Morison D, et al. A method for estimating zero-flow pressure and intracranial pressure. *J Neurosurg Anesthesiol* 2013; 25:25–32.

19. Dinov ID. Expectation maximization and mixture modeling tutorial. California Digital Library, Statistics Online Computational Resource website; December 9, 2008. http://repositories.cdlib.org/socr/EM_MM.

20. R Development Core Team. R: a language and environment for statistical computing. R Project website; 2011. http://www.R-project.org.

21. Efron B, Tibshirani RJ. *An Introduction to the Bootstrap*. London, England: Chapman & Hall; 1998.